Reverse engineering of an automotive wind tunnel composite fan blade

by Gavin Lee Quentin Spring-Benyon

FILE	9981_GAVIN_LEE_QUENTIN_SPRING-BENYON_REVERSE_ENGINEERING_OF_AN_AUTOMOTIVE_WIND_TUNNEL_COMPOSITE_FAN_BLADE_128469_271563434.PDF (14.14M)		
TIME SUBMITTED	29-APR-2019 08:31PM (UTC+0100)	WORD COUNT	34302
SUBMISSION ID	105745364	CHARACTER COUNT	200473

Prifysgol Cymru
Y Drindod Dewi Sant
University of Wales
Trinity Saint David

University Of Wales Trinity Saint David
School of **Engineering**
BEng Motorsport Engineering

Reverse Engineering Of An Automotive Wind Tunnel Composite Fan Blade



Gavin Lee Quentin Spring-Benyon

April 2019

P142997

LENTUS COMPOSITES

AMG PETRONAS FORMULA ONE TEAM

Declaration Of Authenticity

'This thesis is the result of the author's original research. It has been composed by the author and has not been previously submitted for examination which has led to the award of a degree.'

Name: Gavin Spring-Benyon

Signed: Date:29/04/2019

Abstract

This document reports on the research, methodology, testing, FEA results and design development of a reverse engineered composite wind tunnel fan blade. The blade in question is from *Mercedes AMG Petronas' F1 Team's* wind tunnel 2. The project was undertaken in partnership with *Lentus Composites* and *Mercedes AMG Petronas' F1 Team*. *Mercedes* commissioned *Lentus Composites* and the author to develop a replacement fan blade design and then manufacture a prototype for testing.

The main body of work identifies the required design targets to match the current original blades' performance achieved through the development of testing methods and carrying out analysis of the blade characteristics. These performance targets formed the basis of the subsequent design and specification capable of manufacture of the new replacement blade.

Acknowledgements

I would like to acknowledge Kelvin Lake for the continued guidance and support throughout the project and in the use of *Design Studio*.

To Tim Tudor special thanks for the opportunities, guidance, mentoring and infinite time over the past 5 years in helping achieve my accomplishments to date.

I would like to say thank you to Graham Miller for the opportunity of working on the fan blade project with *Mercedes*.

To Nolan Richmond I would like to say a special thank you for the support in my professional development and continued guidance over the past year. Also for entrusting me with the opportunity of this project.

Thank you to Graeme Hyson for sharing his extensive composite knowledge, engineering guidance and FEA skills throughout this project.

Thank you to Vijay Kuner and Stephane Helle for support over the last year with the project. A thank you to everyone else at *Lentus Composite* for contributing to the expansion of my knowledge base

Finally, thank you to Nigel Spring-Benyon and Owen Spring-Benyon for the support over the past 5 years throughout my university experience and helping me achieve my goals.

TABLE OF CONTENTS

TABLE OF FIGURES 8
TABLE OF GRAPHS 13
TABLE OF TABLES 14
TABLE OF EQUATIONS 15
1. INTRODUCTION 16
1.1 Background To Project 16
1.2 Principal Challenges At Project Inception 17
1.3 Project Aims 17
1.4 Project Plan & Gateways 18
1.5 Structure Of The Design Team Behind The Project 19
2. LITERATURE REVIEW 20
2.1 Wind Tunnel & Wind Tunnel Blades 20
2.1.1 Mercedes wind tunnel 20
2.2 Wind Tunnel Blade Design 21
2.2.1 Blade loading 22
2.2.2 Axial blade thrust calculations 25
2.2.3 Torsional distribution using 2-D CFD package 26
2.2.4 Blades vibration dynamics 26
2.2.5 Blade design features and blade material 28
2.2.5 Manufacturing techniques 30
2.3 FEA & Composite Material Principles 30
2.3.1 Design studio optimisation 31
3. OUTCOMES FROM LITERATURE REVIEW 32
4. INITIAL LOADING CALCULATIONS, RESULTS & TESTING RIG DESIGN 33
4.1 Blade Aerodynamic Load & Distribution 33
4.1.1 Wind tunnel information from Mercedes 33
4.1.2 Bending load distribution 33
4.1.3 Torsional distribution 37
4.2 Stiffness Rig Design 38
4.2.1 Whiffletree design 38
4.2.2 Overall scheme 39
5. TESTING RESULTS 42
5.1 Initial Testing Results 42

5.1.1 Bending load testing results 43
5.1.2 Torsional load testing results 44
5.2 Whiffletree Testing Results 46
5.2.1 Potential errors 47
5.2.2 Results 49
5.3 Blade Frequencies Testing Results 52
5.3.1 Tap testing results 52
5.3.2 LDV results 53
5.4 Existing Blade Mass Testing Results 55
5.4.1 Blade total weight 55
5.4.2 Blade centre of gravity measurement 55
6. REPLACEMENT BLADE DESIGN TARGETS 56
6.1 Replica Blade Principal Design 57
7. FEA METHODOLOGY 58
7.1 Mesh Strategy 58
7.1.1 Blade assembly meshing categories 58
7.1.2 Mesh connection methods 59
7.1.3 Mesh density 59
7.1.4 Other elements used in the model 60
7.2 Model Loading 61
7.2.1 Applying the stiffness testing load 61
7.2.2 Applying the centrifugal load 62
7.2.3 Applying centrifugal & stiffness load 63
7.3 Model Constraints 64
7.4 Design Optimisation Set Up 66
7.4.1 Objectives 66
7.4.2 Constraints 66
7.4.3 Design variables 67
7.4.4 Composite ply topometry 67
7.5 Summary Of The FEA Model 67
8. INITIAL DESIGN & RESULTS 70
8.1 FEA Model 71
8.2 Initial Blade Layup 72
8.3 FEA Stress Results 74

8.3.1 Bending load 74
8.3.2 Torsional load 77
8.3.3 All 3 loads 78
8.4 FEA Natural Frequency Results 80
8.5 Points To Take Into The Next Design 82
9. MANUFACTURING CONSIDERATIONS 83
9.1 Tooling Scheme 83
9.2 Composite Consolidation 84
9.3 Load Transfer 86
9.4 Blade Mass Control 89
9.5 Optimisation Ply Shape Control 90
10. PROJECT ERRORS & SOLUTIONS 94
10.1 Composite Material Error 94
10.1.1 Solution 97
10.2 FEA Model Glue Contact Error 97
10.2.1 Solution 99
10.2.2 Study results 100
10.2.3 Outcome from study 103
11. FINISHED DESIGN & FEA RESULTS 105
11.1 Blade Design Overview 105
11.1.1 Foot design 105
11.1.2 Shroud area design and foam core 108
11.2 FEA Stiffness Results Of Final Design 109
11.2.1 Blade stiffness 111
11.2.2 Composite stress 114
11.2.3 Composite failure index 114
11.2.4 Material parameter study 115
11.3 FEA Stiffness & Centrifugal Load Results Of Final Design 117
11.3.1 Composite stress 117
11.3.2 Composite failure index 118
11.3.3 Composite strain 119
11.3.4 Other composite part results 120
11.3.5 Foot stress 122
11.3.6 Core stress 123

11.3.7 Other solid parts stress 123
11.3.8 FEA natural frequency results 124
11.3.9 Bond stress between laminate and core/foot 126
11.3.10 Attempts to reduce the bond stress 128
11.4 Summary Of Finished Design 135
11.4.1 Reserve factors 136
12. CONCLUSIONS AND EVALUATION 138
13. FURTHER WORK 140
14. REFERENCES 141
Appendix A – FEA & Composite Material Principles 144
Appendix B – Testing Methodology 149
Appendix C – Blade Assembly Meshing Categories 155
Appendix D – Mesh Connection Methods 158
Appendix E – Mesh Density 167
Appendix F – Model Quality Checks 169
Appendix G – Blade Bill Of Materials 171
Appendix H – Blade Design 2 174
Appendix I – Blade Design 5 180
Appendix J – Extra Information 183

TABLE OF FIGURES

Figure 1 intended timing chart 18
Figure 2 project gateways 18
Figure 3 project supporting structure 19
Figure 4 closed loop wind tunnel construction (Katz, 1995) 20
Figure 5 Mercedes AMG F1 Wind Tunnel 2 (Mercedes AMG F1, 2018) 21
Figure 6 Blade load distribution graphs (Fagerberg & Stromberg, 2007) (Lee, 2008) 22
Figure 7 NASA whiffletree testing a wing (NASA, 2011) 24
Figure 8 Moham turbine blade vibration analysis results (Moham, 2014) 27
Figure 9 system block diagram 28
Figure 10 illustrating the three main parts of the Mercedes blade design 29
Figure 11 RTM process (Mattews & Rawlings, 1994) 30
Figure 12 CreaForm MetraScan equipment (CreaForm, 2019) 32
Figure 13 scan data into blade CAD model 32
Figure 14 the 8 load points on the blade for the testing 34
Figure 15 testing rig blade profile clamp 35
Figure 16 F&S CFD pressure distribution results (Fagerberg & Stromberg, 2007) 36
Figure 17 2D sketch of one of the profile shapes 37
Figure 18 the whiffletree construction 38
Figure 19 showing the whiffletree applying the load offset along the blade 39
Figure 20 stiffness rig 39
Figure 21 showing the blade mounted with the base perpendicular to the loading direction 40
Figure 22 showing the blade mounted with the tip perpendicular to the loading direction 40
Figure 23 blade mounted on the rig at 17° offset 40
Figure 24 GOM camera tracking system 41
Figure 25 initial 'stiffness testing rig' design 42
Figure 26 the current blade being tested with the DTi's 42
Figure 27 ideal way of loading the blade to create torsional load 44
Figure 28 the way the blade was loaded as a compromise to achieve torsional load 45
Figure 29 illustrating original idea for the GOM system 46
Figure 30 steel pillars supporting the rig obscuring GOM cameras 47
Figure 31 compromise position for the GOM cameras 47
Figure 32 showing the points used to check blade movements relative to the profile clamp 48
Figure 33 magnitude of blade displacement at 5020.4N 49
Figure 34 Y component from the test 50
Figure 35 X component displacement 51
Figure 36 tap testing results 52
Figure 37 LDV and F&S results of the first mode shape (Fagerberg & Stromberg, 2007) 54
Figure 38 LDV and F&S results of the second mode shape (Fagerberg & Stromberg, 2007) 54
Figure 39 LDV and F&S results of the third mode shape (Fagerberg & Stromberg, 2007) .. 54
Figure 40 LDV and F&S results of the forth mode shape (Fagerberg & Stromberg, 2007) .. 55
Figure 41 illustration of the seesaw used for find the CoG Z distance 55
Figure 42 main parts forming the new blade design 57
Figure 43 profile clamps modelled into the blade FEA model 60
Figure 44 bolt numbering 61
Figure 45 showing where the load was applied to the profile clamp 62

Figure 46 is an illustration of how the centrifugal would be applied 63
Figure 47 showing how both loads are applied at the same time 64
Figure 48 how F&S set up their model constraints (Fagerberg & Stromberg, 2007) 64
Figure 49 the three different ways that where tested 65
Figure 50 example of the nodes picked for a displacement constraint 67
Figure 51 example of a complete FEA model of the blade 68
Figure 52 main parts that go into the blade FEA model 68
Figure 53 first foot design compared to F&S design (Fagerberg & Stromberg, 2007) 70
Figure 54 interaction between the foot and core 70
Figure 55 comparing the UD 0 plies current blade to new blade (Fagerberg & Stromberg, 2007) 71
Figure 56 blade FEA model for the initial design 72
Figure 57 initial design composite layup 73
Figure 58 initial blade design FEA displacement results 74
Figure 59 bending load ply 1 major principle stress 75
Figure 60 bending load ply 1 minor principle stress 75
Figure 61 potential failing points of the composite 76
Figure 62 illustration of the stress lines on the blade 76
Figure 63 bending load Tsai-Wu failure index 76
Figure 64 bending load foot Von Mises stress 77
Figure 65 torsional load Tsai-Wu failure index 77
Figure 66 failing points of the composite under all 3 loads 78
Figure 67 Tsai-Wu failure index for all 3 loads 79
Figure 68 all 3 loads foot Von Mises stress 79
Figure 69 all 3 loads foam core Von Mises stress 80
Figure 70 initial blade design 1st mode 80
Figure 71 initial blade design 2nd mode 81
Figure 72 initial blade design 3rd mode 81
Figure 73 initial blade design 4th mode 81
Figure 74 mould assembly (Lentus Composites, 2019) 83
Figure 75 both ways of laying up the blade (Lentus Composites, 2019) 84
Figure 76 assembling blade into the mould (Lentus Composites, 2019) 84
Figure 77 Applying autoclave pressure (Lentus Composites, 2019) 85
Figure 78 applying pressure to shroud area (Lentus Composites, 2019) 85
Figure 79 silicone parts (Lentus Composites, 2019) 85
Figure 80 assembly parts in shroud area 86
Figure 81 F&S foot design (Fagerberg & Stromberg, 2007) 87
Figure 82 Antonio Paolozzi composite wing (Paolozzi, 2006) 87
Figure 83 composite spars 88
Figure 84 laying up spars 88
Figure 85 comparing updated foot with first design 89
Figure 86 current blade shroud 90
Figure 87 blade back plate 90
Figure 88 updated composite mesh 91
Figure 89 optimised composite layup 91
Figure 90 optimised composite layup for manufacturing 92
Figure 91 Helius Composite software with optimised layup 93
Figure 92 blade design 2 maximum Tsai-Wu failure index 94

Figure 93 blade design 2 individual ply Tsai-Wu failure index 95
Figure 94 blade design 2 induvial ply minor principle stress 96
Figure 95 glue contact mesh forces 97
Figure 96 glue traction on old settings 98
Figure 97 Jonathan Buck's FEA glue traction results (Buck, 2014) 98
Figure 98 resultant glue traction contour arrows on old settings 99
Figure 99 Graeme Hyson glue traction results (Hyson, 2018) 99
Figure 100 coupon model set up 100
Figure 101 coupon results with current settings 100
Figure 102 results of using spring elements glue traction contour arrows 101
Figure 103 comparing FEA results of using glue contacts and spring elements 101
Figure 104 results of using 2mm tets glue traction 102
Figure 105 results of using 1mm tets glue traction 102
Figure 106 results of using new settings from study 103
Figure 107 results of using new settings from study contour arrows 103
Figure 108 foam core glue traction results with new settings 104
Figure 109 foot glue traction results with new settings 104
Figure 110 final foot design 105
Figure 111 main core interacting with foot and updated back plate 105
Figure 112 FEA results with of the foot without modes Von Mises stress 106
Figure 113 foot with fillets and gussets 106
Figure 114 foot with fillets and gussets FEA results Von Mises 107
Figure 115 FEA Von Mises on back of foot 107
Figure 116 foot with cut out to reduce mass 108
Figure 117 FEA Von Mises results of foot with cut out 108
Figure 118 final core and shroud design 108
Figure 119 final composite main blade layup 109
Figure 120 final composite main blade layup locations and ply orientation 109
Figure 121 first spar layup with layup locations and ply orientation 110
Figure 122 spar layup including woven materials 110
Figure 123 spar layup including woven ply locations and ply orientation 111
Figure 124 total composite thickness across the blade 111
Figure 125 blade deflection under stiffness rig load 112
Figure 126 worst stressed plies under stiffness rig load major principle stress 114
Figure 127 worst stressed plies under stiffness rig load minor principle stress 114
Figure 128 maximum Tsai-Wu failure index 115
Figure 129 material properties tested 116
Figure 130 different material properties blade displacement results 116
Figure 131 different material properties blade maximum Tsai-Wu failure index results 117
Figure 132 worst stressed plies under stiffness rig and centrifugal load major principle stress 118
Figure 133 worst stressed plies under stiffness rig and centrifugal load minor principle stress 118
Figure 134 maximum Tsai-Wu failure index from both loads 119
Figure 135 maximum strain 120
Figure 136 spar composite FEA results 121
Figure 137 shroud composite FEA results 122
Figure 138 foot FEA results Von Mises 123

Figure 139 foam core FEA results Von Mises 123
Figure 140 silicone parts FEA results Von Mises 124
Figure 141 steel sleeves FEA results Von Mises 124
Figure 142 final design FEA results of 1st mode 125
Figure 143 final design FEA results of 2nd mode 125
Figure 144 final design FEA results of 3rd mode 125
Figure 145 final design FEA results of 4th mode 126
Figure 146 glue traction results 127
Figure 147 glue traction on the foot using spring elements 127
Figure 148 comparing failure index's 128
Figure 149 spar interlaminar shear strength failure index 128
Figure 150 the zed ply on the steel foot 129
Figure 151 FEA results of adding in the zed plies glue traction 129
Figure 152 illustrating the 90° plies going into tension 130
Figure 153 comparing the FEA results of the foot with and without a taper 131
Figure 154 foot with extended foot taper 131
Figure 155 FEA results of extended taper foot glue traction 132
Figure 156 comparing FEA results of the foot with and without extended taper interlaminar shear strength failure index 132
Figure 157 tapered foot Von Mises stress FEA results 133
Figure 158 illustrating having stiffer composite section near the foot then dropping off along the blade span 133
Figure 159 FEA results of extended taper foot glue traction 134
Figure 160 blade being attached to testing rig 149
Figure 161 calibrating GOM system 150
Figure 162 tracking blade before attaching clamps 150
Figure 163 attaching clamps 150
Figure 164 calibrating load cell 151
Figure 165 blade fully set up for testing 151
Figure 166 testing blade 152
Figure 167 mesh of 44 accelerometers 153
Figure 168 LDV amplifier on tap testing rig 153
Figure 169 set up of the LDV testing 154
Figure 170 showing the difficulties with meshing the complex geometry 156
Figure 171 bar model for correlation study 156
Figure 172 showing how the plate mesh would overlap with the complex geometry 157
Figure 173 coupon construction 158
Figure 174 coupon sections and measurements 159
Figure 175 FEA model of coupon with glue contact regions connecting the meshes together 160
Figure 176 FEA coupon model with spring elements connecting the meshes together 161
Figure 177 FEA coupon model with RB2s connecting the meshes together 162
Figure 178 FEA coupon model colour contour results 163
Figure 179 comparing the results of the glue contacts and plate mesh model 164
Figure 180 coupon constructions 164
Figure 181 testing rig for the coupon 164
Figure 182 manufactured coupon 165
Figure 183 aluminium holding rig with coupon 165

Figure 184 results of the constraint test 170
Figure 185 composite spar attached to the foot 174
Figure 186 the two variables for the spar 174
Figure 187 blade design 2 foot 176
Figure 188 foot back plate 177
Figure 189 silicone parts and shroud core parts 177
Figure 190 FEA stress results of design 2 composite with updated parts 178
Figure 191 blade design 2 composite failure index results 178
Figure 192 FEA stress results of foot and main foam core 178
Figure 193 displacement FEA results of blade design 5 180
Figure 194 optimised composite layup design 5 181
Figure 195 optimised composite layup for manufacturing to move project forward 182
Figure 196 excel load distribution calculations 183
Figure 197 excel spreadsheet construction to calculate the distance between pin joints for the right load distribution 184
Figure 198 final blade layup (Lentus Composites, 2019) 185

TABLE OF GRAPHS

Graph 1 blade pressure distribution with outlet speed set to 80m/s 34
Graph 2 results of changing the outlet velocity 35
Graph 3 load distribution along the span of the blade 35
Graph 4 results of the CoP CFD analysis of the 2D profiles (100% is the leading edge of the profiles) 37
Graph 5 bending load deflection along the span 43
Graph 6 force increasing against deflection of points 3 and 5 from the bending test 44
Graph 7 loading at leading edge and torsional load results 45
Graph 8 loading at trailing edge and torsional load results 46
Graph 9 results of comparing the displacement between the 5 sets of data 48
Graph 10 Y component displacement against load 50
Graph 11 all the points' magnitude displacement against load 51
Graph 12 LDV magnitude frequency results 53
Graph 13 results of constraining the blade model 66
Graph 14 initial blade design bending load FEA displacement results compared to test data 73
Graph 15 initial blade design torsional load FEA displacement results compared to test date 74
Graph 16 comparing the blade FEA defection against test bending data 78
Graph 17 comparing FEA blade magnitude displacement against testing results point 1 .. 112
Graph 18 comparing FEA blade magnitude displacement against testing results point 4 .. 113
Graph 19 comparing FEA blade magnitude displacement against testing results point 7 .. 113
Graph 20 mesh type study results 157
Graph 21 testing glue contact regions FEA correlation results 161
Graph 22 testing RB2 and spring elements FEA correlation results 162
Graph 23 comparing the best connection results between the each method 163
Graph 24 mesh density study results 168
Graph 25 spar length results 175
Graph 26 spar overhang results 175
Graph 27 comparing FEA blade magnitude displacement against testing results point 1 of design 5 180
Graph 28 comparing FEA blade magnitude displacement against testing results point 4 of design 5 181
Graph 29 comparing FEA blade magnitude displacement against testing results point 7 of design 5 181

TABLE OF TABLES

Table 1 scheme of work 32
Table 2 base wind tunnel information (Miller, 2018) 33
Table 3 profile clamp load 36
Table 4 torsional distribution points 38
Table 5 magnitude displacement data to be used as constraints 52
Table 6 blade design targets 56
Table 7 data used to calculate the bolt stiffness's and stiffness results 60
Table 8 loads applied to FEA model 62
Table 9 summary of the settings used to define each part within the model 69
Table 10 showing a un-balanced layup 92
Table 11 final design performance against the design targets 135
Table 12 blade parts safety factors 136
Table 13 blade load reserve factors 137
Table 14 loads used for the coupon study 158
Table 15 validating the hand calculation results 160
Table 16 results of testing the coupon 165
Table 17 results of testing coupon with new I value 165
Table 18 results of FEA model with rig compared to testing 166
Table 19 nodes and elements numbers over 8 runs 167
Table 20 Rohacell IG-F 71 properties data (Evonik, 2019) 171
Table 21 composite material properties (Torayca, 2018) (TenCate, 2018) 172
Table 22 silicone propteries (Alchemie, 2019) 172
Table 23 15-5P properties (AK Steel) 173
Table 24 304 properties (AZO Materials, 2001) 173

TABLE OF EQUATIONS

Equation 1 centrifugal force 23
Equation 2 resolving blade velocity 25
Equation 3 Bernoulli's 25
Equation 4 coefficient of pressure 25
Equation 5 calculating blade force 25
Equation 6 calculating the coefficient of pressure point 26
Equation 7 centrifugal force 63
Equation 8 centrifugal force at 550RPM 63
Equation 9 gravitational load 63
Equation 10 gravitational load numbers 63
Equation 11 FEA solution matrix 144
Equation 12 displacement from stiffness matrix 144
Equation 13 element stiffness matrix 144
Equation 14 transformation matrix 144
Equation 15 element force 144
Equation 16 orthotropic stiffness terms 145
Equation 17 Composite rule of mixtures equation (Bheemreddy, 2014) 145
Equation 18 Kinematic Equations (Bheemreddy, 2014) 146
Equation 19 Constitutive Equations (Bheemreddy, 2014) 146
Equation 20 Resultants (Bheemreddy, 2014) 146
Equation 21 Equilibrium Equations (Bheemreddy, 2014) 147
Equation 22 CLT replaced equation (Bheemreddy, 2014) 147
Equation 23 Integrated CLT (Bheemreddy, 2014) 147
Equation 24 ABD stiffness equation (Bheemreddy, 2014) 147
Equation 25 148
Equation 26 Tsai-Wu failure theory (Kaw, 2006) 148
Equation 27 max bending deflection 159
Equation 28 parallel axis theorem 159
Equation 29 max bending deflection formula for the coupon 159
Equation 30 max deflection under tension load 159
Equation 31 max deflection under tension load formula for the coupon 159
Equation 32 working out the spring element stiffness 161

1. INTRODUCTION

This report details the work carried out and submitted for consideration as a 3rd year undergraduate project in support of a BEng (Hons) degree (Motorsport Engineering and Design) adjudicated and awarded by the University of Wales Trinity Saint David.

The work is an on-going commercial project with its origins evolving during the authors period of industry placement where, after gaining valuable experience, was appointed by his employer *Lentus Composites* to liaise with their client *Mercedes AMG Petronas* to assist with developing solutions for retro design and manufacture of replacement wind tunnel fan blades.

1.1 Background To Project

The *Mercedes AMG Petronas' F1 Teams* aerodynamics department operate an aerodynamic wind tunnel facility. A major component is the motor-fan unit which is made up of individual fan blades. Currently, *Mercedes* do not hold any spare blades in the event that one or more fails and requires replacement. There is therefore a risk that projects using the wind tunnel facility could be delayed and disrupted with corresponding impact on cost. To minimise the risk of the tunnel facility being out of operation, *Mercedes* have identified the need to have available spare fan blades.

The existing fan blades are of a composite construction. They were originally designed and manufactured by *Flex Prop* in 2004. For commercial reasons not revealed *Mercedes* have not returned to the original manufacturer to obtain additional blades preferring instead to commission *Lentus Composites*, a company specialising in bespoke composite manufacturing, in the first instance, to perform a reverse engineering investigation to determine design criteria and manufacturing process for a like for like single replacement blade. It is this work embarked upon and entrusted to the author to successfully fulfil this commission that forms the basis of this final year undergraduate honours degree project.

1.2 Principal Challenges At Project Inception

The project aims (detailed in Section 1.3) were largely influenced by the absence of information on the original design and construction of the existing blades essential to achieve a simple replication. As a consequence, the assignment was complex with multiple unknowns requiring evaluation as well as considerable computation analyses and testing of an existing blade.

Original data/information that was not available:

- Specification for fan module operation, including limits
- Blade loading conditions (subsequently assumed); including parameters for torsion, fatigue and vibration
- Behaviour characteristics under varying loading conditions and outputs of analysis undertaken
- Final design concepts adopted
- Actual profile of material used in composite blade construction
- Manufacturing techniques/process

Data available:

- *Mercedes* actual operating conditions and self-limits
- Inspection of actual wind tunnel facility
- Fan blade supplied by *Mercedes* from which dimensions and surface cross section profile were determined as well as being subjected to non-destructive load testing (It was not available for destructive examination of internal core material and construction techniques deployed)

1.3 Project Aims

- Investigate the current blade loading
- Identify blade performance requirements
- Design and build testing rigs
- Test current blade performance
- Identify achievable design targets for the new blade
- Build FEA methodology and create FEA model
- New blade design to achieve design targets
- The new blade design to be manufactory viable

The project aims were developed after reviewing literature and carrying out initial testing to see if the project was achievable and to understand the scope.

1.4 Project Plan & Gateways

The intended project planning Gantt chart can be seen in Figure 1.

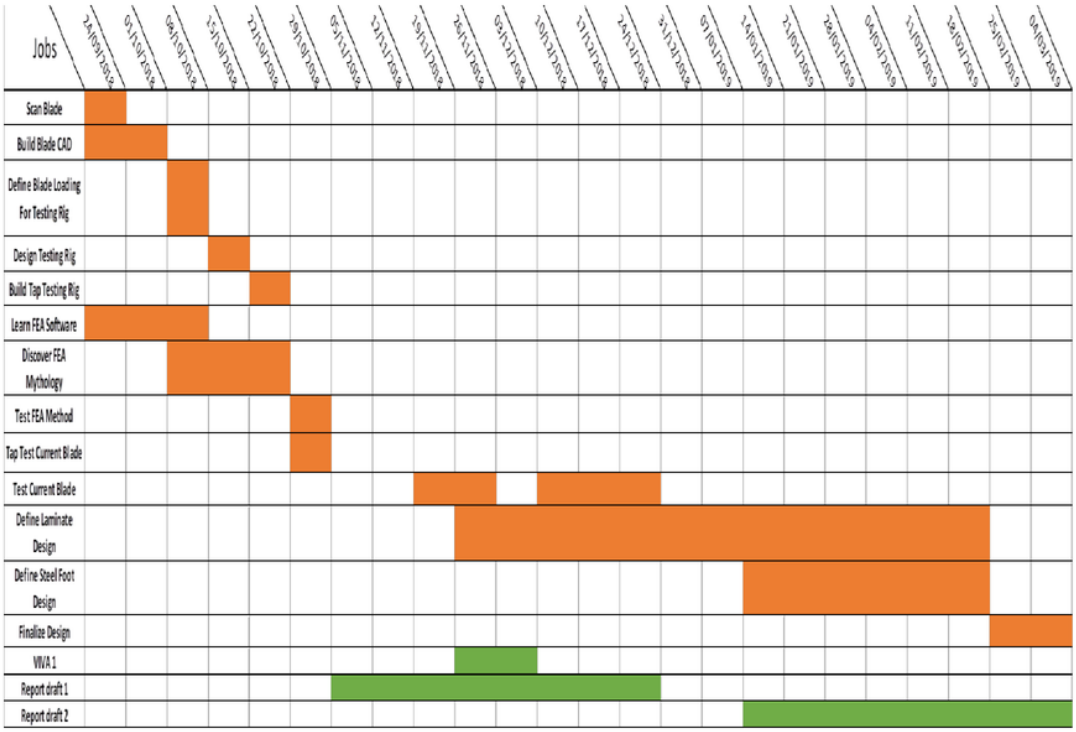


Figure 1 intended timing chart

The plan was developed after an initial project review and exploration of testing required. Below are the gateways associated with achieving the project aims and executing the project plan:

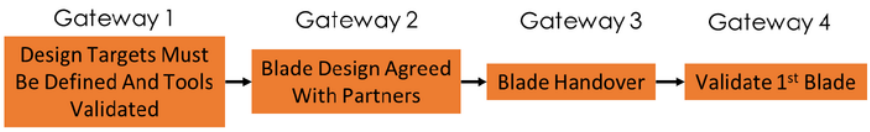


Figure 2 project gateways

Each gateway was set to be achieved before moving to the next stage. This report covers up to Gateway 3 which at that point the project is handed over to *Lentus* to complete.

1.5 Structure Of The Design Team Behind The Project

The project was conducted working alongside the engineers at *Lentus*. The engineers are at the cutting edge of composite technology and *Lentus* is contracted to sell the new replica blade to *Mercedes*. Consequently, throughout this project, aspects of the analysis and decisions were made in conjunction with *Lentus*. This meant there was a structure as to who made the final decisions and mentored the work of Gavin Spring-Benyon (the author), together with how the tasks were allocated through the life of the project. The following flow chart sets out the supporting structure:

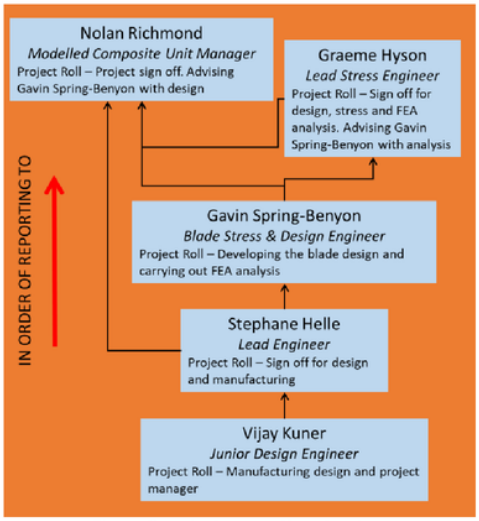


Figure 3 project supporting structure

Nolan Richmond and Graeme Hyson both have vast experience in this type of project. This experience was used as references to back up the findings/outputs of Gavin Spring-Benyon; particularly important in the absence of very little/no published research or literature to provide guidance on blade design, loading and analysis.

2. LITERATURE REVIEW

2.1 Wind Tunnel & Wind Tunnel Blades

Automotive wind tunnels are a vital tool in developing aerodynamic devices and assist in validating computational fluid methods of analyses (Katz, 1995). Wind tunnels come in two different types; closed and open loop. The *Mercedes AMG F1* facility is a closed loop wind tunnel comprising segments of variable cross section and function illustrated in Figure 4.

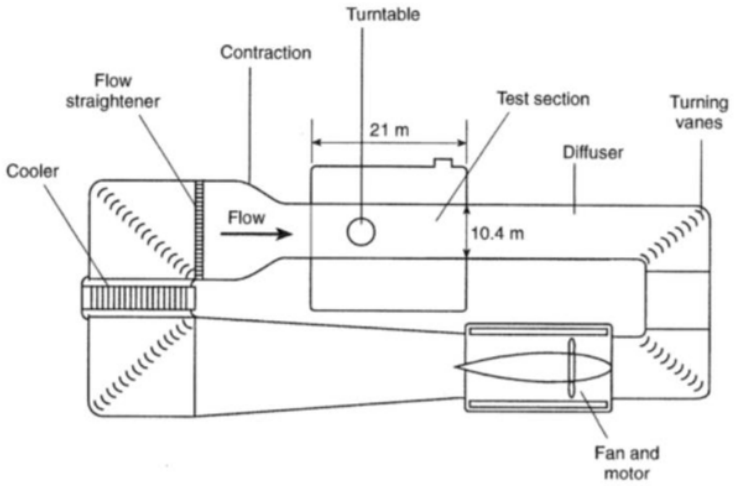


Figure 4 closed loop wind tunnel construction (Katz, 1995)

The air speed in a closed loop wind tunnel is generated by an axial fan comprising blades manufactured from a variety of materials including aluminium, carbon fibre and composites. (Katz, 1995). The axial fan is designed to generate a large volume of flow without inducing large pressure differences within the tunnel. Further, axial fans are optimised to minimise sound excitation particularly if the tunnel is designed specifically for acoustic tests. Low sound emission from the operation of the tunnel is crucial for accurate measurements of sound excitation. An automotive wind tunnel and/or an acoustic wind tunnel can be considered to be precision equipment in a demanding application where the blade design is crucial for its optimum measurable performance with minimal energy losses (Fagerberg & Stromberg, 2007).

2.1.1 Mercedes wind tunnel

Mercedes AMG F1 have two wind tunnels: one being a full scale testing facility for automotive use (Tunnel 1) and the other being 60% scale for the formula one racing team development (Tunnel 2). The composite blades analysed and subject of this project are those forming the axial fan in Tunnel 2 (Miller, 2018).

Tunnel 2 is a closed loop temperature controlled single axial rotor wind tunnel. *Mercedes* advised the max rotor speed of 550 RPM is capable of generating wind speeds up to 80m/s. The air circulation is forced by a 2.2MW motor which drives 1.5m long carbon fibre composite blades (overall fan diameter of 3m). Other features of the wind tunnel include in-built rolling road, adaptive wall system and yaw and pitch control (Mercedes AMG F1, 2018) (Miller, 2018).



Figure 5 Mercedes AMG F1 Wind Tunnel 2 (Mercedes AMG F1, 2018)

2.2 Wind Tunnel Blade Design

A report by Fagerberg and Stromberg (F&S) looking into the required design characteristics of modern day composite rotor blades found that most closed loop wind tunnel rotors are equipped with short blades housing a slender design. A blade had to meet the demands of a tunnel by utilising materials with high strength and stiffness values, but is also lightweight enough to reduce centrifugal loading when in operation. Fagerberg discusses how carbon fibre fulfils the modern day requirements of a blade with it being lightweight, having high tensile capabilities and being versatile when manufacturing complicated shapes (Fagerberg & Stromberg, 2007).

Incidentally, one surprising outcome of the literature review was the realisation that the F&S report on fan blades was centred on design of a composite blade for *Flex Prop* wind tunnels and was the same or similar blade used in the *Mercedes* wind tunnel 2 axial fan.

F&S go on to suggest that a tunnel rotor blade needs to have the following criteria considered when designing the optimised blade:

- 1st natural frequency of the final design
- Must be cost effective
- Strength
- Geometrical tolerance
- Impact and toughness

- Attachment details to the rotor hub

Unsurprisingly one of the main blade design parameters is the aerodynamic profile and shaping. However the profile design in this instance is already set, this being a reverse engineering replication project. Therefore there is little that can be optimised if the project output is to achieve an individual replacement matching the remaining set of blades.

2.2.1 Blade loading

F&S report suggests there are 3 main loadings acting on the blades. They are:

1. Bending aerodynamic load caused by low pressure fields.
2. Torsional load from the low pressure fields distribution across the span.
3. Centrifugal load generated by the mass of the blade being spun at high speed.

These loading characteristics are supported by Ki-Sang Lee in a paper looking into the aerodynamic optimisation of low speed axial fan flow which found the same loadings scenarios as F&S (Lee, 2008). A further reinforcement of these considerations is verbal evidence offered by Nolan Richmond (*Lentus Composites* moulded composite's Aerospace engineer) who concurred with the findings of the two papers (Richmond, 2018).

The distribution of the aerodynamic load in both F&S and Lee's papers found that blades are aerodynamically designed to evenly distribute the aero load across the span as much as possible to achieve a target uniformly distributed load particularly with bending kept even longitudinally and as much as possible near to the centre to reduce the torsional moment (Fagerberg & Stromberg, 2007) (Lee, 2008). Both papers found, through computational fluid dynamics, the following pressure distributions and surface velocity traces:

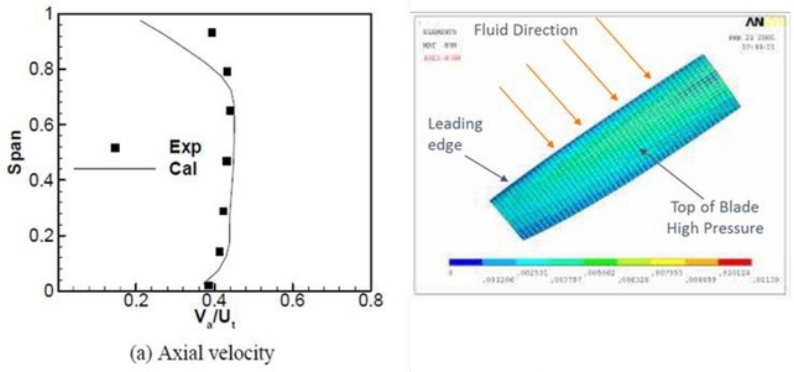


Figure 6 Blade load distribution graphs (Fagerberg & Stromberg, 2007) (Lee, 2008)

The graph on the left in Figure 6 shows that the velocity (black square markers) along a blade's span stays fairly even. The pressure plot on the right is the findings of F&S which shows a high pressure contour on top of the *Mercedes* wind tunnel 2 blade. The pressure contour illustrates a fairly even pressure along the span with a slight bias to the blade tip.

The *Mercedes* blade has a twisted profile along the span to replicate a higher angle of attack (AoT) at the blade base as incoming velocity speeds will be lower. Moving out from the base, the blade twist becomes less aggressive to reduce AoT as incoming velocity speeds increase (Fagerberg & Stromberg, 2007). The changing angle of attack along the span supports the theory of attempting to achieve a uniformly distributed load along the blade. This design reasoning is also applied to jet engine blades. A report by LI Yang tests the performance of jet engine blades and finds blades are twisted to try and give equal thrust and load distribution. In addition Yang finds there is tendency for axial flow blades aero load to be in the upper mid-span area, which matches up to the pressure contours found by F&S (Yang, 2007).

The following can be concluded from the available literature looking into blade loading:

- The *Mercedes* wind tunnel 2 blade has three principal loading conditions of bending, torsional and centrifugal load when considering the structural design of the blade.
- There appears to be no published research/literature providing guidance on blade loading values or percentage of the distribution in typical operating scenarios; only pressure plots as an indication of likely load distribution.
- There is a considerable amount of research data on jet engine turbine blades; however these concentrate on blade vibration rather than loading.
- F&S used FEA and optimisation techniques in structural design of a fan blade (Fagerberg & Stromberg, 2007).

There is no literature providing the values for bending and torsional load on the current blade. However the centrifugal loading of the blade can be calculated. A report by *NASA* calculated the centrifugal force for wood blades on a wind tunnel fan from:

$$CF = m \times \omega^2 \times r$$

Equation 1 centrifugal force

The report goes on to say that m is the mass of the body in rotation and r is the body's centre of gravity point distance from the axis of rotation (NASA, 1998). This is a simple but effective way of identifying the centrifugal loading for *Mercedes* blade.

As the design brief is limited to design a like for like blade it is not necessary to know the full bending and torsional load. Instead, testing the current blade can determine the torsional and bending stiffness. The results can then be utilised as the design targets for the new replica blade. If however a blade was not available for testing, then the aerodynamic loads could be found from computational fluid dynamics software such as *ANSYS* which was the method F&S used. (Fagerberg & Stromberg, 2007).

Most smaller blades are tested for stiffness by using a single point load and measuring the displacement. However, a paper by *NASA* looking into the best practice for testing of wings and blades, found the preferred testing method for validating designs is using a whiffletree rig (see Figure 7). A whiffletree rig allows loading the blade with bending and torsional loads at the same time and gives freedom for distributing load un-evenly across the span of the wing/blade. The whiffletree distributes the load from a single point through beams pivoting in tension which are connected by cables. The load is applied to the wing/blade surface through profile clamps. (NASA, 2011) *NASA's* recommendations are backed up by Nolan Richmond's advice from his previous experience at *GKN,* validating wing designs (Richmond, 2018).

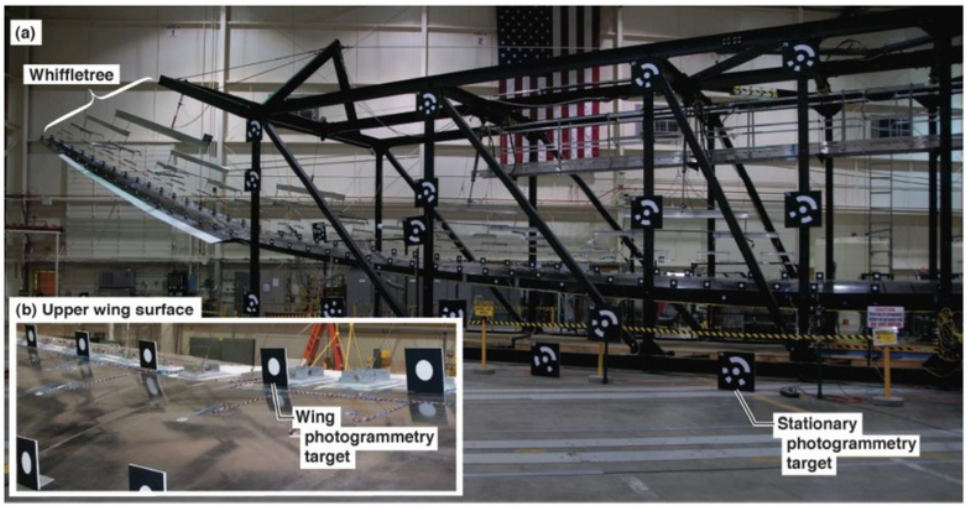


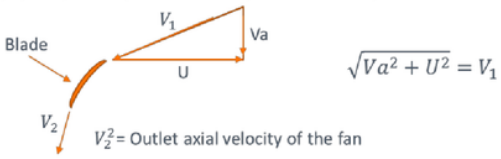
Figure 7 NASA whiffletree testing a wing (NASA, 2011)

The whiffletree rig gives the possibility of being as close as possible to how the blade is loaded from aerodynamics. However whiffletrees are designed from knowing the percentage of load distribution across the span and chord length (NASA, 2011). F&S's report does provide a pressure contour figure of the blades loadings, but this is not substantial enough to base a decision on the percentage of loading acting on the blades surface (Fagerberg & Stromberg, 2007). Advice from Nolan Richmond from past experience designing wings and whiffletrees advised that it is possible to find the blade/wing loading span spread (bending load) from using simple jet engine blades thrust calculations; and find the point at which it acts along the blade chord (torsional) (coefficient of pressure point) from using 2-D aerofoil analysis software (Richmond, 2018). Using a combination of results from calculations and F&S's pressure contour figure it is considered enough data to design an appropriate whiffletree rig for test loading the existing fan blade.

2.2.2 Axial blade thrust calculations

A seminar by the *Cranfield University* (Cranfield University, 2008) into the jet engine design, expressed the steps to find blade load distribution as follows:

1. **Blade velocity resolving from Pythagoras theorem –** V_1^2 = Inlet velocity to the blade V_1= The axial velocity Va + the blade rotation velocity speed U.
   $U = \omega(RPM\ of\ fan) \times r\ (the\ radis\ of\ the\ blade\ from\ the\ rotation\ axis)$.



$$\sqrt{Va^2 + U^2} = V_1$$

Equation 2 resolving blade velocity

2. **Using Bernoulli's to find the pressure difference across the blade –**

$$\Delta p = \frac{1}{2}\rho V_1^2 - \frac{1}{2}\rho V_2^2$$

Equation 3 Bernoulli's

3. **Calculate the coefficient of pressure** – it is being assumed that the axial fan is in steady state and the temperature is set at 20°C.

$$\boldsymbol{Cp = \frac{\Delta p}{q}} \quad \boldsymbol{q = 1/2\rho V^2}$$

$$V^2 = V_1^2$$

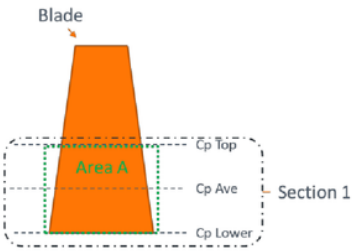
Equation 4 coefficient of pressure

4. **Calculating the force acting on blade from coefficient of pressure** - To work out the force acting over the blade in a single section, find the $Cp\ Top$ and the $Cp\ Lower$, thus giving the $Cp\ Ave$ in the middle. Then use the area (A) between the $Cp\ Top$ and $Cp\ Lower$.

$$\boldsymbol{F = Cp \times 1/2\rho V^2 \times A}$$

$$V^2 = V_1^2$$

$$Cp = Cp\ Ave = (Cp\ Top + Cp\ Lower)/2$$



Equation 5 calculating blade force

Using this method has the benefit of understanding the distribution as well as to estimate the total test load.

2.2.3 Torsional distribution using 2-D CFD package

There are many aerofoil 2-D analysis packages; however, *Aero Foil Engineering* is one of only three packages which validate its results against existing aerofoil profile data. It calculates profile coordinates, coefficient of pitch (Cm), coefficient of lift (Cl), and aerodynamic centre (ac) from vortex panel method and integral boundary layer equations (Aerofoil Engineering, 2003).

The coefficient of pressure point (Cp) is calculated from *Aerofoil Engineering* out puts as follows:

$$Cp = \frac{(ac - Cm)}{Cl}$$

Equation 6 calculating the coefficient of pressure point

The Cp represents the moment about which all aerodynamic forces act for a profile, thus giving the torsional load along the blade.

2.2.4 Blades vibration dynamics

F&S found another important aspect to consider when designing the blade; vibration dynamics (part natural frequency) (Fagerberg & Stromberg, 2007).

The vibration modes within blades give different attitude displacement. For example, a paper by R.S Moham carried out analysis on several different steam turbine blade designs and found a similar trend of mode types (Moham, 2014). Between 3 designs they had the following modes:

1. Bending Flutter
2. 2nd bending flutter
3. Torsional flutter
4. And edge bending

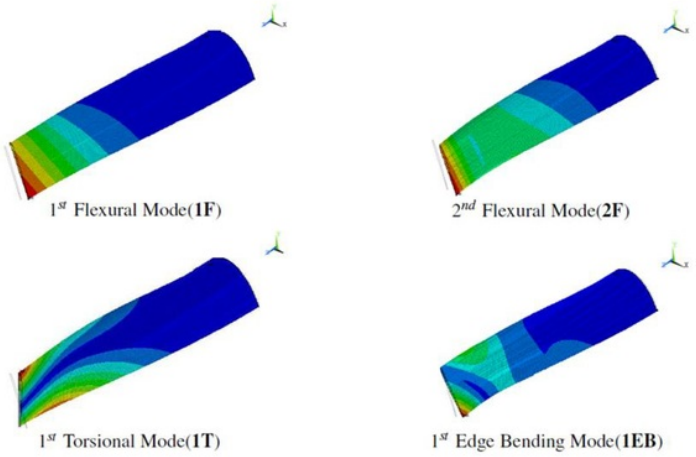


Figure 8 Moham turbine blade vibration analysis results (Moham, 2014)

Another paper looking into design and testing of composite compressor blades also found the same trends as Moham (Wollmann, 2016).

Reverting back to F&S paper, they found through finite element analysis, the first four modes of the blade to be:

1. Flutter
2. Tip torsional
3. Torsional flutter
4. Second load bending

The F&S report states the first mode to be at 38Hz, however when manufacturing the blades this value ranges from 38 to 42Hz (Fagerberg & Stromberg, 2007).

Moham and Wollmanns findings follow a similar pattern. In each paper, the author has obtained their results through FEA and practical testing, with the testing validating their FEA results.

There are a few methods to carry out testing. A common method is Frequency Response function. This works by simultaneously measuring the excitation and output response of the body, which returns the frequency peaks in Hertz (see Figure 9). The peaks from the response represent the different modes of the body. The test can be carried out either 'static' or 'free'. The results obtained from static testing are influenced from being attached to another body as this may increase/decrease the overall stiffness, and/or cause a dampening effect. Free testing is when the body is elastically suspended, which avoids the problem of other bodies affecting the results. The test can be carried out by using a single

accelerometer measuring the response of the body and a force inducer (Agilent Technologies, 2000). This method was used by F&S when correlating their results.

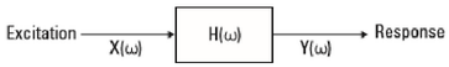


Figure 9 system block diagram

An alternative testing method is laser velocimetry (LDV), which works on the same principle as the Frequency Response function method. However, it obtains results using the Doppler Effect to measure vibrations in components. It works by measuring the light scattered from the vibrating object and detects slight frequency changes. This method can produce the same results as normal tap testing but with the added benefit it can detect displacement changes in a part and predict the mode shape (Polytec, 2018).

2.2.5 Blade design features and blade material

Later on in F&S's report is an explanation of the design of the *Mercedes* blade and in particular the principal design formula derived from years of experience for meeting the needs of wind tunnels. The *Mercedes* blade design is:

- Stainless steel foot in the shape of an H located at the base of the blade. The steel foot allows the rotor attaching bolts to be pre-stressed to avoid the challenge of predicting long term creep properties within the part without putting any compression force onto the composite which could result in relaxation of the joint. In addition, the steel foot would adequately transfer the centrifugal forces to the rotor (Fagerberg & Stromberg, 2007). Creep is the tendency of the material to move slowly or deform permanently when under mechanical stresses. A book by F.L Matthews and R.D Rawlings defined a design technique of using metallic materials pre-stressed in composite constructions which can minimise the creep effect within laminate, almost making it negligible (Mattews & Rawlings, 1994). F&S also have a steel foot in their design to avoid inter-laminar stresses between sharp radiuses from the blade fixing to the tunnel rotor hub (Fagerberg & Stromberg, 2007).
- Creep predictions also applied to the steel foot itself and F&S over engineered the foot to avoid the need for non-linear analysis. F&S took the view of having the highest operation stress value below half of the material yield value, and thus could argue creep in the foot is so minimal that it is negligible as well. This obviates the need for doing FEA analysis into creep (Fagerberg & Stromberg, 2007).
- The main blade profile shape is formed by a PVC foam core. Composite plies are then wrapped around the core (Fagerberg & Stromberg, 2007).

- The blade tip is reinforced with a pre-cured composite piece. This allows for small adjustments of the blade length when being installed in the wind tunnel without exposing the foam core (Fagerberg & Stromberg, 2007).
- The main central laminate comprised UD fibres running in the longitudinal direction wrapping around the blade foot. The UD fibres contribute to the bending stiffness of the blade and transfer centrifuging load to the foot. The plies are layed onto the foam core. The foam core acts as a sandwich composite ultimately increasing the second moment area value of the structure, thus increasing stiffness (Fagerberg & Stromberg, 2007).
- Have UD plies running in a +45/-45 direction to aid the torsional stiffness of the blade (Fagerberg & Stromberg, 2007).
- F&S highlighted the final weight of the blade as one of the most important considerations when developing design. If the component is extremely heavy this will increase the centrifugal load on the wind tunnel rotor dramatically. The consistent weight of each blade manufactured is also important because any big variance in weight between blades can lead to the rotor being un-balanced causing unnecessary vibrations (Fagerberg & Stromberg, 2007).

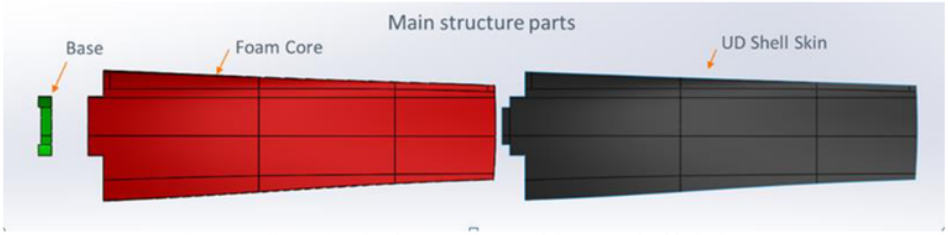


Figure 10 illustrating the three main parts of the Mercedes blade design

There are no papers available which prescribe a wind tunnel fan blade design with the exception of *NASA's* paper, but that was tailored to solid wood blades (NASA, 1998). There is also a lack of published data around composite jet turbine blades structural design. One paper by Amoo states the modern day composite structural design of a jet engine fan blade is comprised of a solid UD laminate with a titanium base. The leading, trailing, and tip of the blade are reinforced with a titanium strip (Amoo, 2012).

There appears to be very little literature exploring composite materials used in fan blades. F&S state a combination of UD carbon fibre and a cold cure epoxy resin matrix as a good formula for successful blade design (Fagerberg & Stromberg, 2007). Amoo states the same with jet engine blades made from UD fibres and epoxy resin (Amoo, 2012).

2.2.5 Manufacturing techniques

F&S took into consideration the surface finish of the blade, consistent finished product tolerances and confidence in all plies being consolidated as the main requirements when manufacturing the blades. From their experience, resin transfer moulding (RTM) meets all the requirements (Fagerberg & Stromberg, 2007).

RTM is a technique of closed mould curing. Dry fibres are placed into a closed mould when a low viscosity resin is injected and typically cured with hot water running through the mould. F.L Matthews and R.D Rawlings describe the technique as a consistent and reliable way of ensuring consolidation between plies of complex geometry parts (Mattews & Rawlings, 1994).

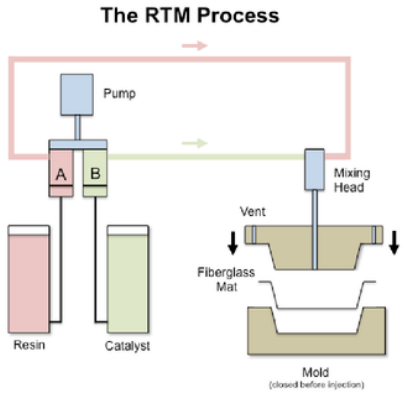


Figure 11 RTM process (Mattews & Rawlings, 1994)

Amoo states that most jet engine blades are manufactured using prepregnanted composites and are cured in autoclaves (Amoo, 2012).

2.3 FEA & Composite Material Principles

Once F&S established the design features and targets of the blade FEA and optimisation techniques were used to develop the laminate and stainless steel foot. Papers by Amoo and Lee also used FEA packages to develop jet engine blade laminate structures (Amoo, 2012) (Lee, 2008).

From the different sources researched (such as F&S and Amoo) it was evident that the ideal way of developing the blade laminate structure was to use FEA and optimisation packages, as this saves a vast amount of time when trying to achieve all blade design targets.

2.3.1 Design studio optimisation

Once a single FEA analysis has been completed within *Design Studio*, optimisation can be used to speed up the development process of the laminate. The optimisation principal is setting out the variables, objectives and constraints to find the best design for a given part through gradient-based algorithm. An example of this being applied to the fan blade is:

Variables – Number of UD plies
Constraints – 1: Does not deflect more than 10mm 2: Has a minimum natural frequency of 40Hz
Objectives – minimise blade weight

Once the 3 parts have been established, this creates a design dilemma. The optimisation provides an approximate solution to the problem. The optimisation problem is then carried out using DOT and BIGDOT optimisers within *Design Studio*. With it being an iterative process, once the optimisers have found an approximate solution, a new FEA is performed and the process is repeated until the solution converges. Numerical optimisation in a general sense solves the nonlinear and constrained problem, hence the set of design variables X_i, $i = 1, N$ contained in vector X, this will give:

$$Minimize\ F(X)$$

Topology within *Design Studio* can then be used to further develop the design and optimise part shape (Vanderplaats, 2007).

3. OUTCOMES FROM LITERATURE REVIEW

From reviewing the available literature, the scheme of work to design the blade was as follows:

Table 1 scheme of work

No.	Task	Description/Notes
1	Create CAD model of the current blade	
2	Calculate blade loading and distribution	The methods developed in the literature review are used to calculate both the aerodynamic and centrifugal loadings
3	Design testing rig	The loadings found from the calculations are used to design a whiffletree stiffness testing rig
4	Stiffness testing	Carry out the testing to find the current blade stiffness
5	Tap testing	Using a combination of using LDV and a single accelerometer testing rig to find the current blade modes
6	Mass testing	Measure the current blade to find the total mass and the centre of gravity
7	Develop FEA model	Develop the methodology of how to model the blade
8	Develop blade design	
9	Develop blade laminate	

The first step was to create a CAD model of the current blade from a 3D scan. *Mercedes* loaned their *CreaForm MetraScan* (see Figure 12) equipment to be able to create a detail scan of the blade.



Figure 12 CreaForm MetraScan equipment (CreaForm, 2019)

Figure 13 illustrates the scan data of the blade converted into the blade CAD used for this project.

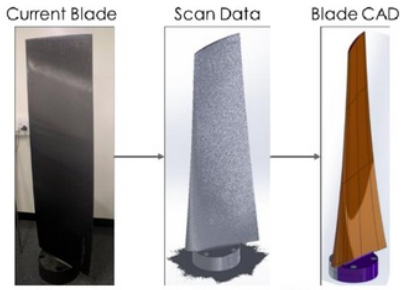


Figure 13 scan data into blade CAD model

4. INITIAL LOADING CALCULATIONS, RESULTS & TESTING RIG DESIGN

4.1 Blade Aerodynamic Load & Distribution

4.1.1 Wind tunnel information from Mercedes

Mercedes supplied the base information regarding the maximum tunnel load for the calculations discussed in Section 2.2.2 (see Table 2).

Table 2 base wind tunnel information (Miller, 2018)

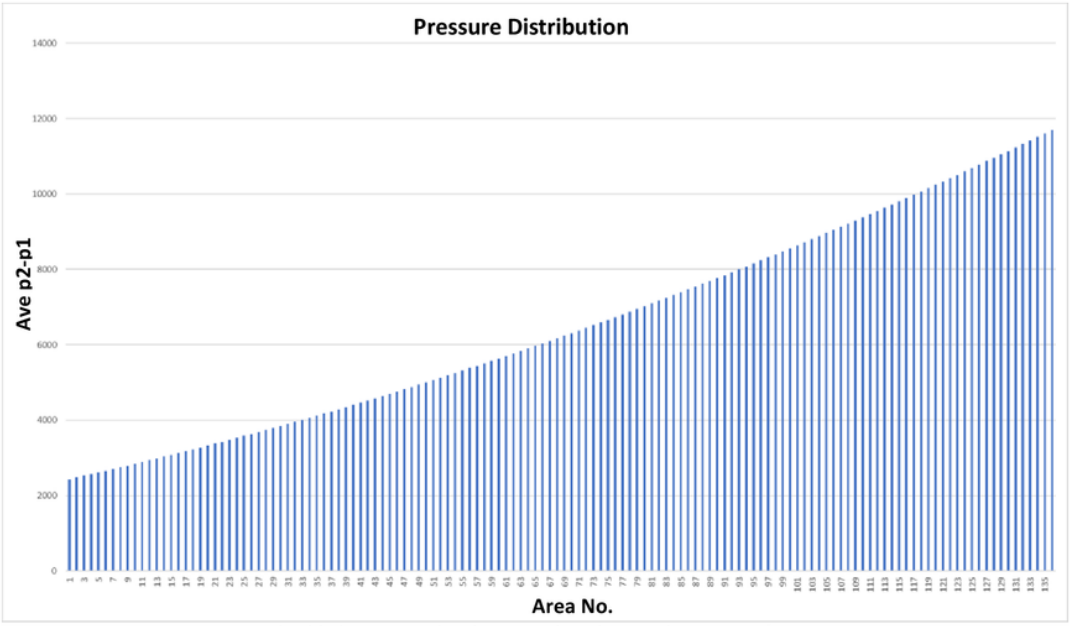
Calculation Input	Term	Value
ω	Fan rotor max RPM	550RPM
r	Radius of the blade from the rotation axis	1.2m
Va	The axial velocity inlet	55m/s
ρ	Air density	1.225Kg/m³

At 550RPM, the wind speed in the working section of the wind tunnel is 80m/s which decelerates to 55m/s when it reaches the inlet of the fan rotor. It is unclear what the outlet velocity of the fan rotor is as there is no air speed sensor until the working section of the wind tunnel. This means the velocity output speed could be between 55m/s to 80m/s.

4.1.2 Bending load distribution

The calculations were carried out in Excel and done in 10.625mm increments of the blade span, thus giving 136 calculations. The Excel spreadsheet can be seen in **Appendix J**.

Setting the outlet velocity to 80m/s in the calculations gives the following pressure distribution along the blade with area 1 being the start of the blade span and area 136 at the tip (see Graph 1).



Graph 1 blade pressure distribution with outlet speed set to 80m/s

It can be seen from Graph 1 that there is a trend of the pressure difference increases moving towards the blade tip. This makes sense when considering the blade tip is traveling at a higher velocity as the blade is rotating around the central axis. This trend underpins confidence that the calculations are consistent with expectation.

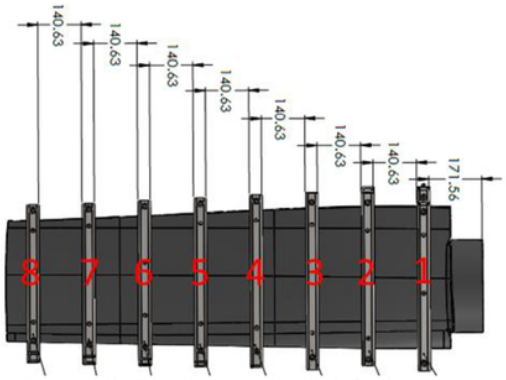
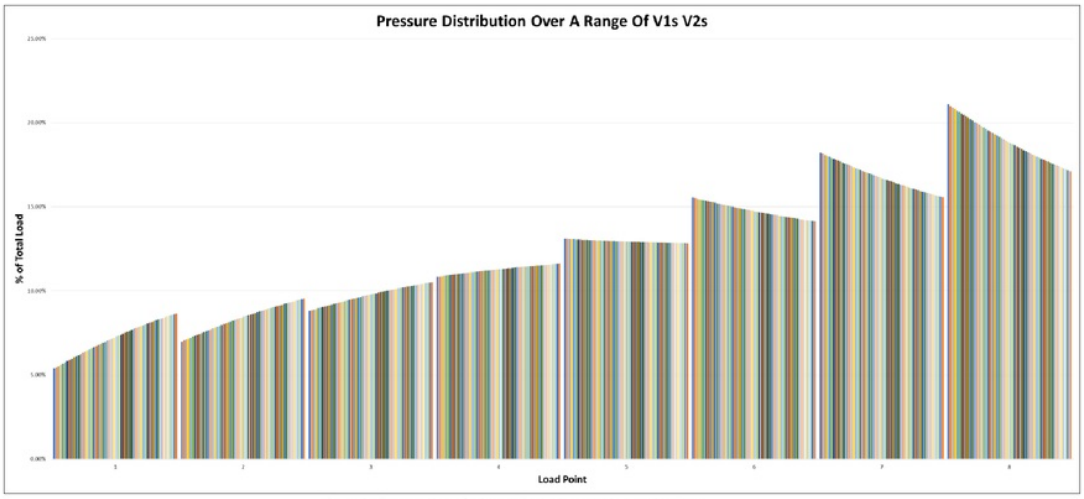


Figure 14 the 8 load points on the blade for the testing

The whiffletree principle design will apply the adopted load to the blade under tension through profile clamps (clamps see Figure 15). It was considered that 136 sections is excessive to accommodate along the blade span without over constraining the test. After researching what the minimum size of steel box section that could be used for the testing load, it was decided 8 load points would be the maximum. The 136 sections would be split into 8 loading points (see Figure 14 for CAD illustration).

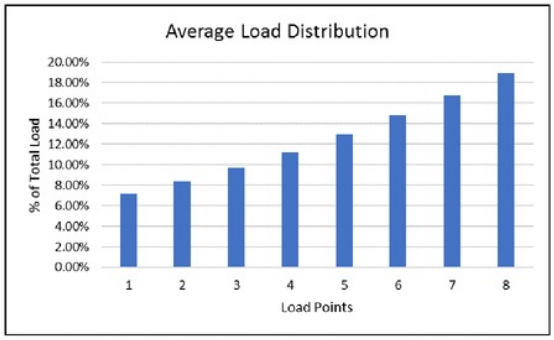


Figure 15 testing rig blade profile clamp



Graph 2 results of changing the outlet velocity

To understand how changing the outlet velocity changes the load distribution, the calculations were repeated 55 times. Graph 2 above shows the results of changing the outlet velocity values. The biggest change from 55m/s to 110m/s was 4.98%. This is a small enough change confirming the method can still be used. From Graph 2, the average was taken for each load point and used as the final load distribution (see Graph 3).



Graph 3 load distribution along the span of the blade

After adopting the average results, the trend remained the same with the largest load towards the tip. Comparing the results against F&S's CFD pressure contour, there is the trend of higher pressure towards the tip (see Figure 16's progressive green towards the tip).

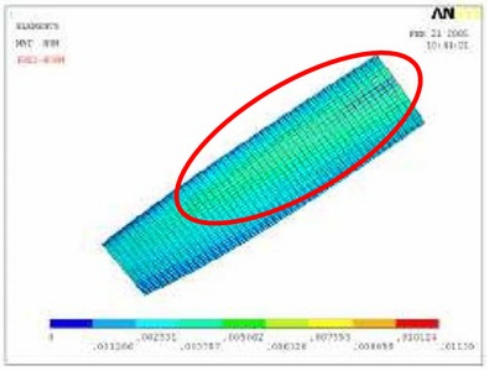


Figure 16 F&S CFD pressure distribution results (Fagerberg & Stromberg, 2007)

Whilst the two sets of results appear to match closely, there are still errors within the calculations. For instance, back in Section 2.2.1, Lee and F&S found the blades are aerodynamically designed to evenly distribute the aero load across the span as much as possible to achieve a target uniformly distributed load, particularly bending, maintained even longitudinally (Lee, 2008) (Fagerberg & Stromberg, 2007). The results did not reflect that trend. This could be down to the calculations not taking into account the varying coefficient of lift due to the blade twisting profile (different angle of attack along the blade). However, the results are sufficient enough to give an understanding of load distribution for testing to find the current blade stiffness. Table 3 is the percentage of total load going to each profile clamp for the testing rig.

Table 3 profile clamp load

Profile Clamp	% Of Total Load
1	7.17%
2	8.38%
3	9.74%
4	11.27%
5	12.95%
6	14.78%
7	16.78%
8	18.93%

Calculating the force acting on blade from coefficient of pressure at 550RPM results in **421Kg** as the maximum aerodynamic load at that speed. However, it should be noted this is just a guide for the total load as it is calculated from the frontal area of blade. The stiffness testing should be tested above this load to give a reserve factor for the calculations.

4.1.3 Torsional distribution

The torsional distribution comes from the point where the centre of pressure (CoP) acts along the chord length. For each of the load points on the blade, a 2D sketch of the profile shape (Figure 17) was taken and then exported into *Aero Foil Engineering* 2D CFD package for analysis.

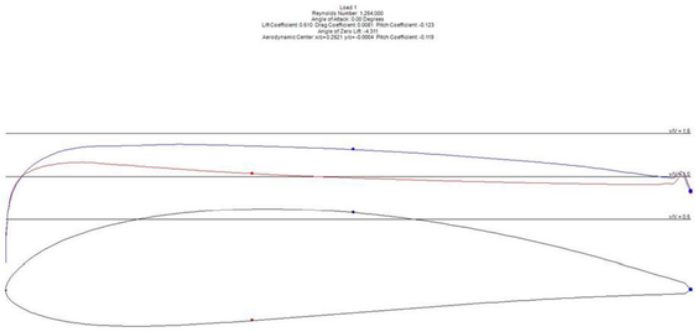
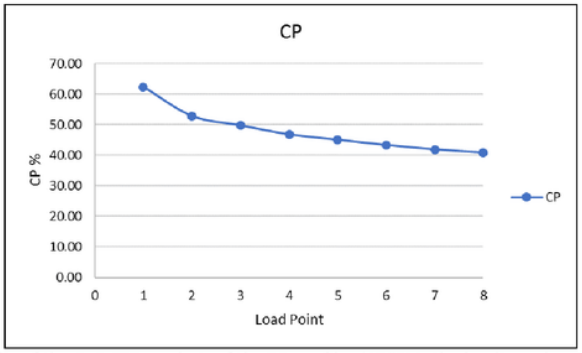


Figure 17 2D sketch of one of the profile shapes

For all the profiles, the air speed was set to a standard value for the analysis. One of the limitations of using this method was identifying what angle of attack the profile should be to find the CoP point along the chord which is closely represented in operation. To overcome this problem, each 2D profile angle of attack was adjusted in the software to give the same output coefficient of lift as it was the blade design methodology, to ensure an even load distribution (have similar lift force). This is a limited approach, but it keeps the torsional distribution relative to each other and gives an indication for testing. The results of this gave a percentage distance from the leading edge to the point of the CoP (see Graph 4).



Graph 4 results of the CoP CFD analysis of the 2D profiles (100% is the leading edge of the profiles)

The results show the profile nearest the blade base has the CoP point closer to the lead edge and travels towards the centre along the span length. This trend makes sense as the profile nearest the base is traveling at a lower air speed in operation meaning it needs to run at a higher angle of attack to achieve similar lift force in comparison to the profiles traveling

faster (keeping the bending load as even as possible). The trend can be seen in F&S's pressure contour data in Figure 16.

Table 4 below is showing the point at which the loads need to be applied along the chord lengths to represent the torsional distribution during the testing.

Table 4 torsional distribution points

Load Point	Chord Load Position
1	296.04
2	245.48
3	226.42
4	208.09
5	195.55
6	183.72
7	173.71
8	166.07

4.2 Stiffness Rig Design

4.2.1 Whiffletree design

The whiffletree distributes the force depending on the distance between the pin joint linkages. The tree was fabricated in a series of box sections with linkages to be able to take a single load input and split it into 8 points. The distance between the linkages dictates the percentage of the total load applied to a single load point (see Figure 18 for illustration) (NASA, 2011).

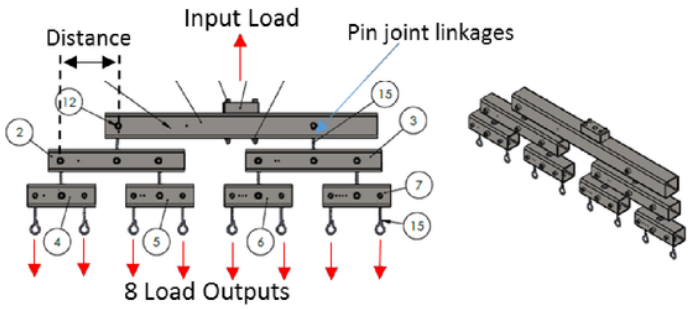


Figure 18 the whiffletree construction

The box section size was designed to have a large safety factor to minimise the deflation of the parts when under load and affecting the testing results.

To calculate the correct distance between the linkages for the correct force, distribution moments were used. The construction of the excel spreadsheet to calculate the required pin to pin distance to match the results of Section 4.1.2 can be seen in **Appendix J**.

To apply the torsional distribution as well as the bending load, the whiffletree was configured to apply force offset along the profile clamps to represent the results of Section 4.1.3 (see Figure 19).

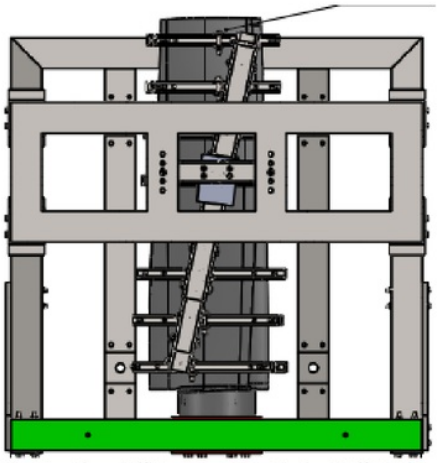


Figure 19 showing the whiffletree applying the load offset along the blade

4.2.2 Overall scheme

The stiffness rig works by applying the load through a chain host and is monitored by a tensile load cell (see Figure 20).

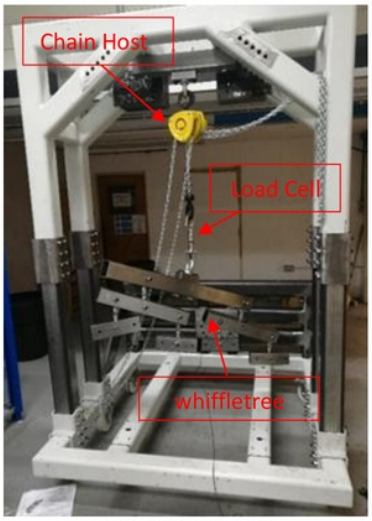


Figure 20 stiffness rig

Due to the twisting of the blade profile, determining what angle the load should be applied was a challenge. In operation the aerodynamic loading is applied normal to the surfaces of the blade profile, but the rig could not apply the load in this manner. If the blade was mounted in the rig with the start of the span perpendicular to the loading direction, then towards the end of the span, the load would need to be applied 45° (see Figure 21).

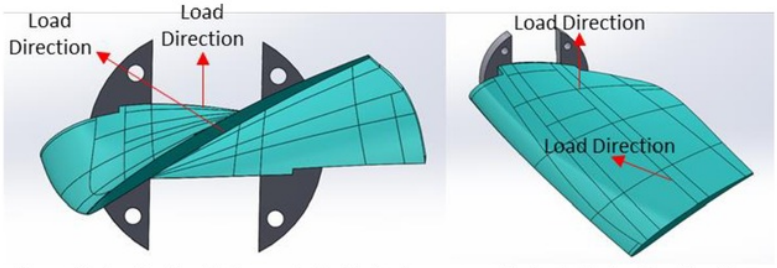


Figure 21 showing the blade mounted with the base perpendicular to the loading direction

If the blade was mounted twisted at the base so the end of the span was perpendicular to the load direction, the same problem would occur at the reverse end (see Figure 22).

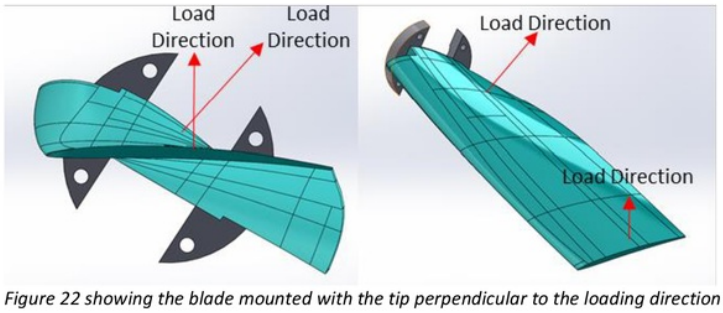


Figure 22 showing the blade mounted with the tip perpendicular to the loading direction

To achieve a compromise, the blade is mounted 17° offset to minimise the twisting (see Figure 23). This is one of the limitations of the stiffness testing rig as it is not applying the load that truly resembles actual operating conditions. This is a disadvantage of adopting stiffness testing instead of CFD.

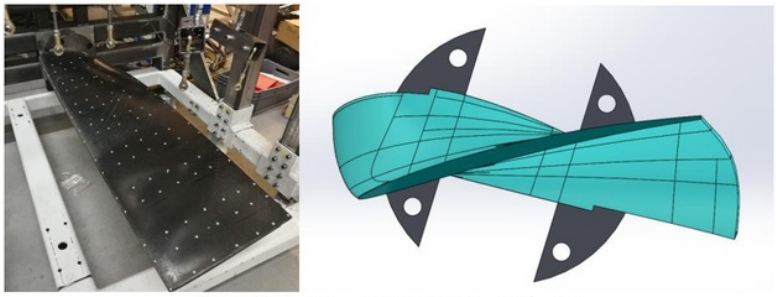


Figure 23 blade mounted on the rig at 17° offset

The load cell tracks the load being applied to the blade and displacement is tracked by the GOM camera tracking system.



Figure 24 GOM camera tracking system

5. TESTING RESULTS

This section lists the results of all the blade testing carried out. **Appendix B** details the methodology of how the tests were carried out.

5.1 Initial Testing Results

Whilst waiting for the manufacture of the main testing rig, a simplified alternative point load facility was built to allow initial performance data to be captured so that the first stage design development process could proceed pending completion of the whiffletree rig.

Figure 25 is the design of this initial testing rig. The rig applies the bending and torsional load separately through a profile clamp at the end and the blade is attached to a steel girder to minimise the deflation of the base influencing the results.

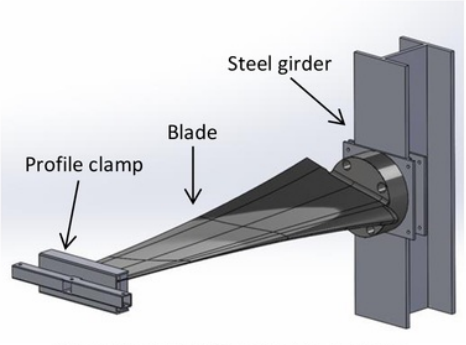


Figure 25 initial 'stiffness testing rig' design

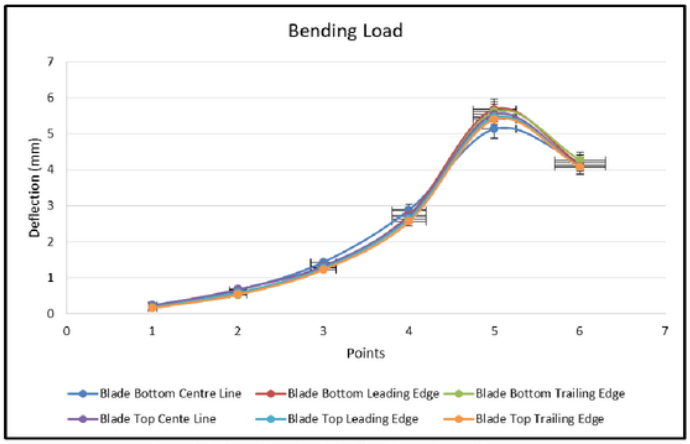
The blade was tested up to 50Kg in bending and 12Kg in torsional. The load was applied in increments to ascertain if the deflection is linear and thus the stiffness is linear. The deflection was measured using 6 DTi's along the span. The test was repeated with the DTi's in different positions on the upper and lower surfaces to identify if the current blade laminate was consistent everywhere.



Figure 26 the current blade being tested with the DTi's

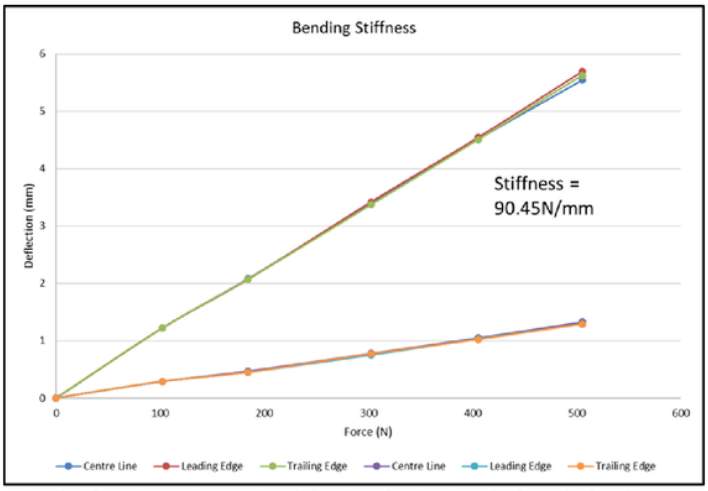
5.1.1 Bending load testing results

The construction of this testing rig and how it applies the load creates a cantilever beam scenario. The lines in Graph 5 represent the deflection of the blade with DTi's in different positions. The results show that the blade bends consistently across the whole span and chord lengths indicating the current layup is symmetrical. However, point 6 shows the deflection decreases which deviates from what could be expected from bending of this type of beam. Initially it was thought that this could be due to a faulty DTi, but changing the gauge had no effect on the result. It was hopeful that the whiffletree testing would shed more light on this anomaly in the blade deflection.



Graph 5 bending load deflection along the span

Graph 6 maps out the stiffness of the blade. The two set of lines are showing how the deflection is increasing as the load increases at points 3 and 5 from the test. Both sets of lines are linear across the blade meaning the blade material is working in the elastic region. For both points the stiffness is 90.45N/mm.



Graph 6 force increasing against deflection of points 3 and 5 from the bending test

5.1.2 Torsional load testing results

To represent the torsional behaviour, the blade loading needed to be offset from the centre axis to create a twist in the blade. Also, due to the nature of the blade profile, a load at each of end of the profile clamp was required to be in the same clockwise direction (Figure 27 illustrates torsional load). However, the equipment needed to create this loading scenario for the testing rig was unavailable. Instead, a compromise was to load separately the leading and trailing edge of the blade offset from the centre (see Figure 28). This does not create a pure torsional load, but a mixture of bending and torsional which would have to suffice for this testing rig.

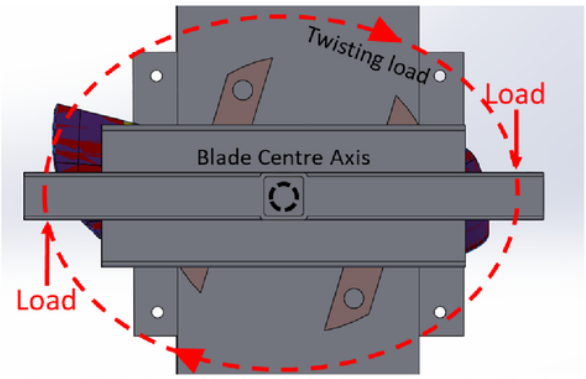


Figure 27 ideal way of loading the blade to create torsional load

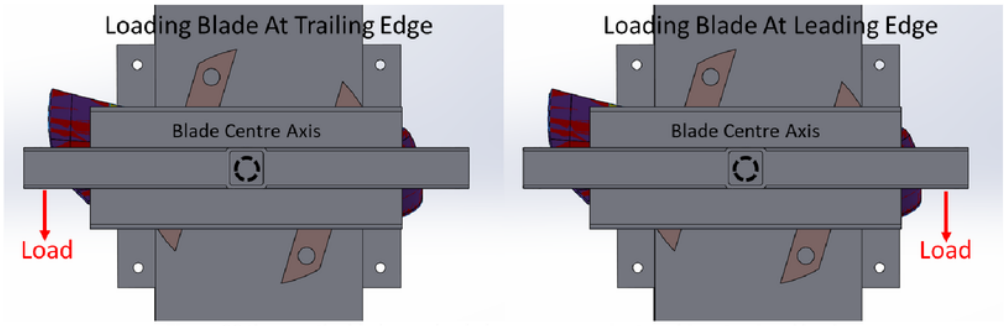
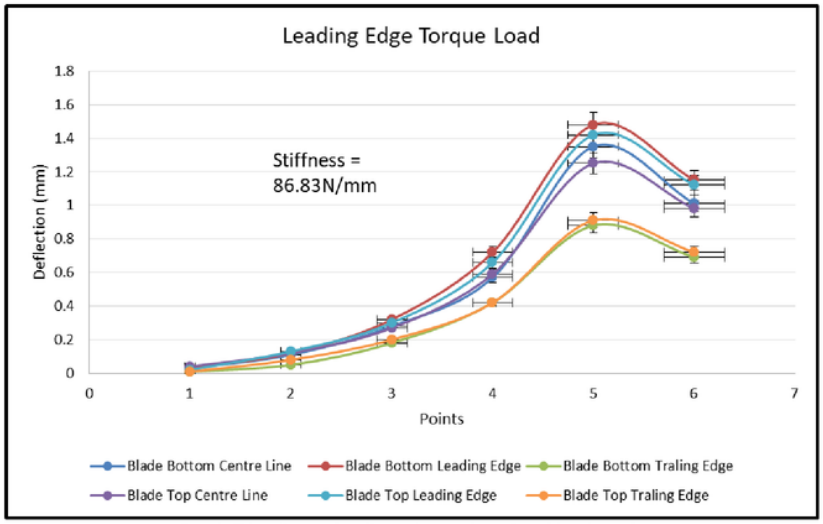


Figure 28 the way the blade was loaded as a compromise to achieve torsional load

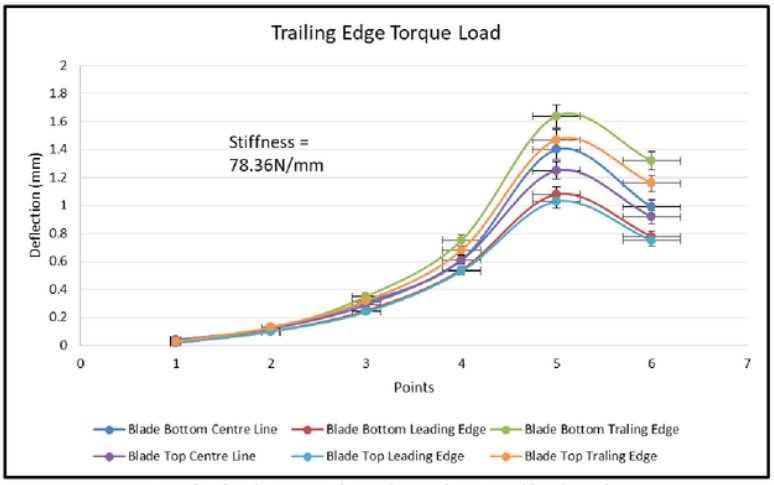
Graph's 7 and 8 are the results from applying the load at either end of the profile clamp. The same testing method of repeating the test with the DTi's in different positions was carried out. Between both sets of results, the DTi's switch with the amount of deflection measured at the trailing and leading edge blade surfaces (observe the coloured lines change over magnitude in Graph's 7 and 8). This does indicate that the test is applying some torsional load to the blade as it would be expected to see the lines closer together if the blade were bending more than torsional. The testing for torsional load is not perfect with this rig design but is sufficient for having starting data to advance the design process pending the manufacture of the whiffletree rig.



Graph 7 loading at leading edge and torsional load results

The graph lines switching between the two tests points towards there being a symmetrical layup for the torsional stiffness of the blade. The leading edge results in a stiffness of 86.83N/mm and trailing of 78.36N/mm, both which are close to the bending stiffness of 90N/mm. This again indicates symmetrical layup across the whole blade. Alternatively, it

could be due to not being a pure torsional load and the plies creating the bending stiffness are contributing to the results.



Graph 8 loading at trailing edge and torsional load results

Overall, the results from these tests are not perfect but considered sufficient for moving the project forward. The DTi data from the tests can be used as constraints for optimising the new blade layup for the given load to match the stiffness performance. However point 6 previously discussed seems to be an error in the data and consequently only the data up to point 5 was used for optimisation of a new layup.

5.2 Whiffletree Testing Results

The original idea with the whiffletree rig was to set the GOM system facing to the side of the blade looking down to capture the full length of the blade deflecting under load as illustrated in Figure 29. However, an oversight when designing the testing rig was the GOM system cameras could not be positioned to pick up the points on the blade due to the steel pillars supporting the rig being in the way (see Figure 30).

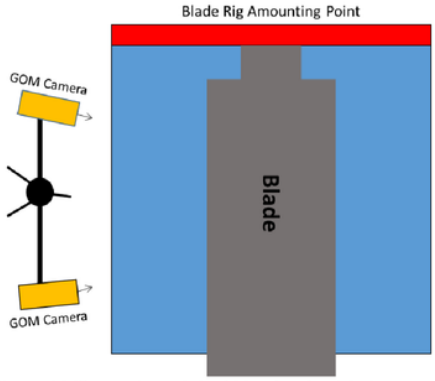


Figure 29 illustrating original idea for the GOM system

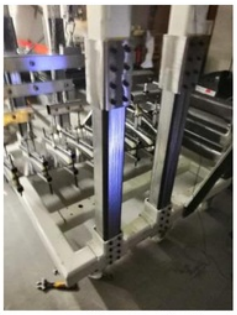


Figure 30 steel pillars supporting the rig obscuring GOM cameras

The compromise was to position the cameras offset from the blade front looking along the side (see Figure 31).

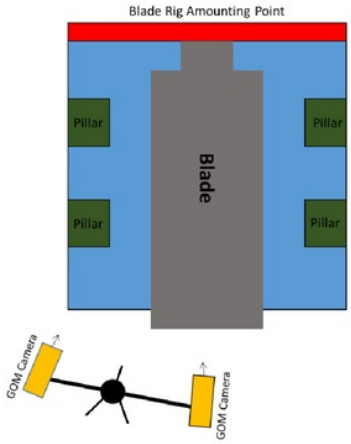


Figure 31 compromise position for the GOM cameras

5.2.1 Potential errors

Figure 33 illustrates how the position of the cameras during the test could not capture the entire length of the blade and could only pick up the points on the profiles clamps 4 to 8. This meant when designing the new blade this is the only data available to match the stiffness performance. However, there are a few potential errors using this data:

- The profile clamps do not move fully relative to the blade surface as the parts have their own displacement and stiffness properties which would mean the blade is not deflecting as much as is shown from the data.
- Not having the full length of the blade measurements could lead to not matching the correct stiffness performance.

In Figure 33, where the profile clamp is at the tip of the blade, the GOM system is picking up the points on the top box section, blade surface and bottom box section. To identify how

much of a difference between the blade moves relative to the profile clamp, the point captured on the end of profile 8 can be analysed. This is achieved by calculating the percentage difference between points on the top box, lower box and blade surface. The calculation was done on 5 sets of three points that align to each other across the chord length at profile 8 (see Figure 32).

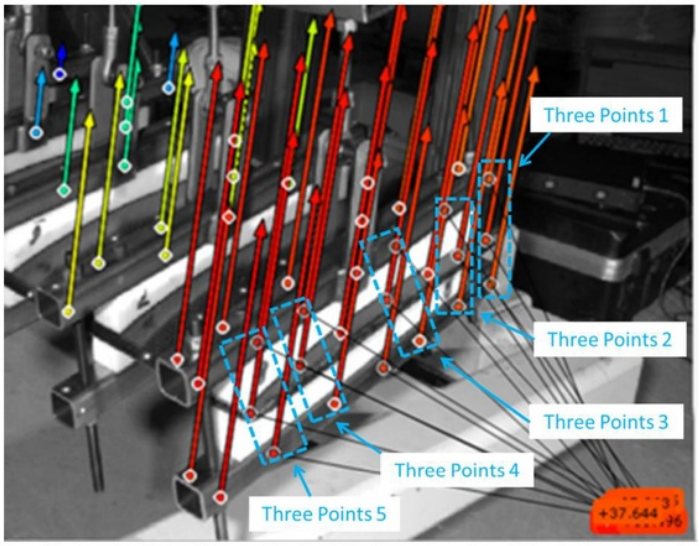
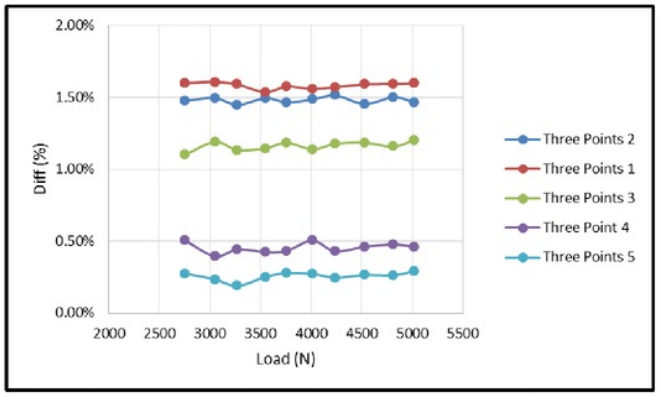


Figure 32 showing the points used to check blade movements relative to the profile clamp

Graph 9 shows the results of comparing the displacement between the 5 sets of three points as the load increases. The minimum difference is below 2%, rendering it negligible. The difference was likely to be even smaller as the FEA should model the problem correctly. Also, profile 8 shows the maximum difference as it is applying the most load.



Graph 9 results of comparing the displacement between the 5 sets of data

Figure 33 also shows at the mid-point of the blade span (profile 4), the deflection is converging to minor and with the blade bending like a beam it is reasonably predicted to reduce further closer to the base. With the deflection being very small after profile 4, the data

that might have been captured would likely have very minor influence on defining the stiffness of the new blade. Under these circumstances, the data is considered sufficient enough to develop the layup to give the correct stiffness on the new blade.

5.2.2 Results

The blade was tested up to 5020.4N (511.76Kg). Figure 33 is the magnitude of blade displacement at 5020.4N load that the GOM system measured.

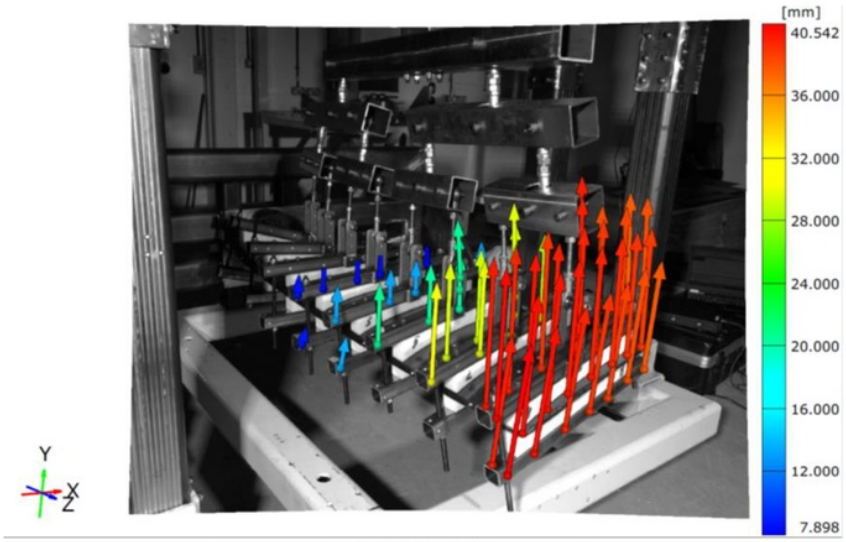


Figure 33 magnitude of blade displacement at 5020.4N

The GOM system can divide up the magnitude displacement into X,Y,Z components with Y being the bending deflection. Figure 34 is the Y component from the test which shows progressing towards the tip of the blade, the deflection is increasing exponentially. This indicates that the load towards the tip is potentially increasing, which was expected from the whiffletree design in mimicking the load distribution from the calculations in Section 4.1. However, it could just be displacement characteristics of a cantilever beam scenario in bending. There is, in actual fact, no way of establishing if the load being applied from the whiffletree is delivering what was expected.

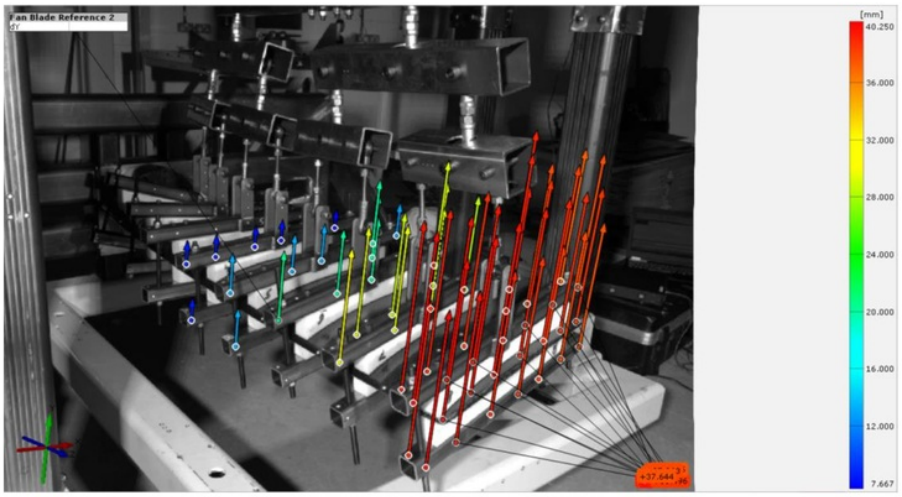
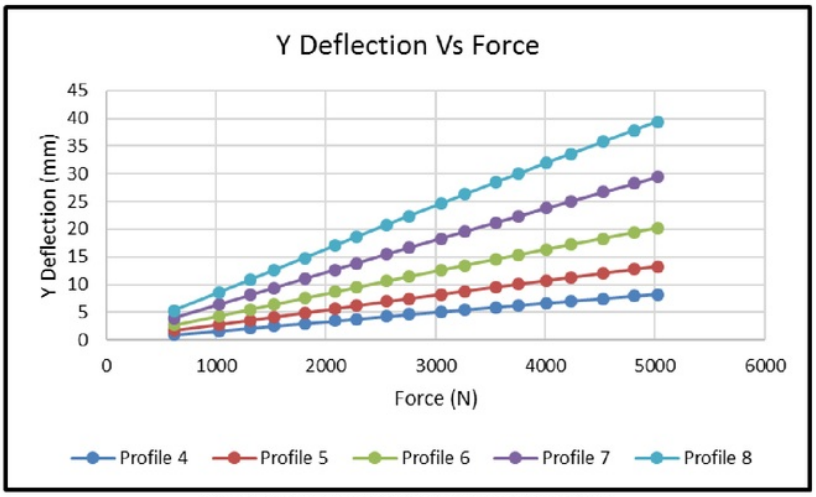


Figure 34 Y component from the test

There is confidence in the whiffletree loading, the results of which are shown in Graph 10 which is mapping out each profile clamp displacement against load. From zero load, all clamps are the same but as the load input increases, the gap between the graph lines is increasing in accordance to what was expected. Profiles 4, 5 and 6 have similar jumps between the displacements as do the calculated load distribution. Profiles 7 and 8 are increasing with the gap greater in comparison, which also aligns with increasing load distribution.



Graph 10 Y component displacement against load

The calculations for the torsional loading of the whiffletree found approaching the centre of the blade span (profile clamp 4) moment of the load is centre of the chord and towards the tip moves off to the side. Looking at the X component (see Figure 35), there is deflection off to one side of the blade towards the tip and minimal at the span centre, which matches to

what was expected of the whiffletree loading. This indicates the rig is applying the right load distribution.

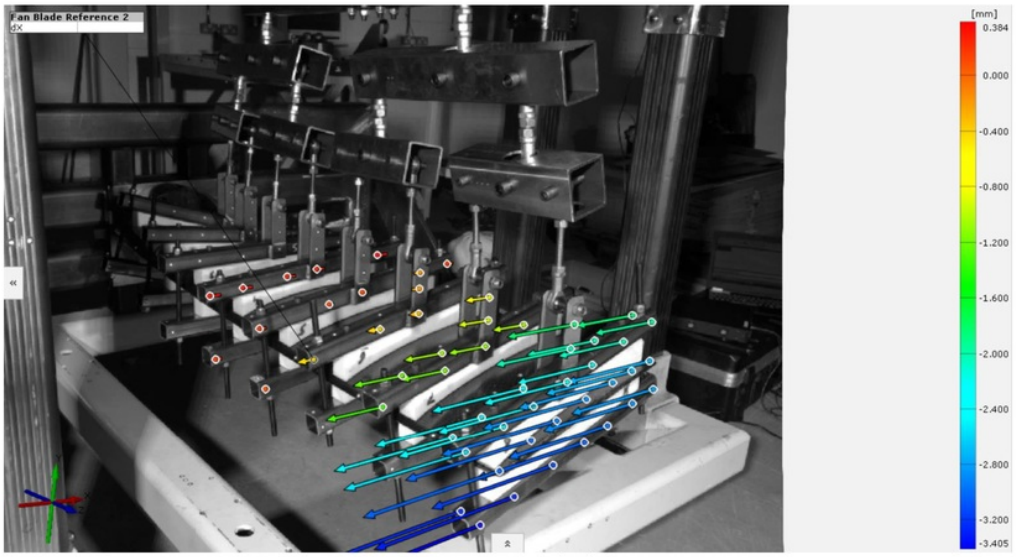
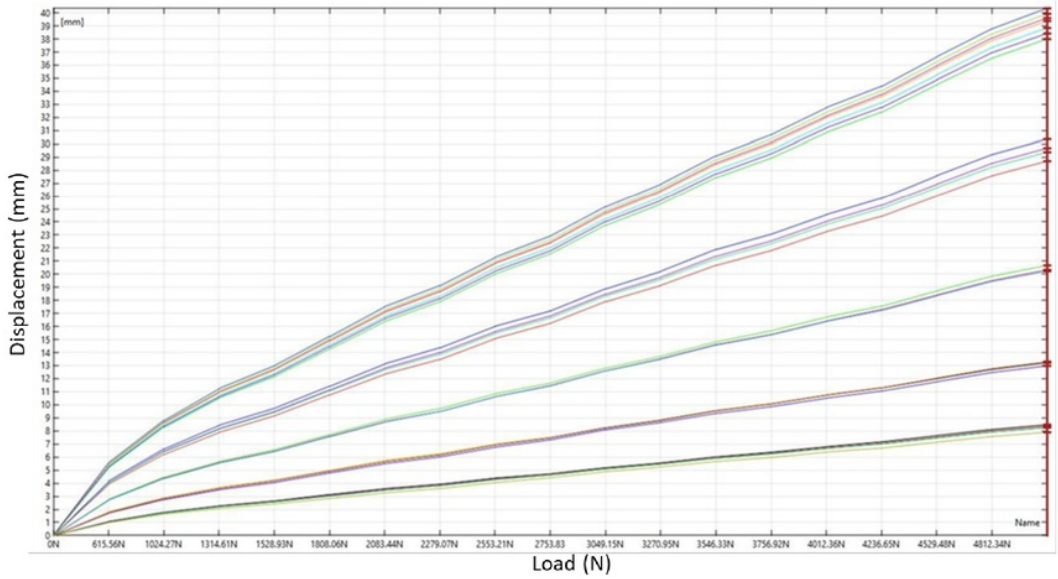


Figure 35 X component displacement

Graph 11 is showing how the magnitude displacement from the measured points on the profile clamps increases with load. The graph lines are all linear indicating the blade is still working in its material elastic region. However, at a low load input, the graph traces are not linear but this is due to the whiffletree taking up slack and not applying load across the whole blade.



Graph 11 all the points' magnitude displacement against load

All of the results from this testing did not replicate the errors identified in the initial testing results from the temporary rig (see Section 5.1.1). There is the possibility that the profile clamps are constraining the blade during testing which would hide this error, but that is unlikely as the profile clamps were positioned away from point 6 that was measured in the initial testing.

The results of the testing was considered adequate for defining the stiffness of the new blade. Table 5 shows the magnitude displacement data to be used as constraints for optimising the new blade layup for the given load to match the stiffness performance.

Table 5 magnitude displacement data to be used as constraints

Profile	7	6	5	4	3	2	1
4	8.479	8.372	8.267	8.253	8.17047	7.898	7.81902
5	13.247	13.23375	13.226	13.1731	13.1204	13.06792	12.983
6	20.667	20.46033	20.327	20.225	20.02275	19.82252	19.6243
7	30	29.73	29.678	29.373	29.07927	28.69	28.4031
8	40.346	39.923	39.601	39.378	38.843	38.42	37.993

5.3 Blade Frequencies Testing Results

5.3.1 Tap testing results

Figure 36 below shows the results of the tap testing to find the first natural frequency.

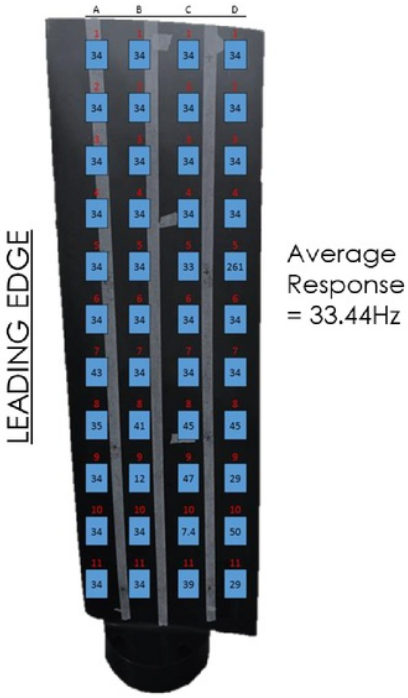


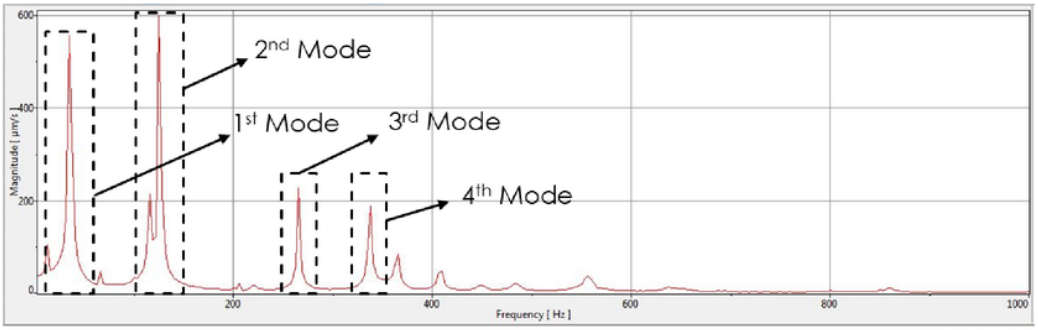
Figure 36 tap testing results

The 44 accelerometers found an average response of 33.44Hz across the blade. This average ignores a few accelerometers that were outputting erroneous results that did not follow the trend of the majority on the blade.

The result of 33.44Hz was encouraging as this was very close to what F&S designed and tested (Fagerberg & Stromberg, 2007). The actual difference between the results could be due to the setup of the test; for example F&S tested a blade bolted to a steel plate while this current blade was bolted to a steel table. To what torque the bolts are tightened will have an effect on the stiffness of the blade and its frequency. Attached to different platforms also has an effect on the frequency (Agilent Technologies, 2000) (Fagerberg & Stromberg, 2007).

5.3.2 LDV results

The LDV also found the same first frequency of 34.37Hz confirming correlation of the two test methods underpinning confidence in the results. The LDV's magnitude frequency graph of all 4 modes are shown where the data trace spikes (see Graph 12).



Graph 12 LDV magnitude frequency results

From the results the LDV found the mode shapes of all 4 modes. The first mode is bending. Figure 37 shows the results compared to F&S's FEA results. LDV correlates closely. F&S in their report only state the frequency of the first mode to be 38Hz, but does show the other 3 modes shaping FEA results.

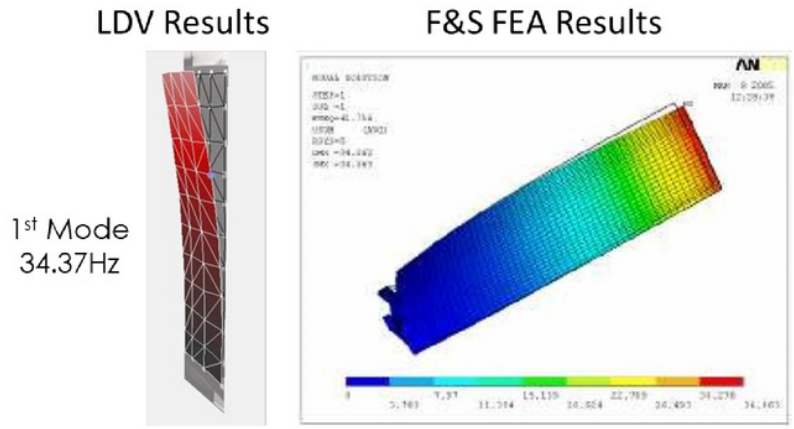


Figure 37 LDV and F&S results of the first mode shape (Fagerberg & Stromberg, 2007)

The second mode shape is torsional and again correlates to F&S's findings (see Figure 38).

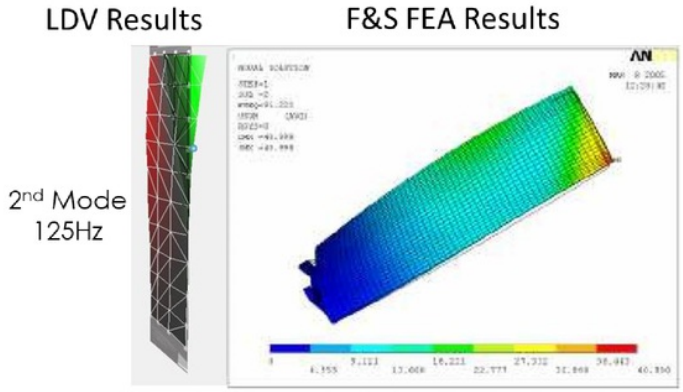


Figure 38 LDV and F&S results of the second mode shape (Fagerberg & Stromberg, 2007)

The third mode shape is second torsional which also correlates (see Figure 39).

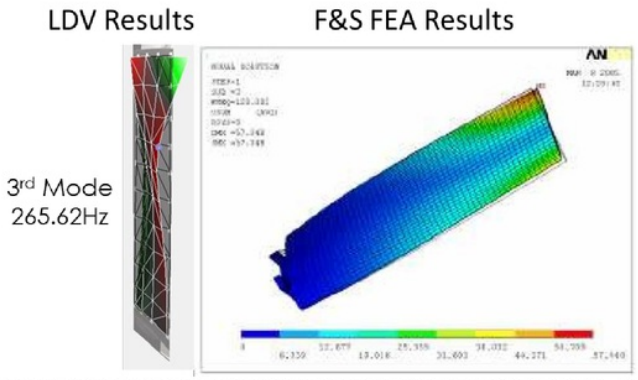


Figure 39 LDV and F&S results of the third mode shape (Fagerberg & Stromberg, 2007)

And finally the fourth mode is second bending (see Figure 40).

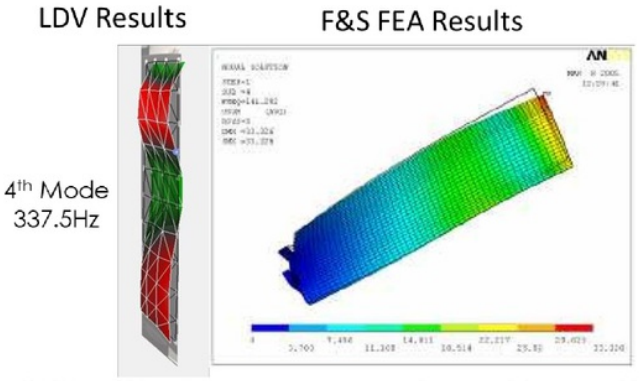


Figure 40 LDV and F&S results of the forth mode shape (Fagerberg & Stromberg, 2007)

All the results correlate to F&S's findings which implies:

1. Full confidence in the testing results.
2. The blade designed in F&S's report is the same blade being reverse engineered in this report.

The results from the LDV testing was adopted for the design input for the new replica blade.

5.4 Existing Blade Mass Testing Results

Another important aspect of the blade to be determined was the total mass and the CoG point.

5.4.1 Blade total weight

The current mass of the total blade was measured (using scales) to be 20.1Kg.

5.4.2 Blade centre of gravity measurement

The distance of the CoG point from the blade base (Z) influences the inertia and the centrifugal force of the blade.

To find the Z distance, a simple test of balancing the blade until in balance was carried out (see Figure 41).

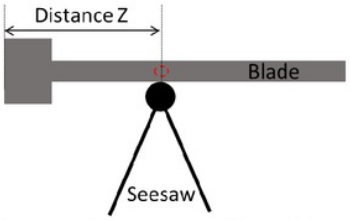


Figure 41 illustration of the seesaw used for find the CoG Z distance

The test established the Z distance for the current blade is 359mm.

6. REPLACEMENT BLADE DESIGN TARGETS

Table 6 below contains the design targets for the new replica blade which were formulated from research and the pre-design testing results:

Table 6 blade design targets

No.	Target	Value
1	New Design To Match Current Blade Stiffness	Match the values from testing
2	The Design To Cope With Centrifugal Loading At 550RPM	Value to be calculated
3	Total Blade Mass	20.1Kg
4	New Design To Match 1st Mode Frequency	Min 38Hz
5	New Design To Match 1st Mode Shape	Bending Mode
6	The CoG Z distance	Z To Be No More Than 359mm
7	Steel Foot Stress To Be Half Of Material Yield Point	Depending On Material
8	Composite Strain	Be Below 3000 Microstrain

Notes for Table 6:

- The ideal target is to match the exact displacement for the given load from the whiffletree testing results, but this might not be possible in the new design. How much of a % error that would be acceptable is not clear as there is no reliable literature to guide. With that in mind, the way forward was to achieve a blade design output and then discuss the values with the project partners, and in particular the implications of the error % that could be tolerated in accepting the final design output.
- The centrifugal loading was calculated from the formula detailed in Section 2.2.1 once a design matched the stiffness targets. The design coping with the load will be judged on the stress and strain of the blade design.
- The first frequency of the blade was the priority to achieve in view of how the new design would interact with the existing blades still in operation. The other 3 modes were considered of less importance as the rotor would not operate near the frequency values to cause a mode to interact with existing blades. However, if the other mode shapes can be achieved, then this would indicate the new blade is matching the exact required stiffness performance.
- The Z distance was set not to increase more than the current blade as this would increase the inertia load on the fan rotor without appreciating the implications on the structural integrity. The value can be lower provided the new blades are changed in pairs to avoid an imbalance during rotor operation.
- The stress on the steel foot needs to be half of the yield to avoid creep within that part. This follows the same approach as F&S (Fagerberg & Stromberg, 2007).

- As established in the literature review, one of the steel foot design concepts is to be able to neglect creep within the composite. Nolan Richmond from his experience advised the plies within the composite layup should not be above 3000 microstrain to certify the part to withstand an infinite life cycle negating the need for a fatigue analysis (Richmond, 2018).

6.1 Replica Blade Principal Design

At this point of the project, *Lentus* confirmed the unilateral decision to manufacture the new blade using prepregnated composite materials in view of the extensive experience of this technique within the organisation. In addition, the alternative of using an RTM process would be too expensive and outside the remit of the project costing.

The initial design of the replica blade followed the same principals as F&S did with the current blade.

The new blade design process was approached considering the following segmental parts:

1. Steel Foot – For the reasons explained in Section 2.2.5
2. Foam Core - For the reasons explained in Section 2.2.5
3. Central UD 0 Laminate - For the reasons explained in Section 2.2.5
4. Full Blade Laminate - For the reasons explained in Section 2.2.5
5. Steel Sleeves – To protect the foam core from damage when installing the blade into the rotor.
6. Shroud Foam Core – To form the shroud shape.
7. Shroud Composite Skin – To protect the shroud core and steel foot.

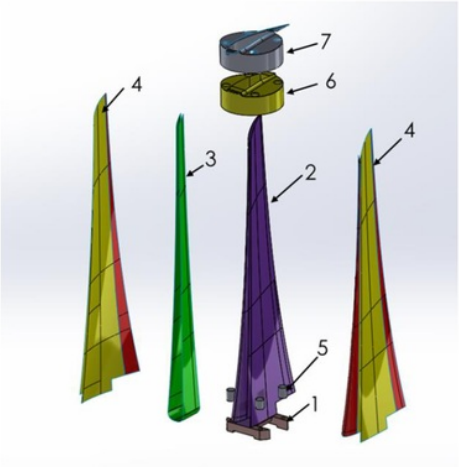


Figure 42 main parts forming the new blade design

7. FEA METHODOLOGY

The FEA model of the blade is one of the most important aspects of the project as it is defining the new design of the blade. Using the correct approach at modelling the blade is essential as model correlation can only come after a prototype has been made. This section runs through the methods found to best model the blade.

One of the blade design principals is to eliminate the need for fatigue analysis or non-linear analysis. This means all the FEA carried out on the blade will be done using linear analysis only.

7.1 Mesh Strategy

The following criteria were determined in pursuit of adopting the best approach to mesh the blade:

- Mesh type
- Mesh density
- Mesh configuration for each blade part and construction model

7.1.1 Blade assembly meshing categories

The blade comprises multiple parts (as detailed in Section 6.1) requiring different meshing techniques categorised as follows and contributing to overall blade design:

1. Parts that are composite (composite parts)
2. Parts which are considered to be in high stress (steel parts)
3. Parts for low bearing stress (sandwich parts)

In **Appendix C** the options for meshing the parts are discussed and reviewed. Having reviewed the options for meshing the blade, the following approach was adopted:

- The composite parts of the blade used 2D quads elements.
- The principal complex geometry is the inner sandwich. Using a bricks mesh was found to be extremely difficult. As an alternative, tets was adopted as the sandwich was not considered to be under high levels of stress.
- The steel parts used bricks elements where feasible with an option to revert to second order tets if subsequent foot design evolves into complex geometry. It has already been established the difference in outputs is small.

There are a few methods to connect meshing multiple parts.

7.1.2 Mesh connection methods

There are a few ways of modelling the connection between the different part meshes each with particular benefits and selection depending on the model scenario (Predictive Engineering, 2014). The methods are:

1. Concentric nodes
2. Spring elements
3. RB2 and RB3 elements
4. Glue contact regions

Each method was tested through parameter studies and coupon testing, with the results and analysis available in **Appendix D.**

In conclusion, the overall best method for connecting the meshes together within the blade model is using glue contacts with the settings used in run 8 (see Appendix D) as it has acceptable correlation between all fronts.

7.1.3 Mesh density

Mesh density is an impotent aspect of modelling in FEA (MacDonald, 2011). Unfortunately there is no straightforward answer to what is the right mesh size or density, but there are methods to help find the right mesh approach:

1. Compare FEA results to experimental testing data.
2. Run an initial analysis with a medium mesh density followed by a further run with a fine mesh and ascertain if there are big differences in the results.
3. Run with overly fine mesh throughout the model.

For the blade model, the following approach was adopted throughout the project:

- Run an initial analysis with a medium mesh density and run again with a fine mesh until the difference is small.
- Increase the mesh density where there is adverse colour contour transition.
- The steel foot had a fine mesh as this was considered an area of high stress.
- Fine mesh refinement around steel foot bolt holes.
- The sandwich part mesh could be low density in comparison to the foot to save on resolving time as this area was expected to be in low stress. This also applies to other areas where stress is low.

The above approach was developed from carrying out research and testing, see **Appendix E** for the results and discussions.

7.1.4 Other elements used in the model

The whiffletree testing applies the load through the profile clamps (see Figure 15). To match the same loading as the blade experiences during testing, the clamps are modelled into the FEA blade model (see Figure 43). This is important to help match the same stiffness when optimising the layup.

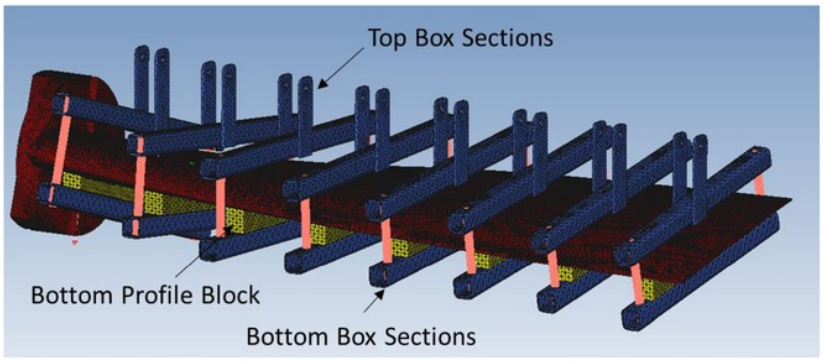


Figure 43 profile clamps modelled into the blade FEA model

Note in Figure 43 only the bottom profile block is modelled in. It was considered that only the bottom clamp was in contact with the blade during the test as the rig was pulling the blade upwards, meaning the top profile block disengages from the blade surface and thus is not in contact. The top profile block was removed to save on solving time.

To simplify the model further the bolts connecting the top and bottom profile box section were removed and replaced with spring elements. The spring elements stiffness was defined in the same manner as shown in Appendix D to match the bolts used in the rig. Table 7 is the data used to calculate the stiffness of each bolt used in the rig and Figure 44 is showing to which profile clamp the bolt value is referring to.

Table 7 data used to calculate the bolt stiffness's and stiffness results

Bolt	Working Length	Area	E	Stiffness	Units
1	210	84.3	205000	82292.85714	N/mm
2	195	84.3	205000	88623.07692	N/mm
3	195	84.3	205000	88623.07692	N/mm
4	180	84.3	205000	96008.33333	N/mm
5	170	84.3	205000	101655.8824	N/mm
6	170	84.3	205000	101655.8824	N/mm
7	160	84.3	205000	108009.375	N/mm
8	169.61	84.3	205000	101889.6291	N/mm
9	210	84.3	205000	82292.85714	N/mm
10	195	84.3	205000	88623.07692	N/mm
11	195	84.3	205000	88623.07692	N/mm
12	180	84.3	205000	96008.33333	N/mm
13	170	84.3	205000	101655.8824	N/mm
14	170	84.3	205000	101655.8824	N/mm
15	160	84.3	205000	108009.375	N/mm
16	169.61	84.3	205000	101889.6291	N/mm

The working length was measured from the blade testing CAD model, the area is the bolt thread cross-section of an M12, and *E* is from the bolt material datasheet.

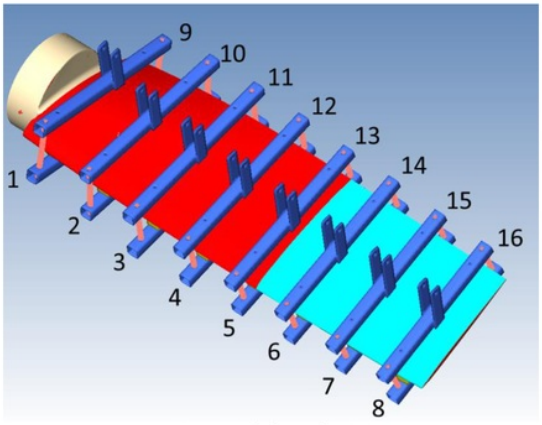


Figure 44 bolt numbering

7.2 Model Loading

When designing the blade, there were initially 3 separate FEA models to load the blade under 3 load types.

1. Applying load from testing
2. Applying the centrifugal load
3. Applying both loads at the same time

Applying the load obtained from the stiffness testing had to be done separately as the rig did not apply centrifugal force to be able to match the stiffness. Once a design was matching the stiffness from testing, it could then apply both loads simultaneously. Applying the centrifugal load only was done just for the initial design process.

7.2.1 Applying the stiffness testing load

As explained in Section 7.1.4, the profile clamps in the FEA model are applying the load to the blade. Referring to the excel spreadsheet built to calculate the whiffletree load distribution, the max testing load of 5020.4N was entered to evaluate the loading for each profile clamp. Table 8 shows the loads applied to each clamp in the FEA model.

Table 8 loads applied to FEA model

Profile Clamp	Load (N)
1	436.48
2	493.54
3	562.29
4	632.92
5	711.76
6	800.07
7	895.08
8	1000.1

Figure 45 illustrates the location of the load points. Normally the load is applied through the bolts holes in the box sections during testing. However in the FEA model, they are applied to the nodes on the top surface of each box section to simplify the model since it does not make a difference to how it applied to the blade.

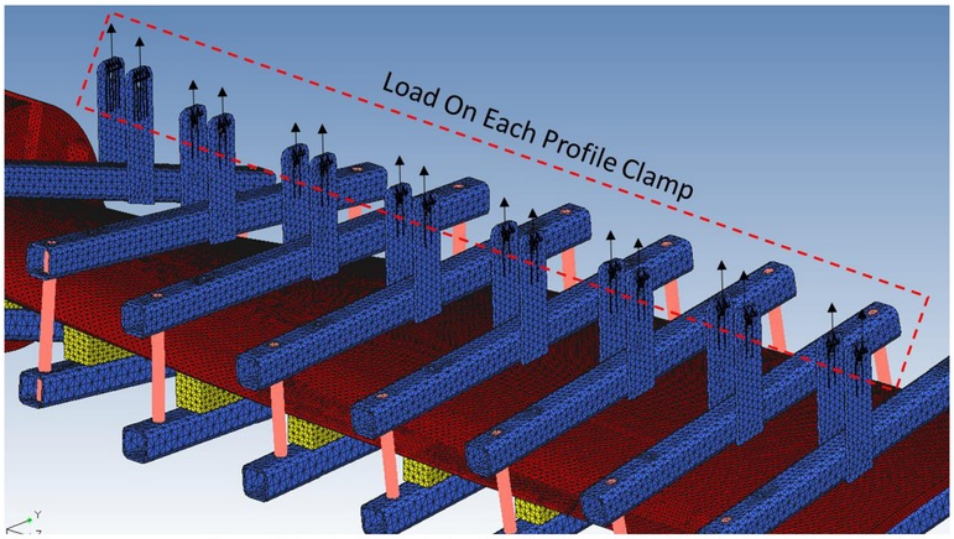


Figure 45 showing where the load was applied to the profile clamp

7.2.2 Applying the centrifugal load

The easiest way of applying the centrifugal load to the blade was applying a gravitational load to the model. The gravitational load (a) can be worked out from using $F = ma$ where F is the centrifugal force of the blade at 550RPM and m is the mass of the blade assembly. This way is advised by *Siemens's FEMAP* commands FEA guild and is similar to how F&S modelled the loading on the current blade (Siemens, 2016). A benefit of applying the centrifugal force through a gravitational load is that it is evenly distributing the force across all the nodes. Figure 46 is an illustration of how the gravitational load would be applied.

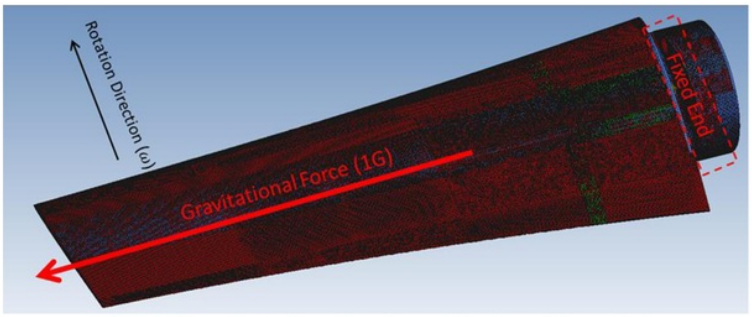


Figure 46 is an illustration of how the centrifugal would be applied

The centrifugal load was calculated by Equation 1 in Section 2.2.1. As a conservative approach, the load was calculated with the blade mass being 21Kg and the centre of gravity point distance 1.859m (1.5 being the radius of the fan rotor + the blade CoG Z distance 0.359). This means the CoG Z distance of the new blade cannot be more than 0.395mm from the base.

$$CF = m \times \omega^2 \times r$$

Equation 7 centrifugal force

$$129.5KN = 21 \times (550 \times \frac{2\pi}{60})^2 \times 1.859$$

Equation 8 centrifugal force at 550RPM

The force is then converted into gravitational load:

$$a = \frac{F}{m}$$

Equation 9 gravitational load

The mass value will depend on the mass of the current design being simulated; for example assume the blade mass is 20.1Kg:

$$6442.786g = \frac{129.5KN}{20.1Kg}$$

Equation 10 gravitational load numbers

Thus the load for the FEA blade model is 6442.786m/s².

7.2.3 Applying centrifugal & stiffness load

Applying both loads consisted of running the model with profile clamps and adding the gravitational load in the same load case (see Figure 47).

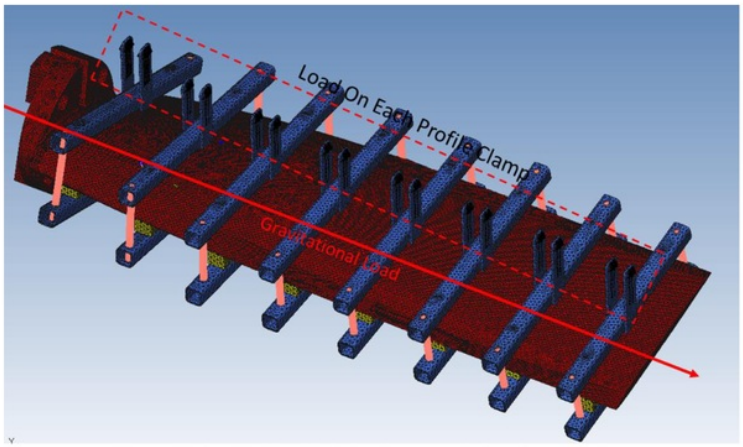


Figure 47 showing how both loads are applied at the same time

When working out the gravitational load, the mass to divide the centrifugal force was required to include the total weight of the profile clamps to avoid over loading the blade in view of the centrifugal force being worked out with the mass at 21Kg.

7.3 Model Constraints

The blade when in operation is connected to the fan rotor by 4 bolts in the steel foot (Fagerberg & Stromberg, 2007). F&S constrained their model by assigning a rigid connection between all nodes at the surface of the bolt holes with a node at the global origin. They did this to simplify the FEA model and accepted this would give a high stress region close to the holes of the steel foot (Fagerberg & Stromberg, 2007).

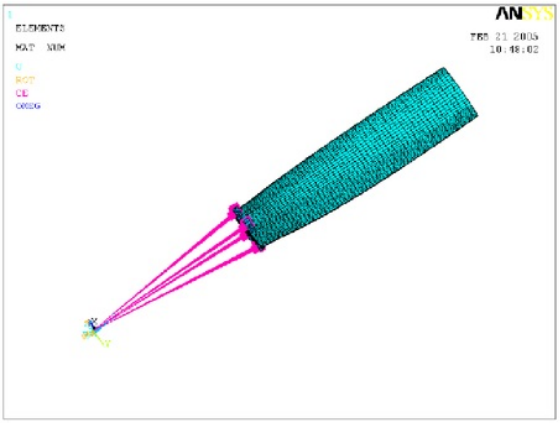


Figure 48 how F&S set up their model constraints (Fagerberg & Stromberg, 2007)

Another approach of constraining the model would be to set the node at the global origin to have a stiffness value that represented the bolts connecting the blade to the fan rotor. However, the information needed to calculate the stiffness was unattainable. Also, there was no information on how stiff the rotor structure was to factor into the model.

In view of this lack of information regarding the stiffness of the structure and connecting bolts, the decision was taken to adopt the same conservative approach as F&S with constraining the nodes around the bolts holes as rigid nodes in 123456.

There are a few ways in which the nodes can be constrained rigidly. In theory it does not matter which approach is selected. However to check that this is indeed the case, a parameter study was carried out on the blade model.

The study loaded the steel foot with 66kN of force and constrained the nodes in three different ways:

1. Spider with a rigid node at the centre
2. Constrained nodes around the edge of the bolt holes
3. Spider to a rigid node at the global origin

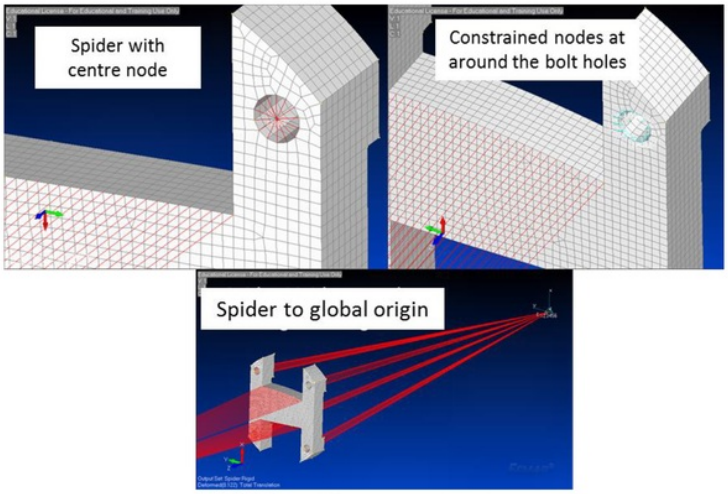
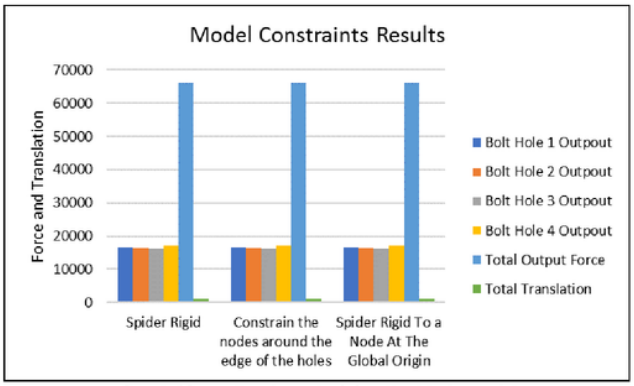


Figure 49 the three different ways that where tested

The point of the study was to see if the reaction forces at the constrained nodes would add up to the input force. If there was a difference, then the way in which the nodes are constrained would influence behaviour.



Graph 13 results of constraining the blade model

Graph 13 shows the results of the study. The graph shows the reactions forces are identical for the different methods.

7.4 Design Optimisation Set Up

7.4.1 Objectives

The objective of the optimisation was originally set to achieve the total mass of the blade within a range of 20Kg to 21Kg, but the software could not accommodate this type of objective. Instead, all the optimisation runs were focused on minimising the total blade mass.

7.4.2 Constraints

Originally the simulation was going to have the following constraints:

- Magnitude displacement of the blade to match the data from stiffness testing
- Have a minimum 1st mode frequency of 38Hz
- Have a minimum composite failure index to control the stress in the layup

However, the software could not facilitate running the failure index and frequency constraints. Only the displacement constraint was able to run in the simulation.

The values used for the constraints are presented in Table 5. The values are applied to the model nodes in the regions of the same position as the GOM tracking points from the test (see Figure 50).

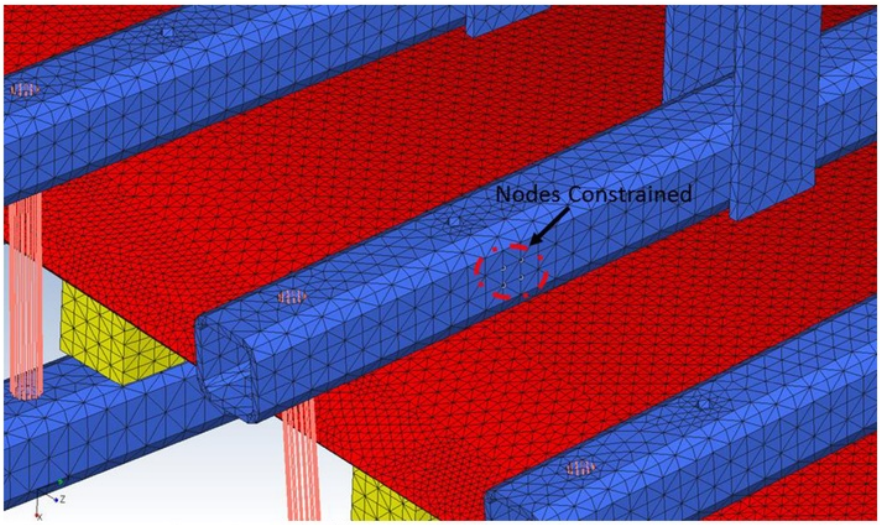


Figure 50 example of the nodes picked for a displacement constraint

7.4.3 Design variables

The number of plies within the composite layup were the variables to change within the simulations. Discrete design variables were chosen as the composite plies could only change by a value of the material thickness (1 ply).

7.4.4 Composite ply topometry

The topometry is the way of controlling what was an acceptable ply size for the new design. If not controlled, the plies could be as small as 5mm².

The topometry was controlled by having a minimum number of elements grouped together for a design variable. The minimum number of elements for a group was found through iterations of testing to find an acceptable ply size for manufacturing.

7.5 Summary Of The FEA Model

Figure 51 is an example of a complete FEA model of the blade.

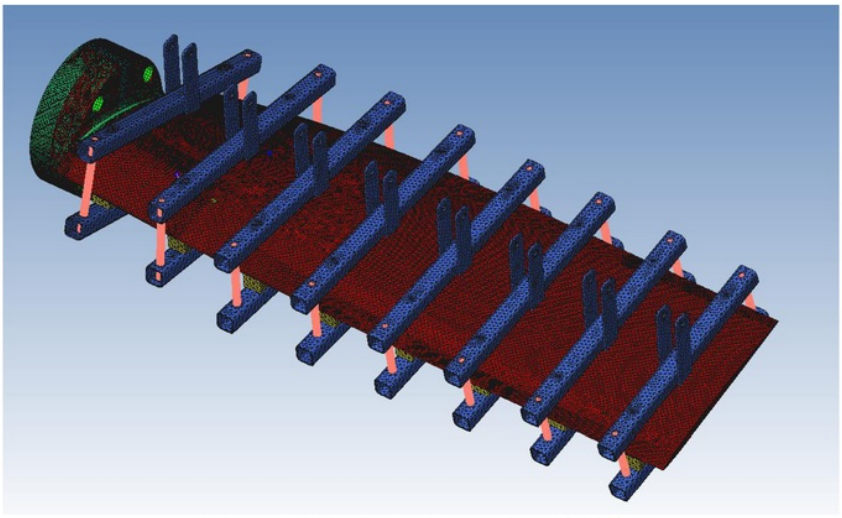


Figure 51 example of a complete FEA model of the blade

Figure 52 shows the main parts included in the blade FEA model and Table 9 is a summary of the settings used to define each part within the model. Note that the summary is a guide as to how the model was set up initially, since the variables were changed/refined throughout the project to optimise results.

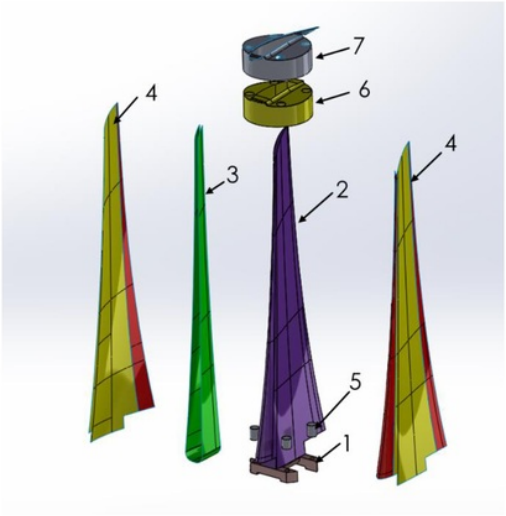


Figure 52 main parts that go into the blade FEA model

Table 9 summary of the settings used to define each part within the model

Part Number	Part Name	Element Type	Element Size	Constraints	Load	Mesh Connection
1	Steel Foot	Solid Bricks/Tets	5mm	Yes	No	Glue Contacts
2	Foam Core	Solid Tets	10mm	No	No	Glue Contacts
3	Central UD Composite	Plate quads	5mm	No	No	Glue Contacts
4	Full Blade Composite	Plate quads	5mm	No	No	Glue Contacts
5	Steel Sleeves	Solid Bricks	5mm	No	No	Glue Contacts
6	Shroud Foam Core	Solid Tets	5mm	No	No	Glue Contacts
7	Shroud Composite	Plate quads	5mm	No	No	Glue Contacts
8	Profile Clamps Block	Solid Tets	8mm	No	No	Glue Contacts
9	Profile Clamps Box Sections	Solid Tets	10mm	No	Yes	Glue Contacts

The built FEA model's quality was evaluated through checking methods which can be seen in **Appendix F**.

8. INITIAL DESIGN & RESULTS

The first design incorporated all the parts listed in Section 6.1. However, to simplify the FEA, only the foot, foam core, central UD 0 laminate and blade full laminate were modelled in. The bill of masteries used in the blade designs are in **Appendix G**.

The first foot design used the same geometry profile of the current blade and the 0 UD plies wrapping around the foot (see Figure 53).

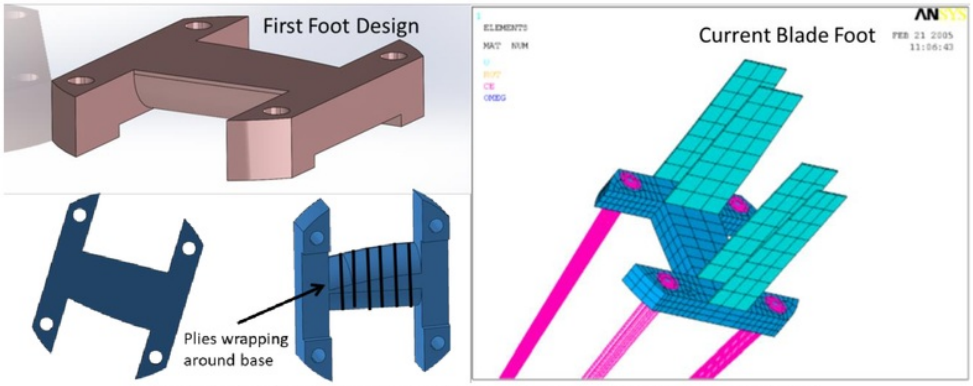


Figure 53 first foot design compared to F&S design (Fagerberg & Stromberg, 2007)

Note the plates on the current blade foot (see Figure 53) are not include in the first design.

The foam core geometry was the exact size of the blade profile. Figure 54 is showing the interaction of the foam core sitting on top of the foot.

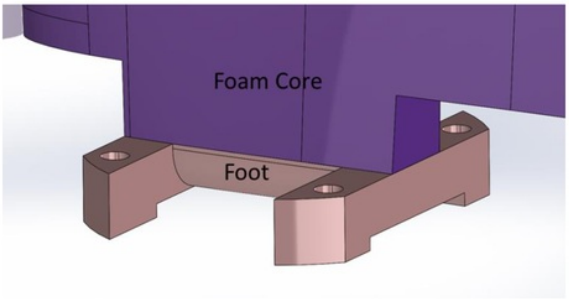


Figure 54 interaction between the foot and core

The UD 0 plies are wrapped around the foot onto both sides of the core, in a similar way to F&S, to connect the core to the foot and transfer the loads to the base of the blade (see Figure 55).

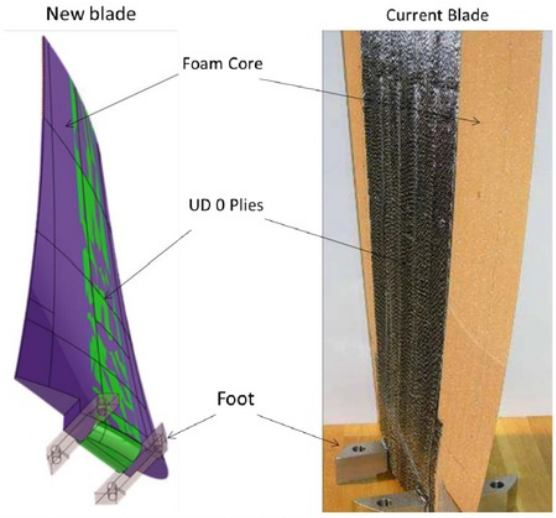


Figure 55 comparing the UD 0 plies current blade to new blade (Fagerberg & Stromberg, 2007)

On top of the UD 0 plies are the main plies that cover the whole blade geometry.

8.1 FEA Model

In Section 5.1 the initial blade design was developed from point load testing rig data. The FEA analysis of the first design was split up into 3 load cases due to the point load testing rig not being able to apply only bending and torsional at the same time:

1. Bending load
2. Torsional load
3. Centrifugal load, bending load and torsional load

The profile clamp was modelled into the FEA model to apply the loads from the test (see Figure 56). The UD 0 plies were meshed separately from the main layup mesh. The meshes were separated to make the centre 0° UD plies the variables for the optimisation. This was done as it was proving difficult to output a sensible layup for manufacturing (ply size not in small patches). This led to the main layup being optimised manually alongside the centre UD 0° plies.

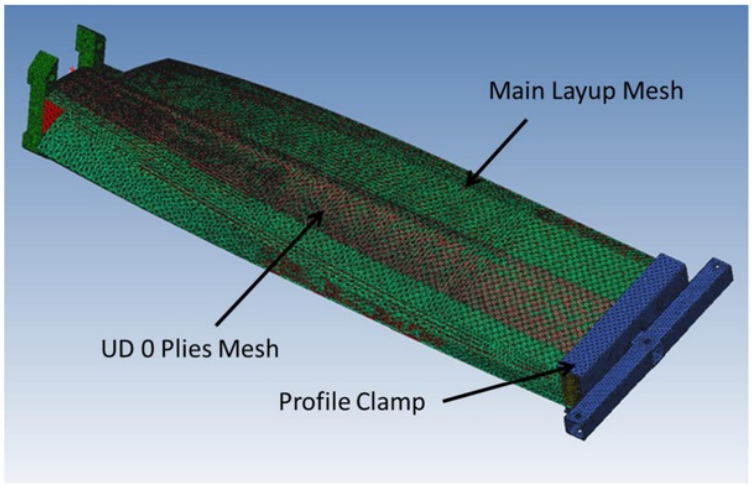


Figure 56 blade FEA model for the initial design

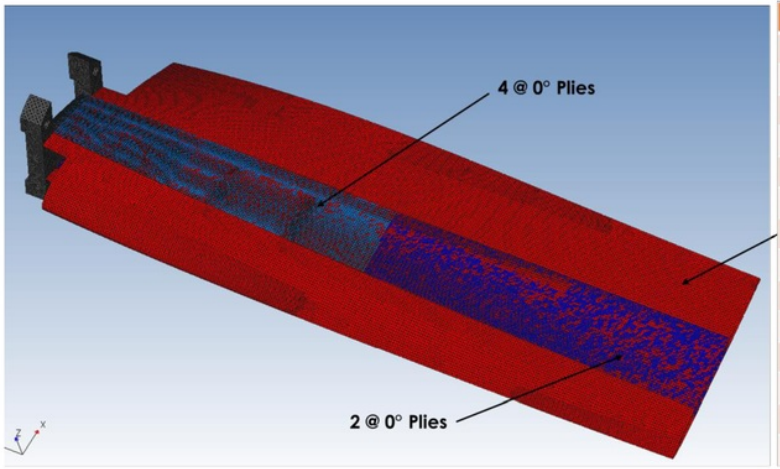
For developing the initial design composite layup, a 3 step process was adopted:

1. **Apply bending load** – apply the load results from the testing and use the displacement data as the constraints. Once the correct stiffness achieved, apply torsional load.
2. **Apply torsional load** – apply the torsional load identified from testing and use the displacement data as the constraints. Once achieving the correct stiffness, apply all 3 loads
3. **Apply all 3 loads** – evaluate design

The composite layup was optimised in steps 1 and 2 which were repeated until both sets of constraints were close to 0% violation.

8.2 Initial Blade Layup

Figure 57 is the optimised layup to meet the constraints of the bending and torsional load optimisation runs.

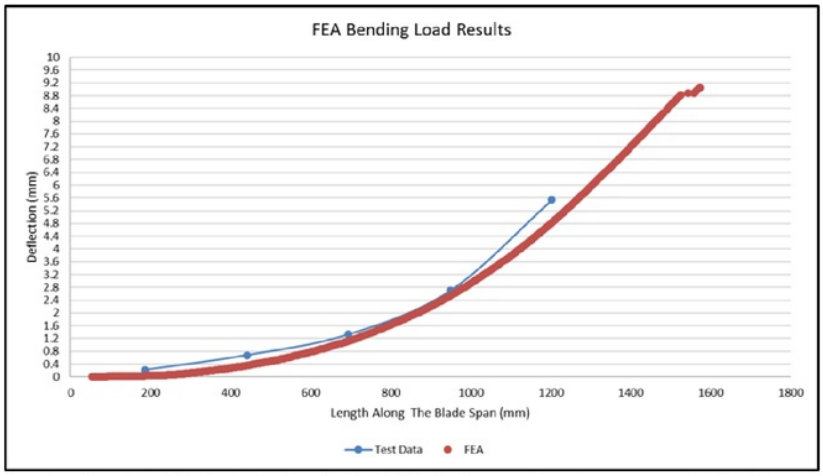


Main Lay Up

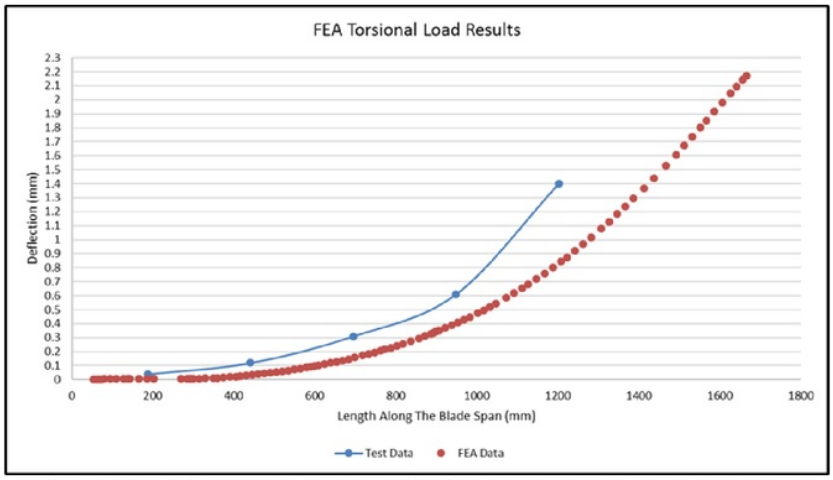
Ply No.	@
1	0°
2	0°
3	0°
4	0°
5	0°
6	0°
7	-45°
8	45°
9	-45°
10	45°
11	-45°
12	45°
13	-45°
14	45°

Figure 57 initial design composite layup

The light and dark blue meshes in Figure 57 is the number of 0° UD plies wrapping around the foot and core with a ply drop off half way up the span length. The red mesh is the main blade layup covering the whole of the blade. The optimisation was tailored to output a symmetrical composite layup. However, to achieve this meant the constraints would be violated as a compromise. Graphs 14 and 15 are the FEA displacement results for bending and torsional loads for the initial blade optimised design. The graphs show the FEA displacement compared to the testing results. Notice the blue graph line stops short; this is because point 6 from the data was left out as it was thought to be an error.



Graph 14 initial blade design bending load FEA displacement results compared to test data



Graph 15 initial blade design torsional load FEA displacement results compared to test date

The violation of the FEA displacement results were not improved any further as the first design was just to initiate developing the blade design. Also, the application of the loads were not considered to be correct for the blade.

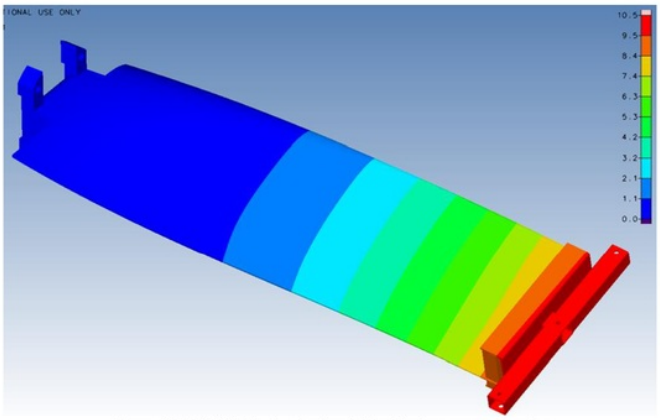


Figure 58 initial blade design FEA displacement results

8.3 FEA Stress Results

8.3.1 Bending load

Figure's 59 and 60 show the highest major and minor principle stresses acting on the composite laminate design. The red circles indicate where the highest stresses occur, thus are potential failure points. The blue circles show where the profile clamp was applying the load in the FEA model. The major principle stress is acting on the top surface of the blade as this side is in tension during the test. The minor stress is on the bottom blade surface as it is in compression during the test.

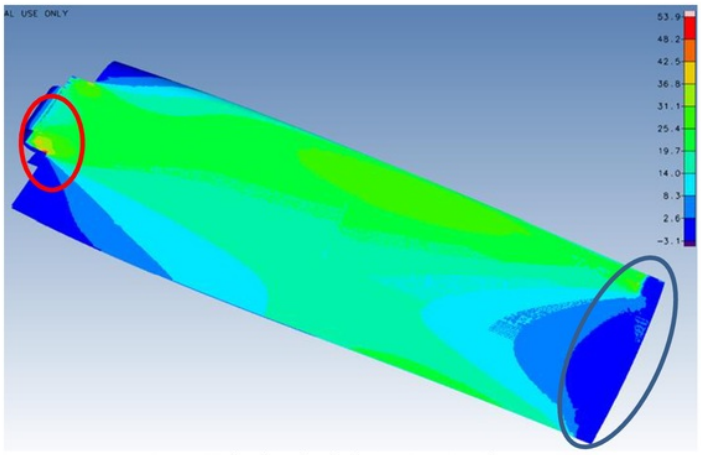


Figure 59 bending load ply 1 major principle stress

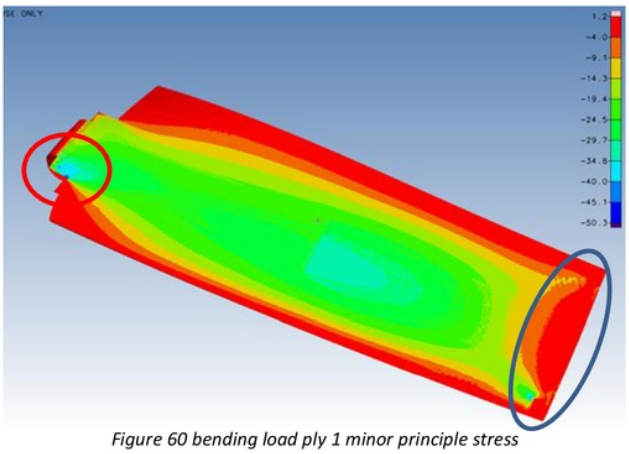


Figure 60 bending load ply 1 minor principle stress

A closer look at the high stress points in the laminate reveal they are on opposite sides of each other (see Figure 61) due to the blade being mounted on the rig at 17° offset creating a twist in the foot area. It is suspected the high stress points are occurring in that area due to sudden change of the composite ply geometry leading to a stress concentration point. Figure 62 illustrates bunching up of stress lines. The stress is also thought to increase in that area due to close proximity to the highly stiff steel foot and the twist.

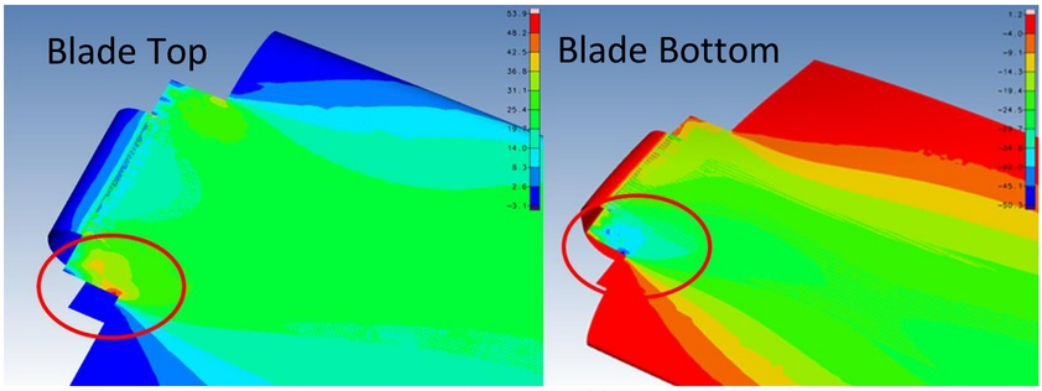


Figure 61 potential failing points of the composite

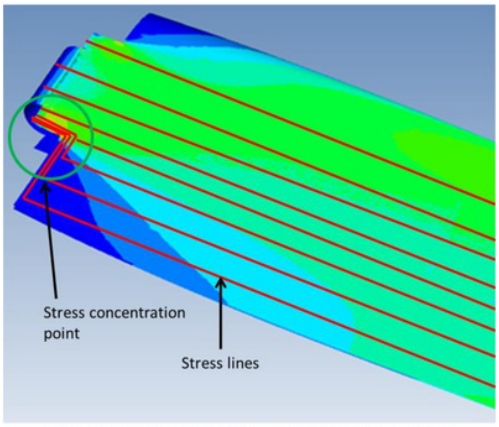


Figure 62 illustration of the stress lines on the blade

The maximum failure index follows a similar trend to that of stress contours with highest points being the same concentration areas (see Figure 63).

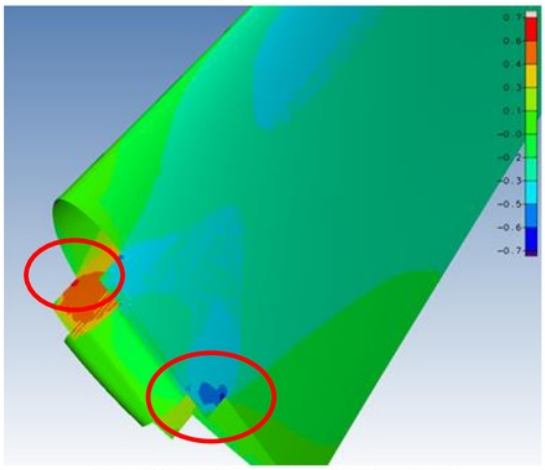


Figure 63 bending load Tsai-Wu failure index

The steel foot has 4 concentration points (see red circles in Figure 64) where the bending load from the composite is being transferred to the 4 bolt holes.

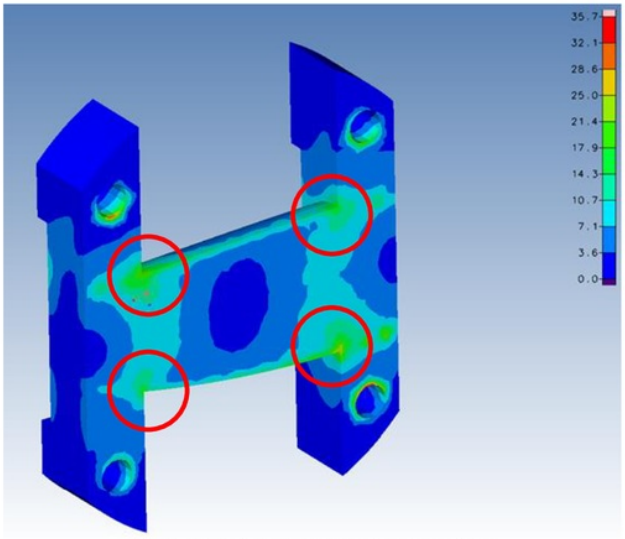


Figure 64 bending load foot Von Mises stress

8.3.2 Torsional load

For the torsional load, the same trends of stress concentration points are evident, particularly in the areas of sudden change of composite geometry. However, it is on both sides of the blade arising from the applied twist. The point where the profile clamp is applying the load can be seen again in Figure 65.

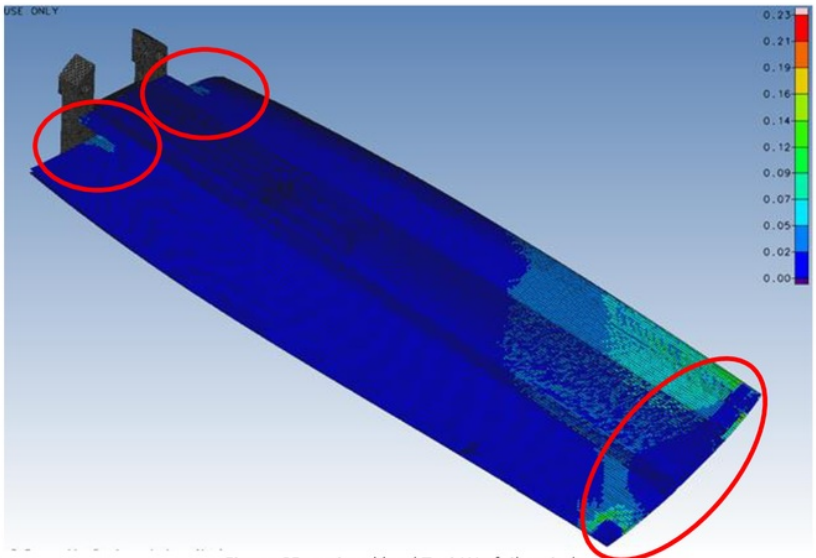


Figure 65 torsional load Tsai-Wu failure index

8.3.3 All 3 loads

Applying all 3 loads including the centrifuge load caused a repetition of stress concentration points (see Figure 66). However, the points were occurring on both sides of the blade due to the high 129.5KN centrifuge load cancelling the bending load; further evidence of this was the deflection in the blade was reduced compared to the test bending data (see Graph 16).

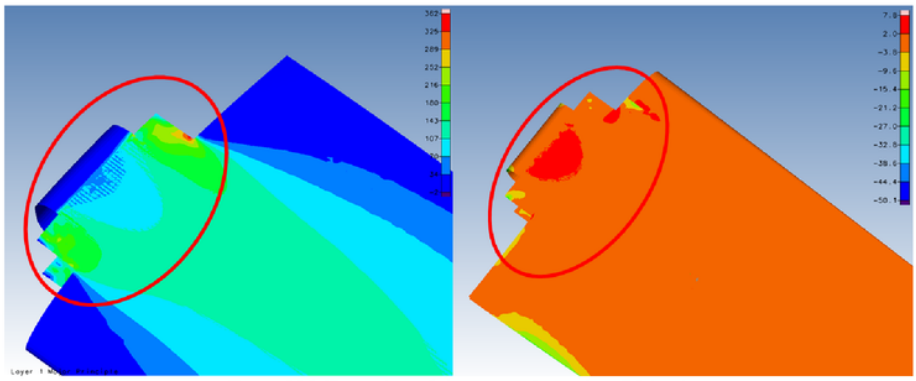
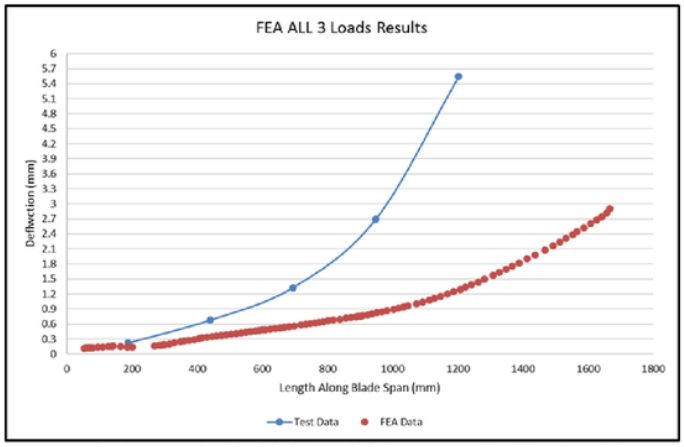


Figure 66 failing points of the composite under all 3 loads



Graph 16 comparing the blade FEA defection against test bending data

The Tsai-Wu failure index showed the high stress points (see Figure 67 blue circles). The highest index however was where the profile clamp was in contact with the blade surface (Figure 67 red circles). This is unexpected as the clamps should not theoretically be applying any more load than from the previous FEA bending load case. Further investigation revealed the clamp was pulling on the composite due to the gravitational acceleration and did not slip due to the nature of the glue contact set up. This means the high index in that area could be due to artificial FEA condition in the glue contacts.

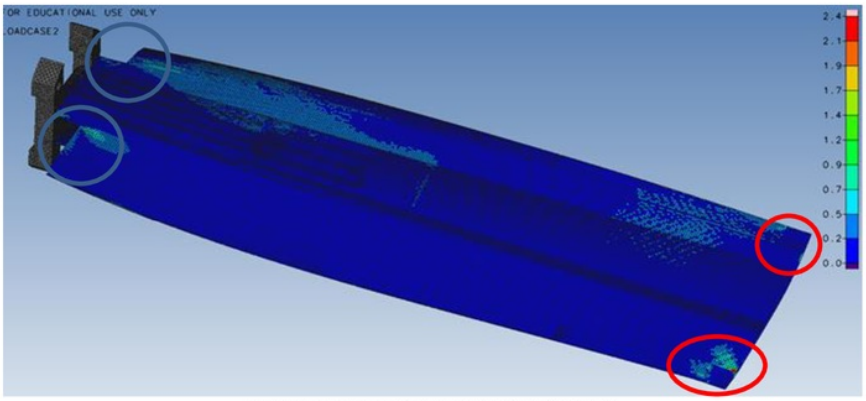


Figure 67 Tsai-Wu failure index for all 3 loads

The steel foot had the high stress around the bolt holes, which is expected with high centrifugal load and the nodes around the holes being constrained rigidly (see red circles Figure 68).

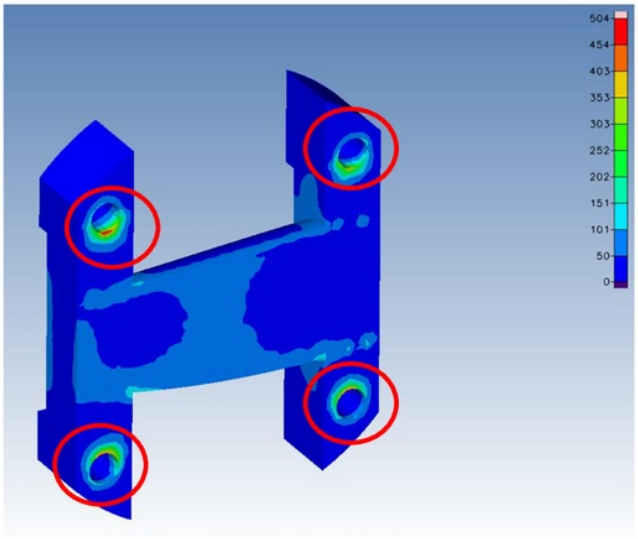


Figure 68 all 3 loads foot Von Mises stress

The stress in the foam core is very low (see Figure 69), which is a good indication the composite skin is absorbing almost the entire load as intended. The core is acting as a sandwich keeping the composite skins apart, as intended.

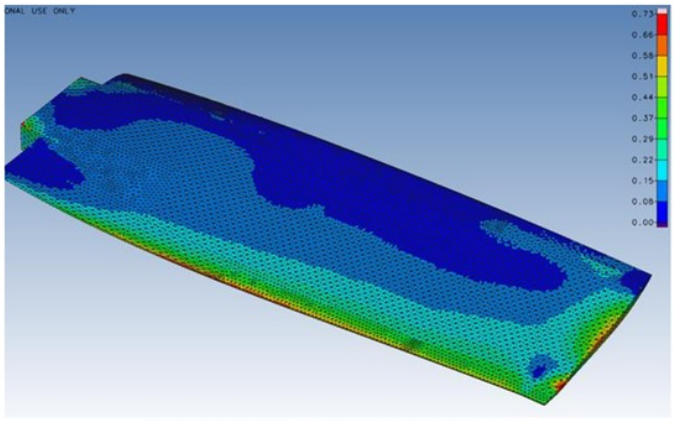


Figure 69 all 3 loads foam core Von Mises stress

8.4 FEA Natural Frequency Results

Figures 70 to 73 compare the FEA natural frequency results from the initial blade design against the LDV results for the first 4 modes. The 1st mode shape is similar to the LDV results; however, the frequency is 112Hz which is exceptionally higher than the current blade of 34.37Hz. This is due to the blade total mass being 10Kg compared to the current original blade of 20.1Kg. The other 3 mode shapes and frequencies are also at variance to the LDV results. This indicates the blade stiffness is not matching up to the current blade as the mode shapes are affected by the part stiffness (Agilent Technologies, 2000).

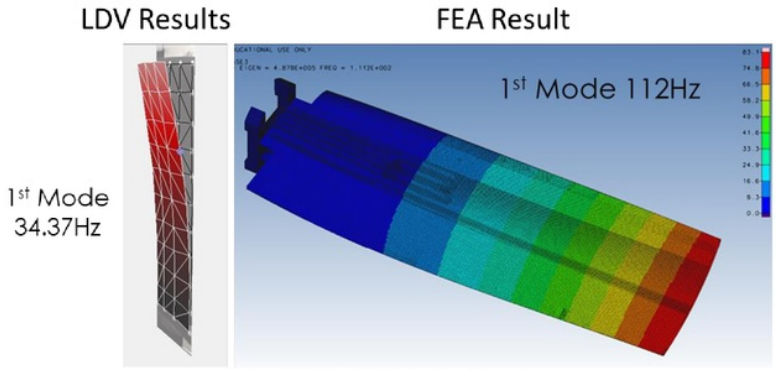


Figure 70 initial blade design 1st mode

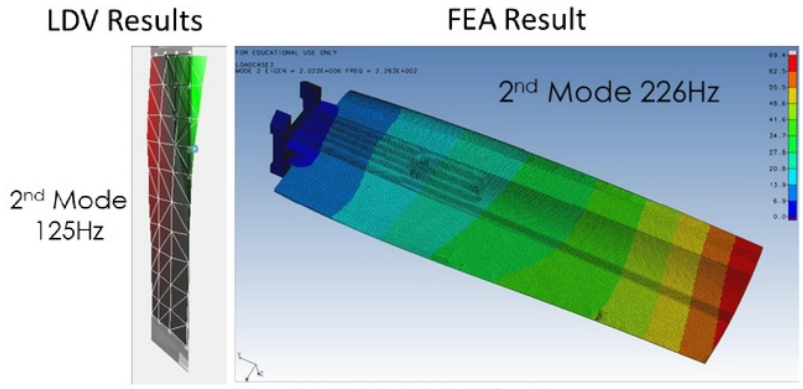


Figure 71 initial blade design 2nd mode

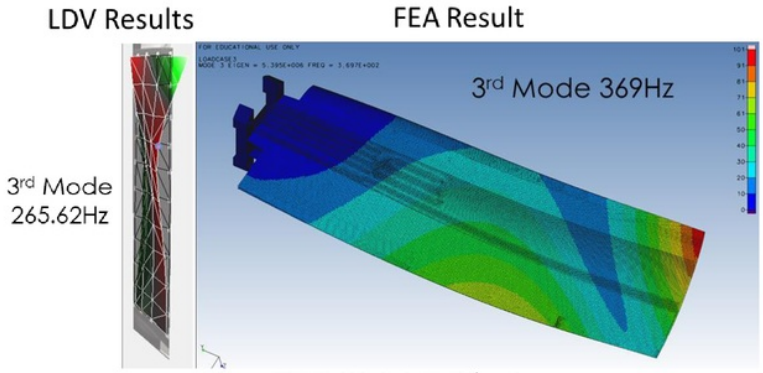


Figure 72 initial blade design 3rd mode

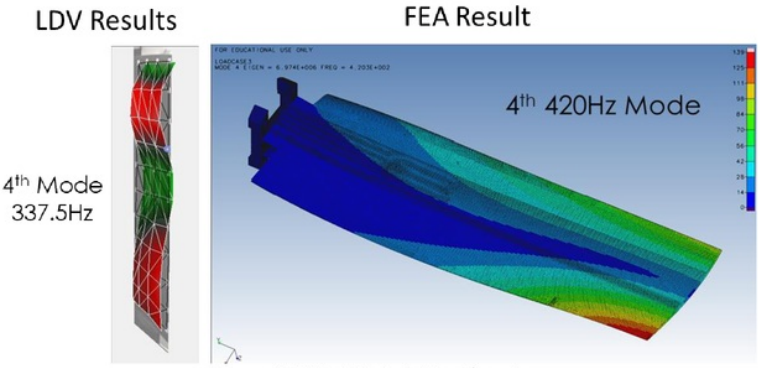


Figure 73 initial blade design 4th mode

8.5 Points To Take Into The Next Design

The initial design gave a good indication that some aspects of the design needed improvement. The following evaluations were made from the results:

- The sudden change in the composite geometry near the blade base is a potential failure in the design. The stress is relatively low in those areas, but this is probably due to a relatively low bending load. When the whiffletree load is applied these points could lead to failure.

  To eliminate the stress points, the geometry would need to be upsized. However, the composite in that zone was reduced in size because of the base shroud. An alternative is to transfer the load to the steel foot progressively commencing further up the blade span.
- Mass needs to be added to the design. This will assist in determining what frequency the mode shapes occur at.
- The shroud parts of the blade design need to be added into the FEA model. This will give a better result of what the total blade mass is and give more accurate results with the mode shapes.

9. MANUFACTURING CONSIDERATIONS

The developments in the blade design covered in this section were made over a series of design iterations. **Appendix H and I** show results of the two interim blade designs.

9.1 Tooling Scheme

The new blade will be manufactured using prepregnated composite materials. *Lentus* opted to cure the material using pressure autoclave. To achieve this, a tooling scheme was developed.

The tooling assembly for the blade comprised a bottom and top composite mould (see Figure 74). A composite mould was elected over aluminium as this would have a small amount of flex during curing to assist with ply consolidation (Lentus Composites, 2019).

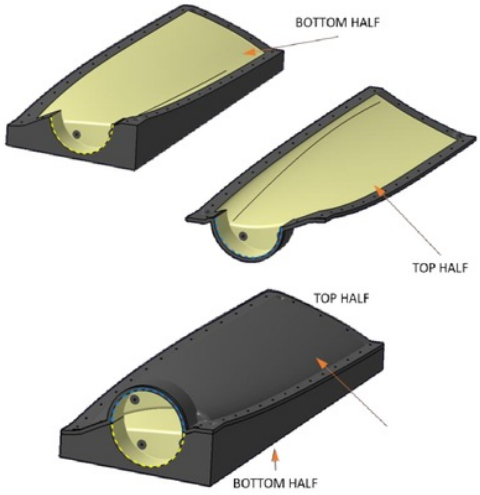


Figure 74 mould assembly (Lentus Composites, 2019)

Ply consolidation is one of the main concerns with manufacturing the blade with prepregnated materials, especially between composite ply stack and core material.

To assist with the consolidation, the plies wrapping around the steel foot will be laminated to the core and foot instead of into the mould. The rest of the plies will be laminated into each side of the mould (see Figure 75). This approach assists with reducing consolidation as it allows the operator to carry out vacuum de-bulks during laminating, which compresses the plies (Lentus Composites, 2019).

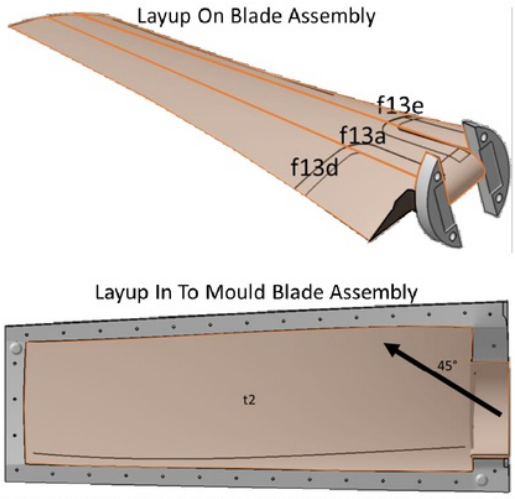


Figure 75 both ways of laying up the blade (Lentus Composites, 2019)

Once the lamination is complete, the blade will be assembled with the shroud core parts and placed into the mould assembly for curing (see Figure 76) (Lentus Composites, 2019).

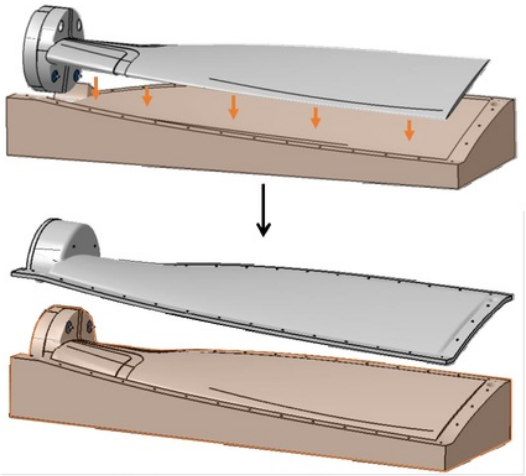


Figure 76 assembling blade into the mould (Lentus Composites, 2019)

9.2 Composite Consolidation

The consolidation of the plies can occur in a number of ways:

1. Vacuum de-bulks
2. Small amount of mould flex during curing from cleave pressure
3. As the mould assembly closes, some crushing of the plies against the core

These 3 consolidation processes help with the main span area of the blade, but not the plies around the foot and shroud zone. The nature of the blade design leaves the base open to

allow autoclave pressure to compress an intensifier into the foot area which consolidates the plies around the foot (see Figure 77) (Lentus Composites, 2019).

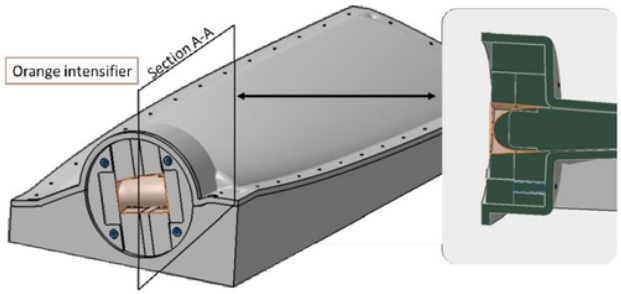


Figure 77 Applying autoclave pressure (Lentus Composites, 2019)

The intensifier pushes the shroud core pieces into the mould to consolidate the shroud plies. However, this only works in one direction as shown in Figure 78 with the solid red arrow.

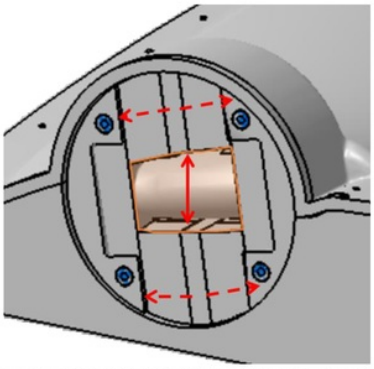


Figure 78 applying pressure to shroud area (Lentus Composites, 2019)

To apply pressure in the chequered red arrow direction, a silicone wedge is added into the blade shroud design (see Figure 79) which expands from the heat generated from the curing process and rams core parts into the shroud plies.

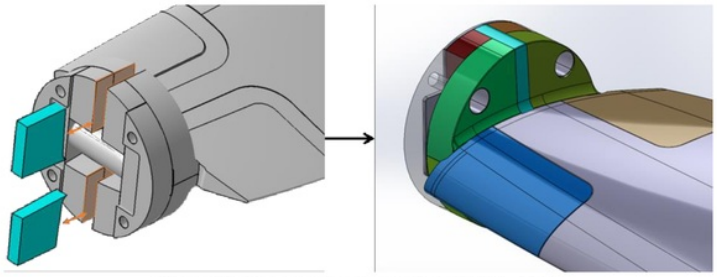


Figure 79 silicone parts (Lentus Composites, 2019)

The foam core in the area of the shroud is considered to contribute little or no structural rigidity to the overall blade design and consequently the stresses are low. To help with

assembling the blade during manufacturing, the core is split into 8 parts, which also accommodate the silicone wedges and steel sleeves (see Figure 80).

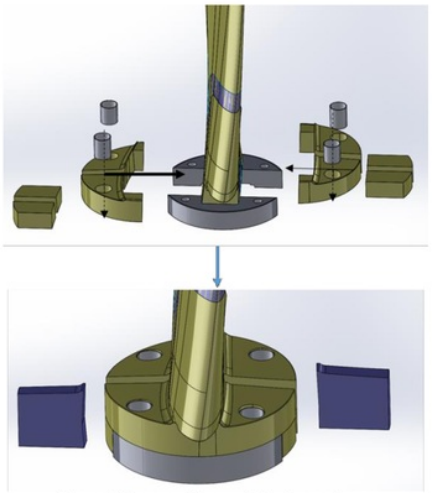


Figure 80 assembly parts in shroud area

9.3 Load Transfer

F&S used steel plates originating off the steel foot (see Figure 81) and extending into the foam core to help transfer the load to the foot (Fagerberg & Stromberg, 2007). Reviewing the FEA results of the initial blade design, the guess would be that the gradual load transfer plate was to reduce the concentration points on the laminate.

It was considered using the plates in the new replica blade design would not have the same effect as it was not intended to be manufactured using RTM, which fills in any crevices with resin, to which the plates would bond with the foam core (Mattews & Rawlings, 1994). The resin around the plates would also create a washer effect to disperse the load into the plates, rather than the plates cutting into the foam (Lentus Composites, 2019). Using prepregnated material does not have the benefit of filling crevices, thus it would be difficult to bond in the plates and over time would cut into the foam.

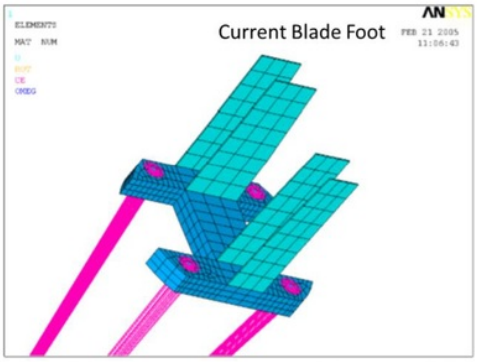


Figure 81 F&S foot design (Fagerberg & Stromberg, 2007)

A suggestion by *Lentus* was to use a composite spar instead of the plates to transfer the load (Lentus Composites, 2019) (Richmond, 2018). A paper by Matthew J Nicolas into the in-flight load and shape of composite aircraft wings found using composite spars in the wing reduces the stress at the connection point to the fuselage (Nicolas, 2016). Also, a paper by Antonio Paolozzi used a composite spar in a carbon skinned with polystyrene core plane wing (see Figure 82) to reduce stress and increase stiffness (Paolozzi, 2006). It appears there is experience to draw on for using a composite spar to reduce the stress near the steel foot with the added benefit of increasing stiffness.

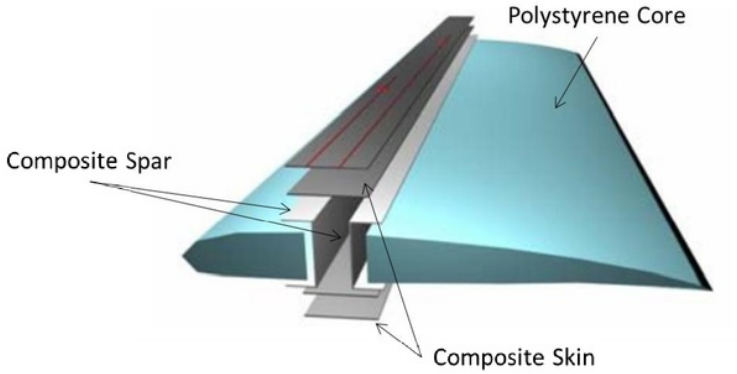


Figure 82 Antonio Paolozzi composite wing (Paolozzi, 2006)

Figure 83 is the spar design developed for the new blade. The design functions by wrapping plies around the main foam core and the steel foot. Note in Figure 83 the foot design is modified to have an extruding part for the composite to warp around. To accommodate the spars, the main core is split giving leading and trailing edge cores. The spar length and overhang was developed in the second blade design, the results of which are in **Appendix H**.

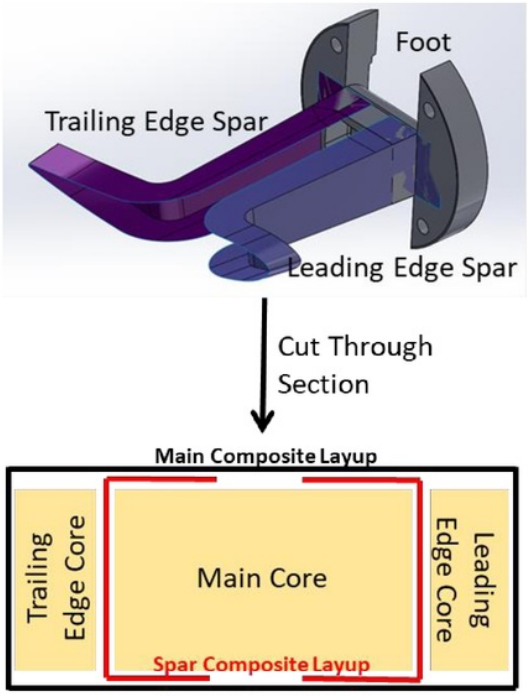


Figure 83 composite spars

Figure 84 shows how the spars fit into the blade design and how the blade would be layed up.

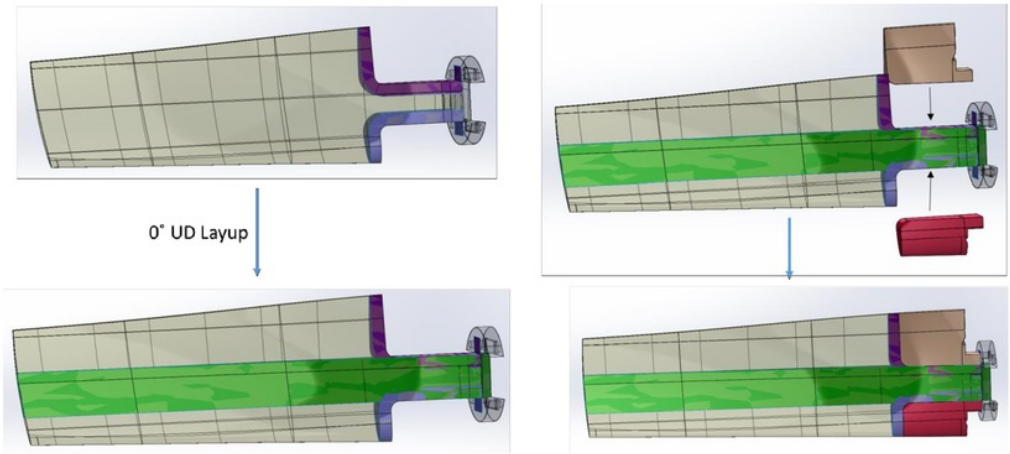


Figure 84 laying up spars

Figure 85 is showing the differences between the initial and the updated foot design for the spars.

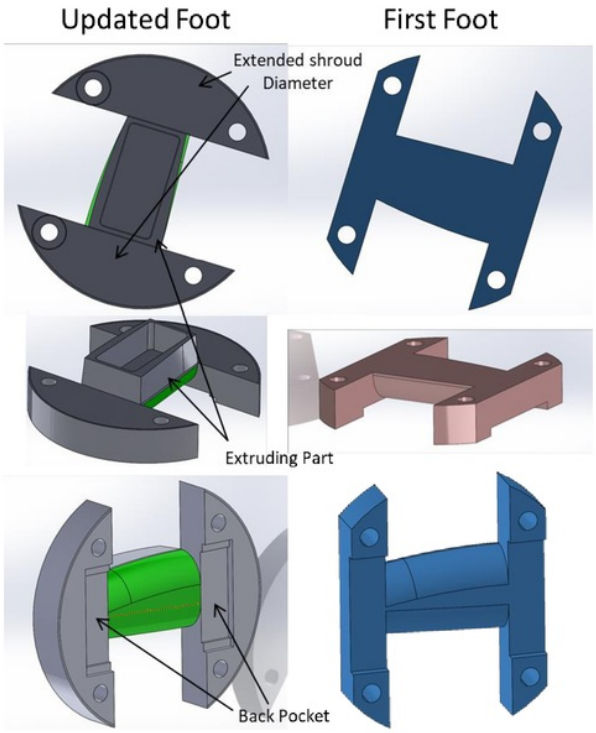


Figure 85 comparing updated foot with first design

The updated foot design also had the following parts incorporated into the design:

- The foot shape was extended up to the shroud diameter to add mass to the design. This also had the added benefit of expanding into the mould to consolidate shroud plies.
- Extruding part for spars and adding mass. The extruding part also has a pocket for the main core to sit into, which when assembling the blade acts as a location pin.
- Pocket on the back of the foot for the back plate.

9.4 Blade Mass Control

The current original blade has the base covered in composite, shown as yellow in Figure 86. The new replica blade cannot cover the base in composite material as the foot requires being exposed to autoclave pressure for ply consolidation.

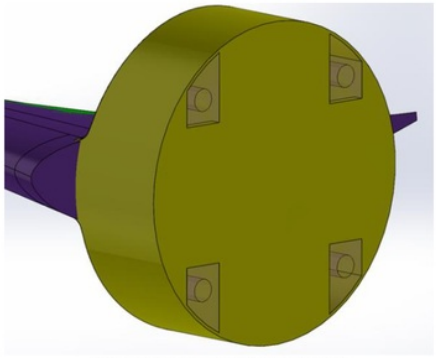


Figure 86 current blade shroud

To protect the internal materials and close the new blade up, a stainless steel back plate was designed. After curing the blade, the back plate can be bonded into place (see Figure 87). Stainless steel was selected cover a composite plate for minimising weight contribution to the total blade mass. The back plate provides the added benefit of being non-structural which means it can act as a way of controlling the total blade weight after curing. The back plate gives 2.3Kg of margin for adjustment of total blade weight.

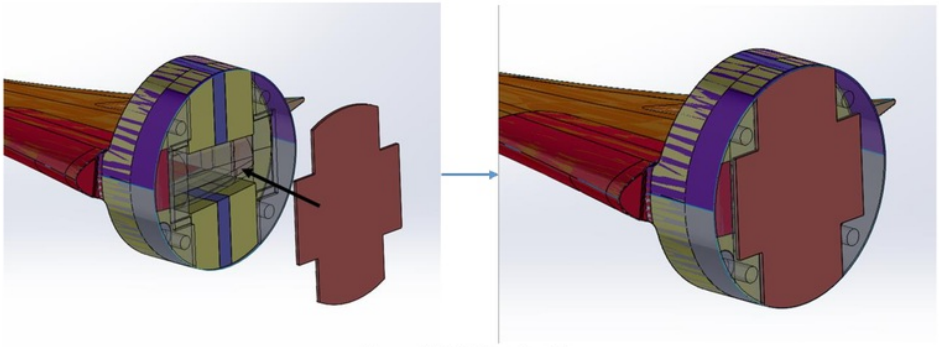


Figure 87 blade back plate

9.5 Optimisation Ply Shape Control

The first few design iterations of the blade centre UD laminate wrapping around the foot as a separate mesh from the main laminate. To give more freedom to the optimisation, the meshes were combined to give one main laminate mesh for the blade. The spar and shroud laminates were still separate meshes (see Figure 88).

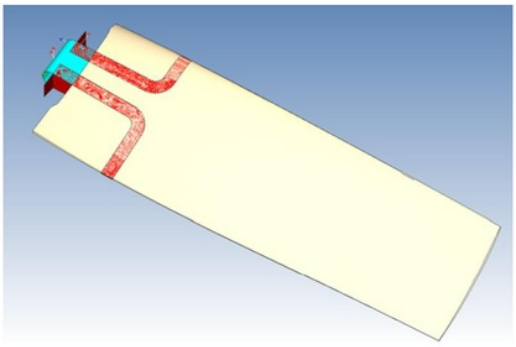


Figure 88 updated composite mesh

Even with applying the ply topometry controls, the laminate designs outputted by the software were either not symmetrical or in small patches (see Figure 89). The former was mainly down to the software attempting to make the layup as light as possible. This was not a problem in terms of manufacturing this type of layup, but when only applying the bending load in one direction, there was no guarantee that if the blade was loaded in the opposite direction, it would achieve the same stiffness performance, nor cope with stresses. Similarly, this can also be said for having a symmetrical laminate due to profile shape, but the risk is minimal in comparison to the non-symmetrical laminate.

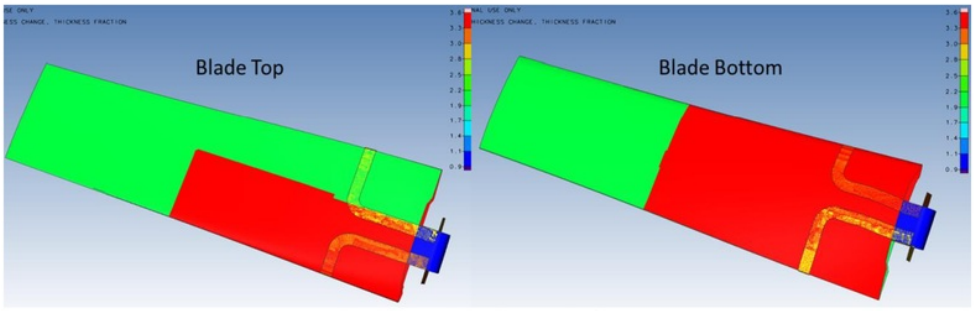


Figure 89 optimised composite layup

Not outputting a symmetrical laminate was the limit of the software capability on this project. To progress the project forward, the best ply shape design was taken and specified to be symmetrical, Figure 90 was the optimum shape.

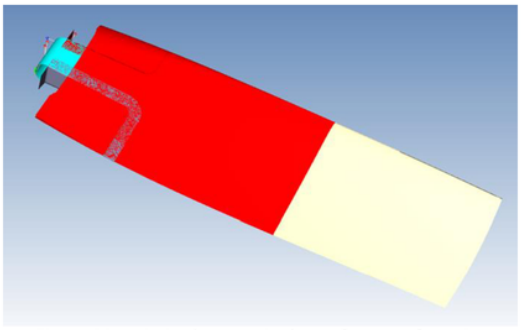


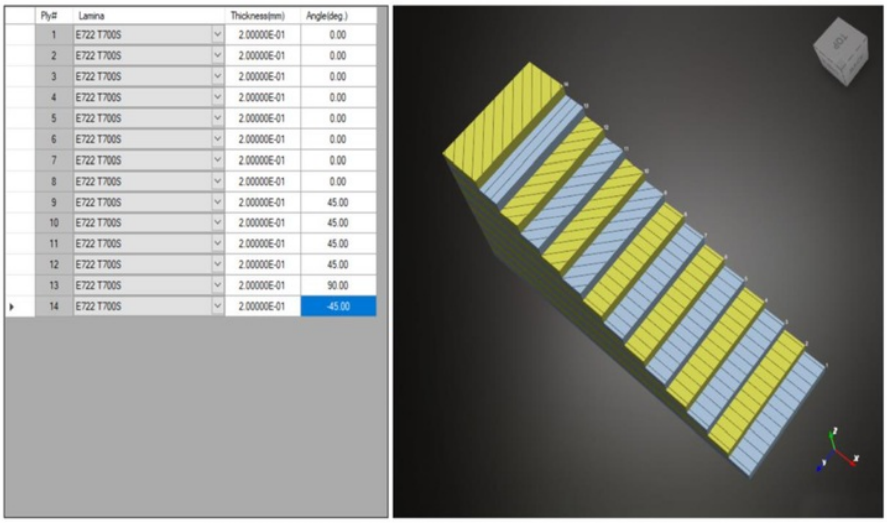
Figure 90 optimised composite layup for manufacturing

The software tended to produce composite layups that were un-balanced, for example the layup in Table 10 where the ply orientation was unidirectional. This is another limitation of the software.

Table 10 showing a un-balanced layup

Ply No.		
14		-45°
13		-45°
12		45°
11		45°
10		45°
9		45°
8		45°
7		45°
6		0°
5		0°
4	0°	0°
3	0°	0°
2	0°	0°
1	0°	0°
	Foot	Core Section 1

The solution was to take the output layup and use CLT to find the Ex and Ey stiffness values. Then use *Helius Composite* software to reorganise the layup to be balanced and achieve the same Ex and Ey (see Figure 91).



Ply#	Lamina	Thickness(mm)	Angle(deg.)
1	E722 T700S	2.00000E-01	0.00
2	E722 T700S	2.00000E-01	0.00
3	E722 T700S	2.00000E-01	0.00
4	E722 T700S	2.00000E-01	0.00
5	E722 T700S	2.00000E-01	0.00
6	E722 T700S	2.00000E-01	0.00
7	E722 T700S	2.00000E-01	0.00
8	E722 T700S	2.00000E-01	0.00
9	E722 T700S	2.00000E-01	45.00
10	E722 T700S	2.00000E-01	45.00
11	E722 T700S	2.00000E-01	45.00
12	E722 T700S	2.00000E-01	45.00
13	E722 T700S	2.00000E-01	90.00
14	E722 T700S	2.00000E-01	-45.00

Figure 91 Helius Composite software with optimised layup

10. PROJECT ERRORS & SOLUTIONS

A complex project of this nature is unlikely to be completed without encountering some errors/blind alley investigations. Two such errors identified by the author as impacting on the project in time and resources are discussed in detail in this section.

10.1 Composite Material Error

When carrying out the analysis of the second blade design, the composite failure index was yielding a value significantly above 1 (see Figure 92).

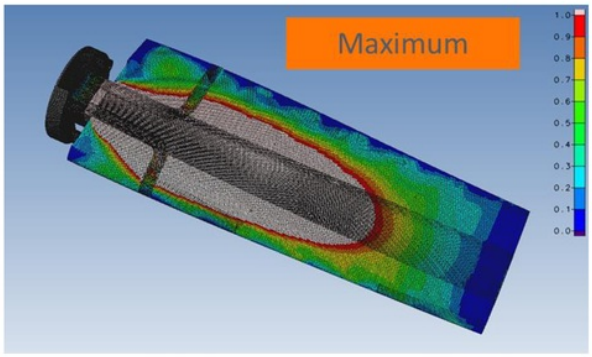


Figure 92 blade design 2 maximum Tsai-Wu failure index

Further investigation showed all of the plies were failing (see Figure 93). However it was restricted in the region of the blade underside face. Indicating that it was only in the areas where the plies are under compression, stress was the issue.

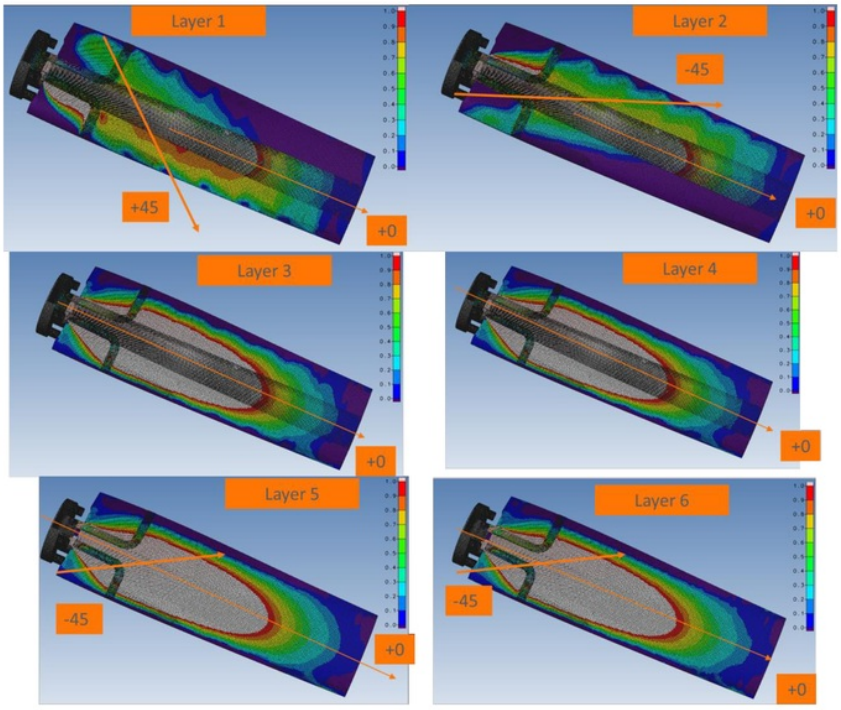


Figure 93 blade design 2 individual ply Tsai-Wu failure index

The compression stresses were found to be unexpectedly low (see Figure 94) in comparison to what *Torayca* states the T700S fibre can withstand under compressive load (Torayca, 2018). This led to questions which material properties were being used in the FEA model.

Upon inspection, the compressive strength of the composite was set to 100MPa compared to *Torayca's* data of using the fibre in a prepregnated resin of 1470MPa (Torayca, 2018). This finding put into question all the material properties being used which were calculated from *CODA* software at the beginning of the project. However, the results were clearly wrong when comparing with *Torayca's*.

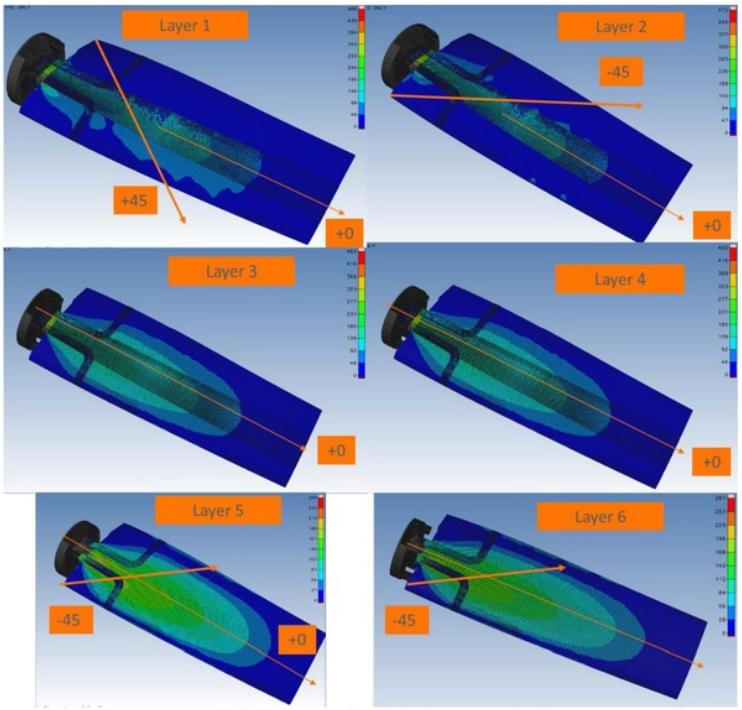


Figure 94 blade design 2 individual ply minor principle stress

The incorrect material properties had been used since the start of the project, which puts into question the validity of the FEA results up to this point. The following are the parts of the project that used the properties:

- **Coupon testing** – The coupon testing used the incorrect properties, but the testing results against the FEA results had good correlation. The reason for this was the longitudinal young's modulus (Ex) was correct to *Torayca's* data and the fibres in the part ran longitudinally, which meant the bending deflection would be correct. The stress results of the plies also had good correlations because the failure index was calculated independently from the major and minor principal stresses. The main material properties affected were the compressive strengths and transverse modulus (Ey).
- **The first blade design** – Again the fibres in the first design ran mostly longitudinally meaning the results were valid. However, the failure index results are incorrect. In theory the index should have been a lot lower and this might be another reason why in the vicinity of the profile clamps, the composite was failing. Unfortunately, the incorrect properties were not noticed at this stage of the project because the bending loads were very small so that it did not put the fibres under much compression stress, thus did not see the wide failure in the same magnitude as design 2.

10.1.1 Solution

After seeking advice from *Lentus,* Graeme Hyson recommended using *Torayca's* longitudinal properties and then *TenCate's* E722 transverse properties as a starting point (Hyson, 2018). In theory, the longitudinal properties of the UD would be more or less correct as the fibre is doing all the work. In the transverse direction, it would be the resin properties withstanding the load, but it is difficult to predict to what extent (Kaw, 2006).

The solution would be to use the *Torayca's* and *TenCates's* properties, but design the blade composite layup to be insensitive to the transverse values. At the end of the blade design, carry out a parameter study comparing how the performance of the blade would change using different transverse properties from the original. This would identify if the design is in-sensitive (Hyson, 2018).

10.2 FEA Model Glue Contact Error

The principle of how the glue contacts work is to maintain two meshes together and the FEA software applies a force in opposite directions at the surface nodes to keep the meshes in equilibrium to one another and stay in contact. Figure 95 illustrates this theory. The total force needed to keep the meshes together divided by the applied element area to give the glue traction, which is essentially the bonding stress on the glue (Siemens, 2016). For the blade analysis, this output can advise the operator if the composite stack is de-laminating from the core and foot under load if the glue traction is exceeding the interlaminar shear strength (ILSS).

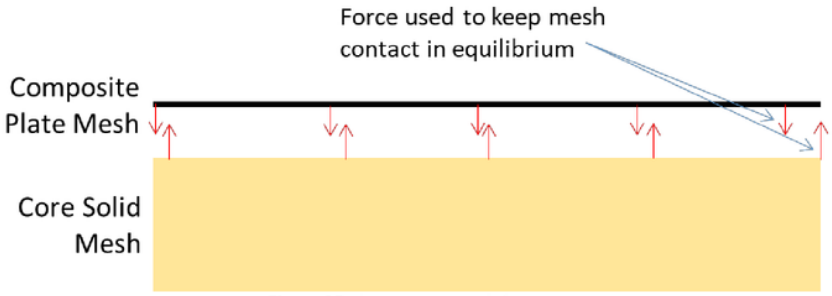


Figure 95 glue contact mesh forces

During the analysis of the one of the blade designs, Graeme Hyson advised to check the values in the glue traction. Figure 96 shows the results, but the colour contours were showing very high traction stress and the plies de-bonding from the core and foot. Hyson vetted the findings and concluded they were not accurate for two reasons:

1. Extremely high traction values in some areas (Hyson, 2018).
2. The colour contour was patchy, indicating the nodes of the meshes are not connecting correctly (see Figure 96) (Hyson, 2018).

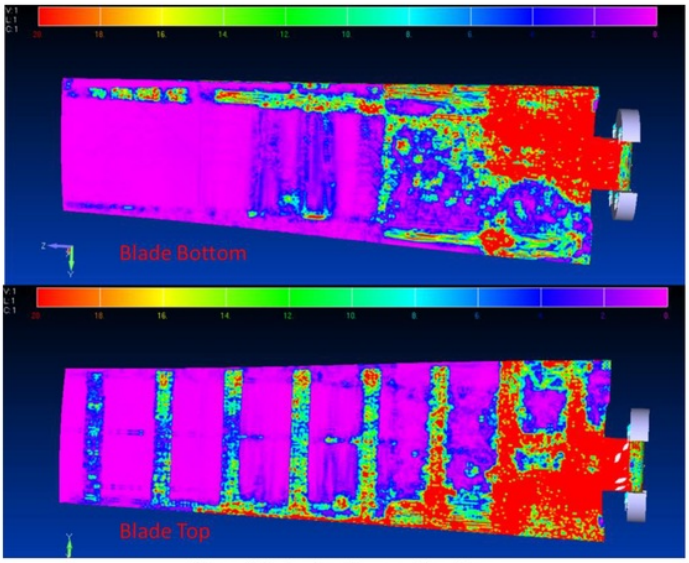


Figure 96 glue traction on old settings

A study by Jonathan Buck into glue contact settings stated the glue traction contour should have a smooth transition (see Figure 97).

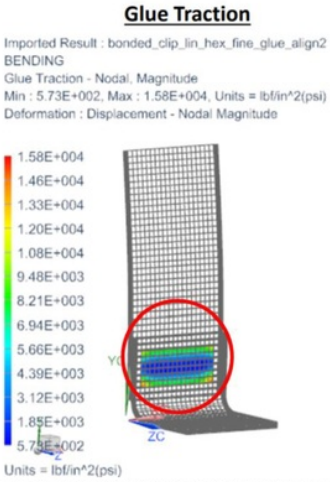


Figure 97 Jonathan Buck's FEA glue traction results (Buck, 2014)

Looking at the contour arrows on the blade, the resultant directions for each vector across the blade surfaces were randomised (see Figure 98).

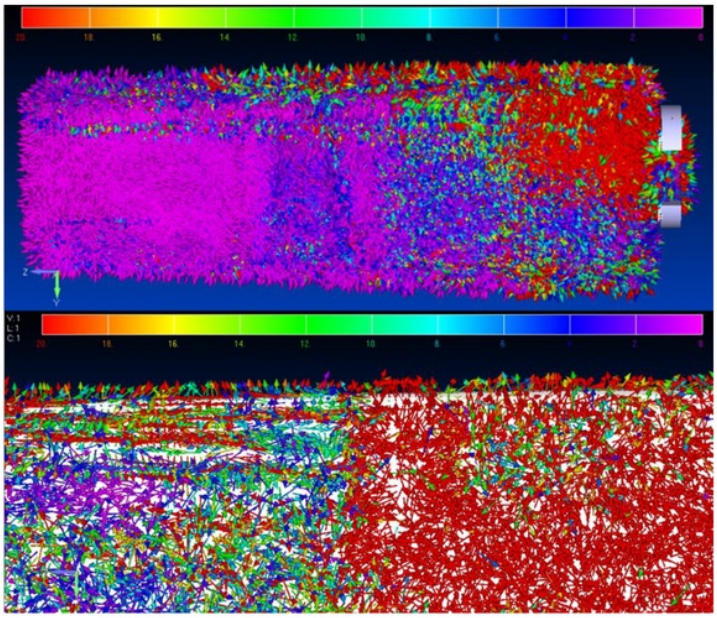


Figure 98 resultant glue traction contour arrows on old settings

Graeme Hyson's own study into glue contacts found the contour arrows resultant directions should be facing in similar directions and not have sudden changes (for example the results in Figure 99) (Hyson, 2018).

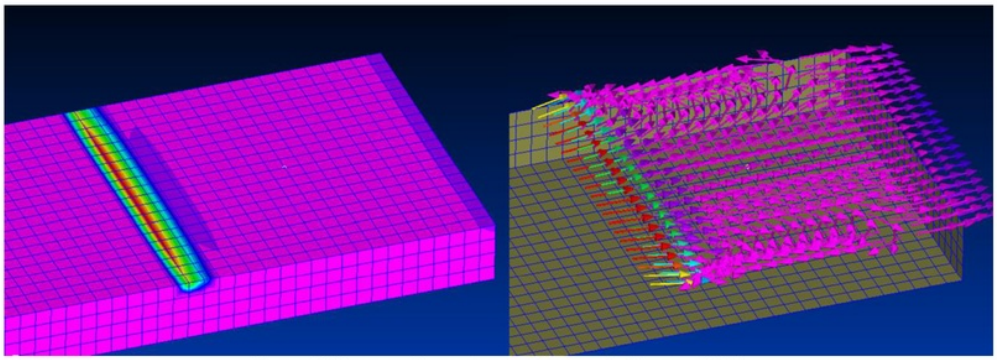


Figure 99 Graeme Hyson glue traction results **(Hyson, 2018)**

The blade contacts were not showing similar findings of the two studies, meaning aspects of the glue contacts were not working. In hindsight, the coupon testing study into glue contacts should have been examining the glue traction results.

10.2.1 Solution

The solution adopted was to re-visit coupon testing to obtain improved results and use a new coupon model which was more representative to the blade design. Figure 100 explains the coupon model set up for the study.

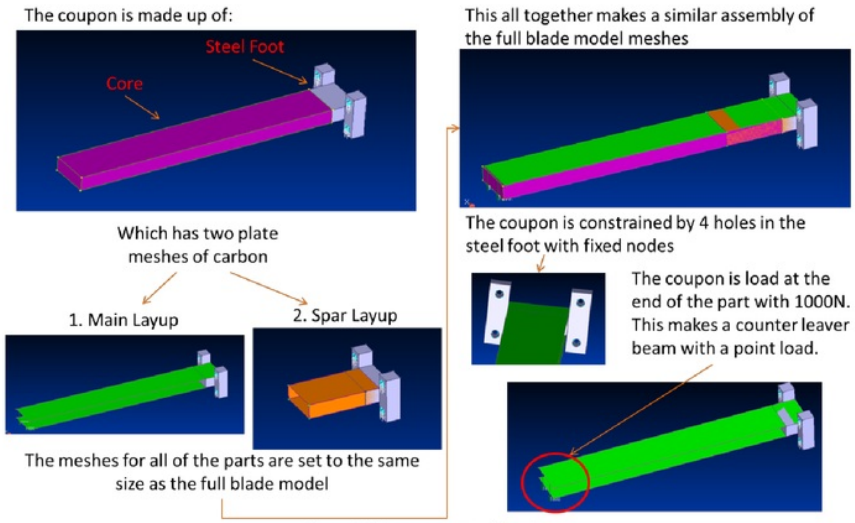


Figure 100 coupon model set up

Running the coupon with the same glue contact settings gives the same patchy results (see Figure 101).

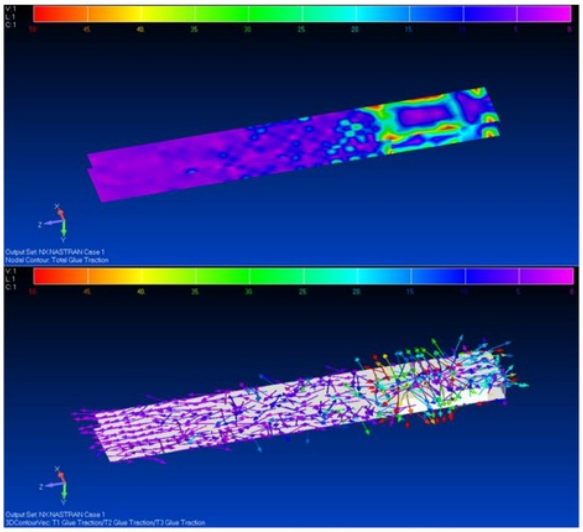


Figure 101 coupon results with current settings

10.2.2 Study results

The study tried changing the aspects that would affect how the contacts connect the mesh surfaces nodes together, the following was tested:

- **Refining Current Glue Contact Settings** – The settings were changed to the other settings explored in the original study, but to no effect. Other changes were tried, for example, increasing the search distance for connecting the nodes and checking the surface vectors directions, but again to no discernible improvement.

- **Spring Elements** – Changing the contacts to spring elements realigned resultant contour arrows faced in similar directions, but the glue traction value was still very high (see Figure 102).

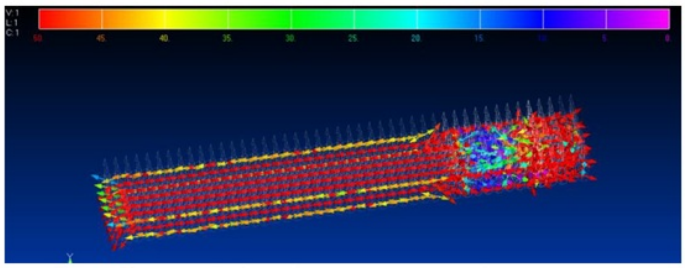


Figure 102 results of using spring elements glue traction contour arrows

The spring elements give fairly different displacement and stress contour results in comparison to the glue contacts (see Figure 103). The results of the previous study found glue contacts best for correlation.

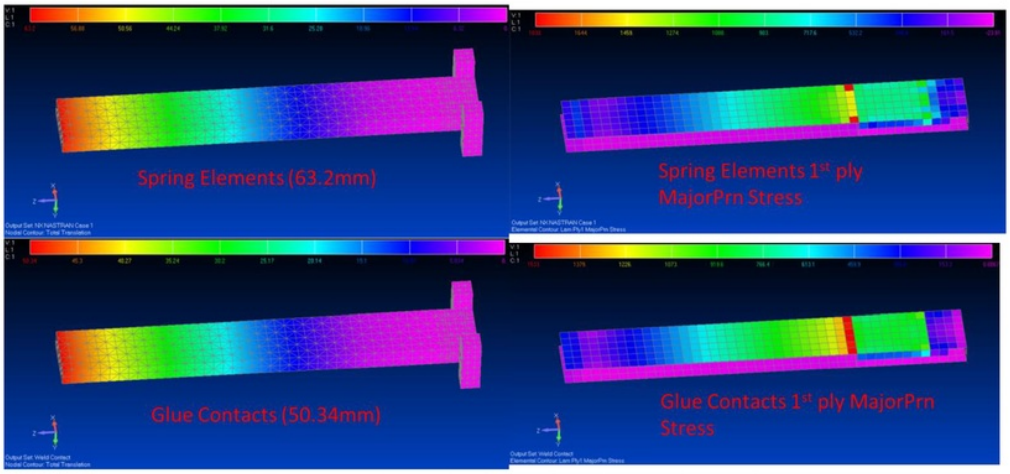


Figure 103 comparing FEA results of using glue contacts and spring elements

- **Refining Plate Meshes** – Using the glue contacts with the current settings but refining the composite plates meshes had no effect on the contours.
- **Refining Core and Foot Solid Meshes 2mm Tetrahedral** – Refining the core and foot solid meshes to 2mm element sizes resulted in a significant improvement; the same displacement results but the glue traction contour and resultant arrows were matching expectation. Looking at Figure 104, the arrows and contour colours had a smooth transition. The highest traction value was centred where composite changed from being attached from the foot to the foam core (see red circle). This was expected due to the sudden change in core stiffness. However, the contour on the foot part of the model was still patchy.

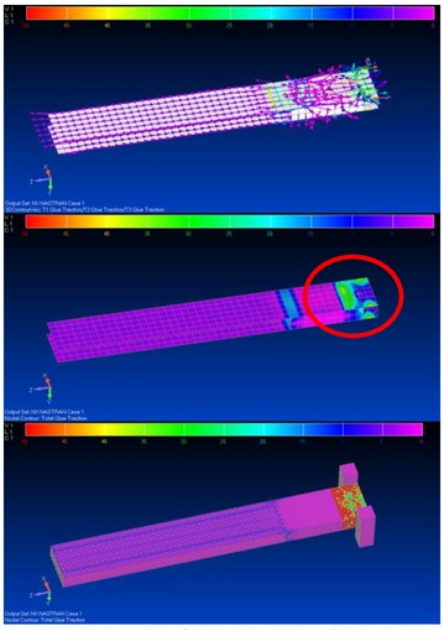


Figure 104 results of using 2mm tets glue traction

- **Refining Core and Foot Solid Meshes 1mm Tetrahedral** – The mesh size was changed to 1mm. This slightly improved the results and reduced the patchy contour on the foot (see red circle Figure 105).

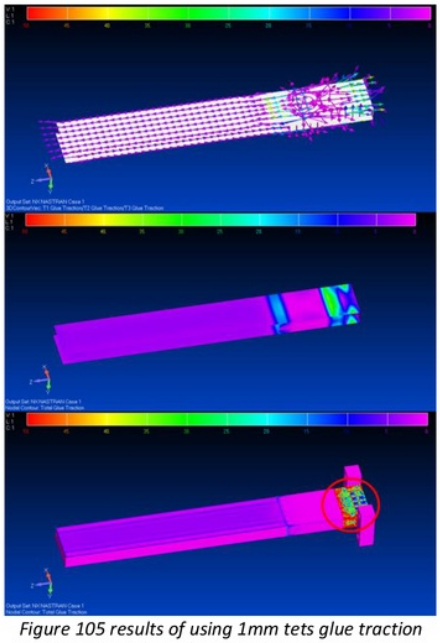


Figure 105 results of using 1mm tets glue traction

10.2.3 Outcome from study

The study found that to improve the glue traction results the core and foot meshes should be changed in size. The foot and core should have a 1mm mesh, but for foam core opting for a 2mm mesh would save on model solving time, as the study showed between 1 and 2mm size has a minimal effect on the result.

Testing the blade model with the new mesh size resulted in a significant improvement on the results. Figure 106 shows the composite mesh with glue traction contour. It can be seen the values are low and the transition is smooth (not patchy).

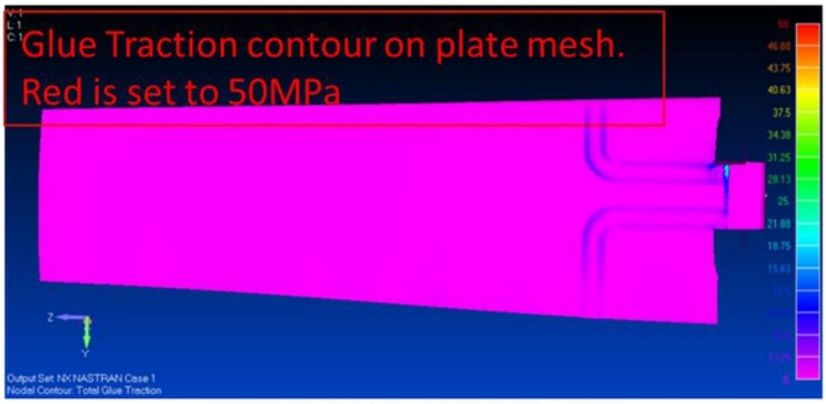


Figure 106 results of using new settings from study

The contour arrows are in similar directions and have minimal sudden changes (see Figure 107). The foam core had the same positive result (see figure 108).

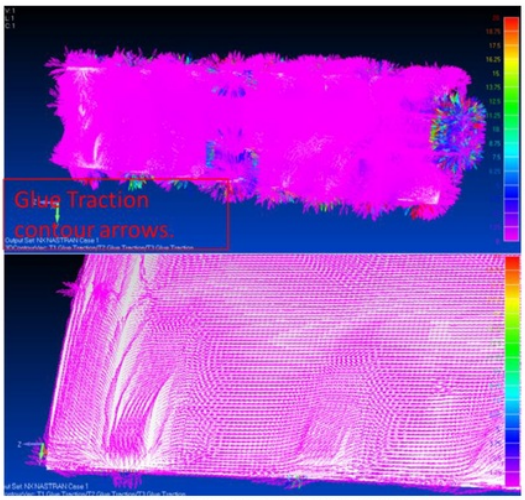


Figure 107 results of using new settings from study contour arrows

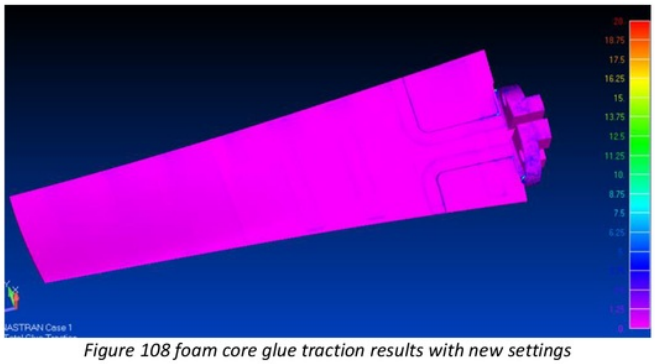


Figure 108 foam core glue traction results with new settings

The new mesh size improved the foot but there was still patchiness across the foot surface (see red circle Figure 109). The mesh size could not be reduced in an attempt to improve the results as it was on the upper limit of the processing power, already at 1mm. The foot was set to glue contacts for developing the composite laminate.

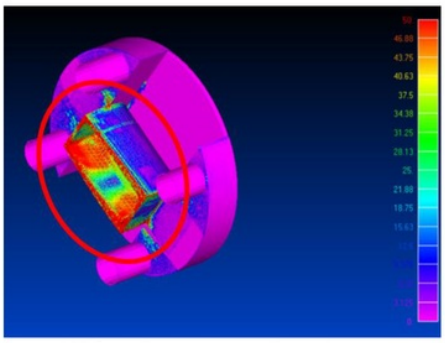


Figure 109 foot glue traction results with new settings

The new approach with the glue contacts increased the amount of solving time needed. To try and reduce the time it was attempted to bias the mesh surfaces of the foot and core, but this would not mesh correctly.

11. FINISHED DESIGN & FEA RESULTS

The finished blade design was the product of several design iterations. The bill of materials used in the final blade design are listed in **Appendix G**.

11.1 Blade Design Overview

11.1.1 Foot design

A similar foot design to the original is adopted but modified with a new round section where the 0° UD plies wrap around (see Figure 110). The section was changed in an attempt to make it easier to laminate the composite around the foot during manufacturing and reduce some of the weight.

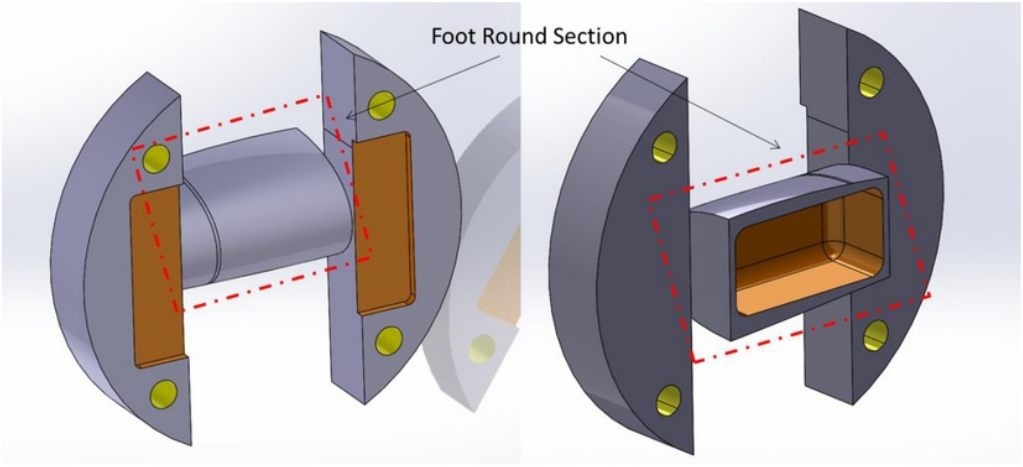


Figure 110 final foot design

In addition, the pocket in the foot for the foam core and back plate were updated to accommodate the new round section (see Figure 111).

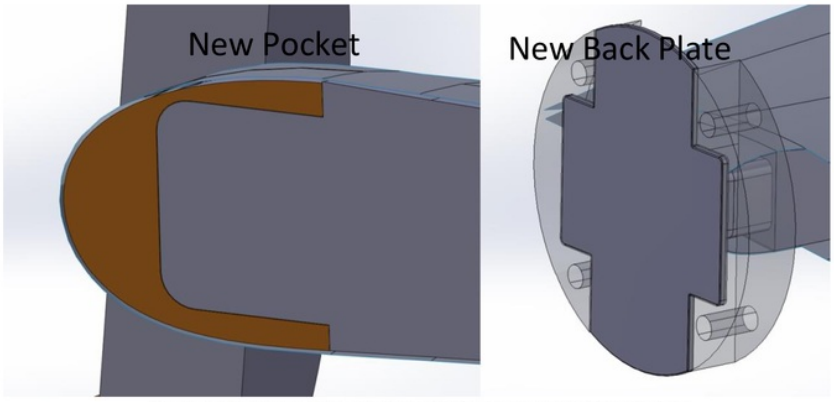


Figure 111 main core interacting with foot and updated back plate

The initial FEA results of the updated foot identified a concentration of high stress in the corners where the round section attaches to the 4 bolts (see Figure 112), greater than the target of 50% yield but less than 100%.

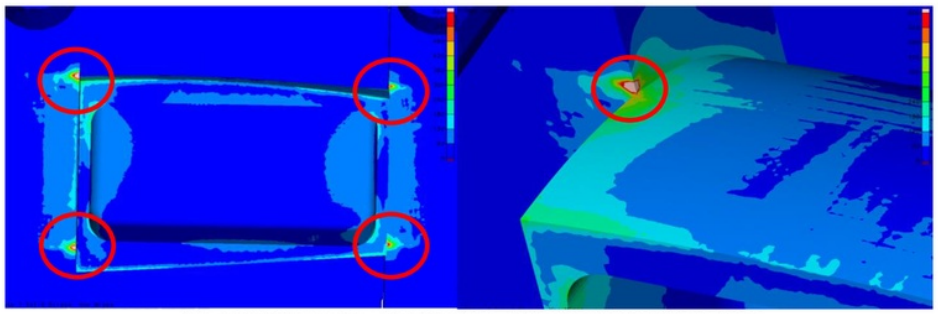


Figure 112 FEA results with of the foot without modes Von Mises stress

To address this, an iteration of adding gussets and fillets were incorporated into the design to disperse the load (see Figure 113).

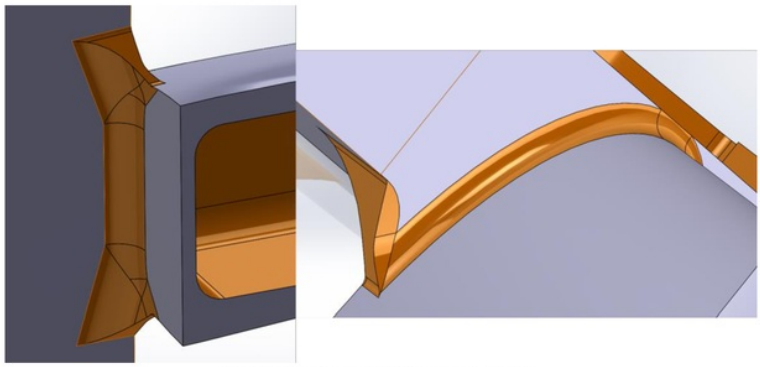


Figure 113 foot with fillets and gussets

The gusset and fillets sizes where taken to the biggest without intruding into composite bonding area of the foot. However, the biggest size could only reduce the stress down to 748MPa (see Figure 114), a 148MPa off the target of 600MPa (half the material yield). Increasing the gusset size any more intrudes into the composite layup and affects the stiffness performance of the blade. The 748MPa would have to suffice as the creep effect would be minimal.

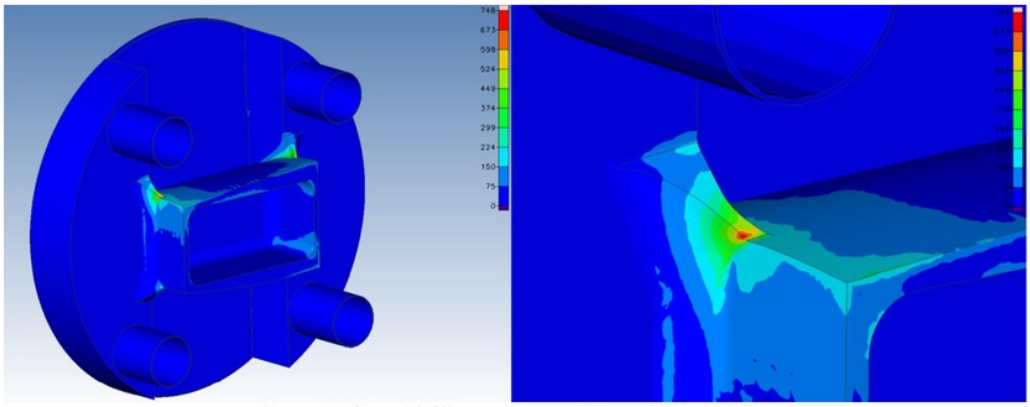


Figure 114 foot with fillets and gussets FEA results Von Mises

A significant issue with the final design was the total blade mass of 23.93Kg was more than the 20.1Kg target. Figure 115 are the FEA results of the back of the foot where it was low in stress and therefore an obvious region to reduce mass.

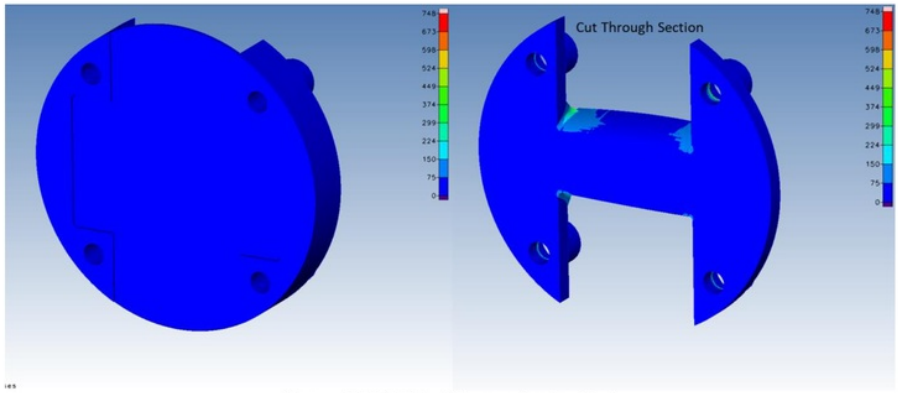


Figure 115 FEA Von Mises on back of foot

The low stress regions of the foot were pocketed out to bring the mass down (see Figure 116).

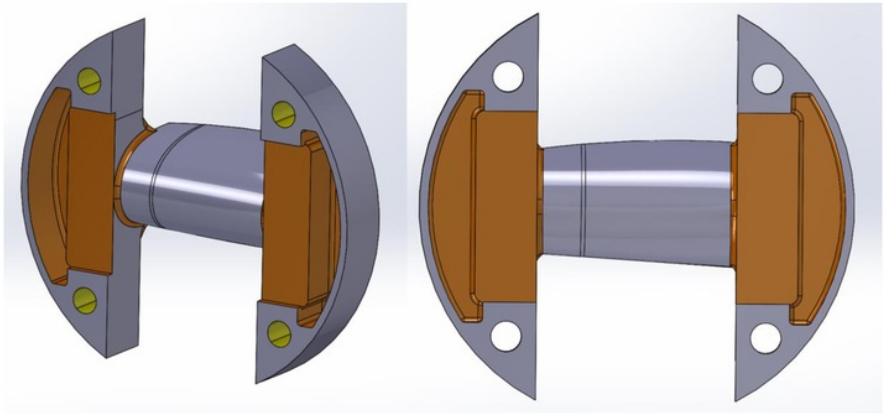


Figure 116 foot with cut out to reduce mass

Running the FEA again with the pocketed-out back section of the foot found the blade total mass reduced to 20.79Kg without increasing the stress on the foot (see Figure 117). The 20.79Kg could be adjusted down to 20.1Kg with the back plate after manufacturing.

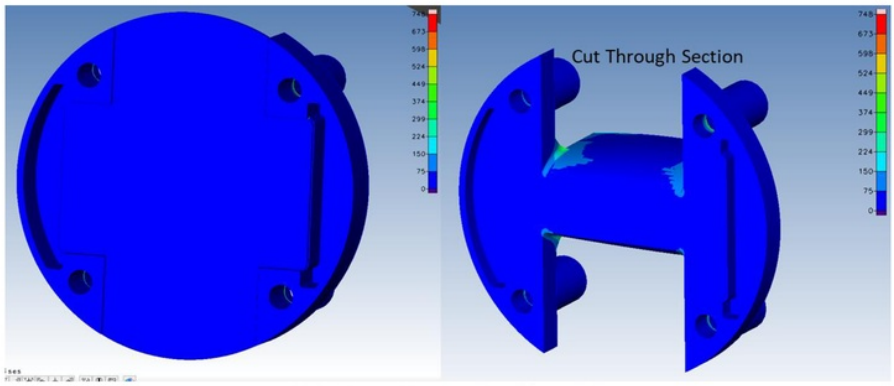


Figure 117 FEA Von Mises results of foot with cut out

11.1.2 Shroud area design and foam core

The shroud area design carried on with the silicon parts and the same amount of core parts. The main foam core also comprised of 3 parts.

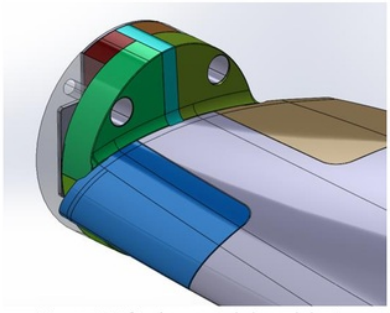


Figure 118 final core and shroud design

11.2 FEA Stiffness Results Of Final Design

Figure 119 is the final laminate layup and Figure 120 is the corresponding sections for the laminate (in **Appendix J** is another diagram of the final blade layup). The final layup included a 90° ply to account for any transverse loading not being accounted for in the blade design.

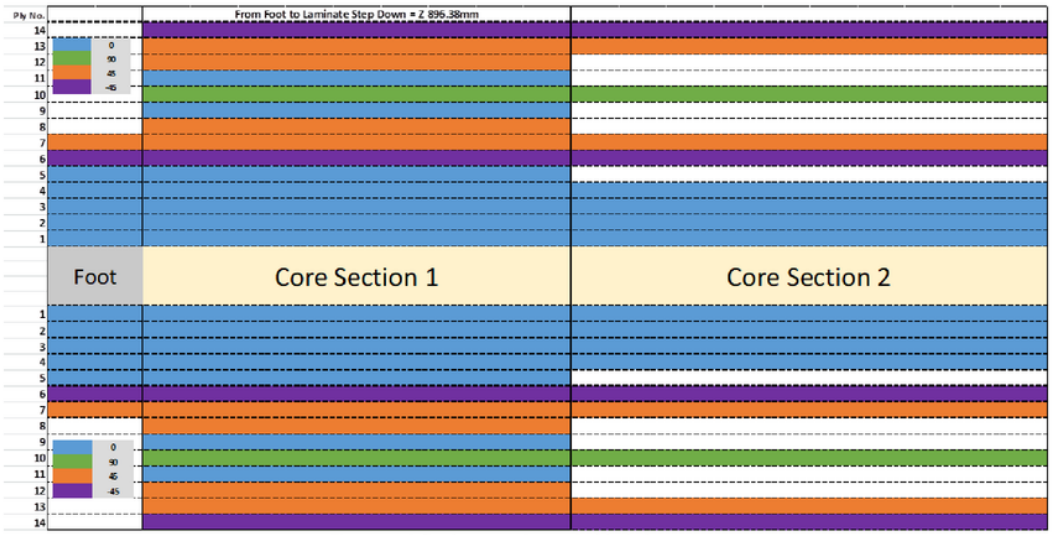


Figure 119 final composite main blade layup

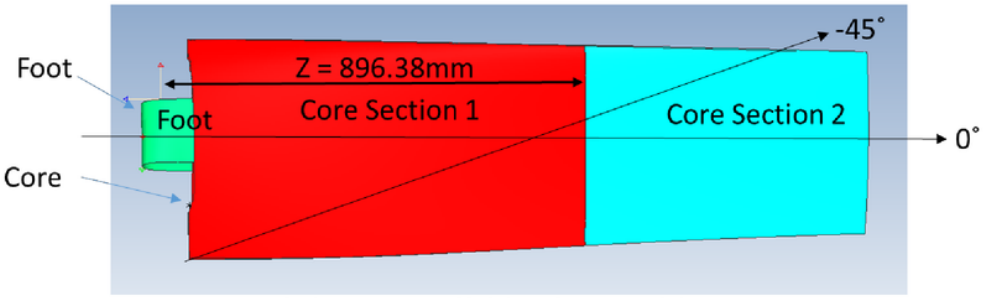


Figure 120 final composite main blade layup locations and ply orientation

Figure 121 was the first spar layup which was changed to use woven material on the ±45 plies to make it easier for manufacturing.

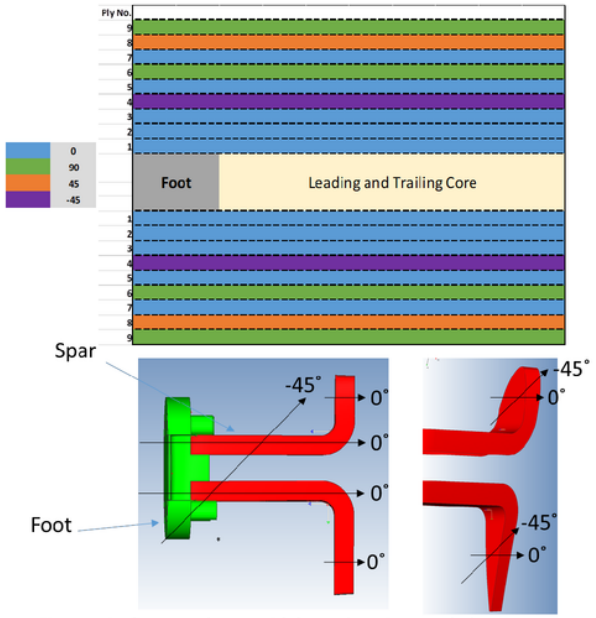


Figure 121 first spar layup with layup locations and ply orientation

Figure 122 is the spar layup with woven material and Figure 123 is the corresponding ply orientation. Some 0° UD plies had to be left in the laminate to keep the correct stiffness within the blade.

Ply No.	
9	Woven 45
8	Woven -45
7	Woven 0
6	UD 0
5	UD 0
4	UD 0
3	Woven 0
2	Woven -45
1	Woven 45
	Foot / Leading and Trailing Core
1	Woven 45
2	Woven -45
3	Woven 0
4	UD 0
5	UD 0
6	UD 0
7	Woven 0
8	Woven -45
9	Woven 45

Figure 122 spar layup including woven materials

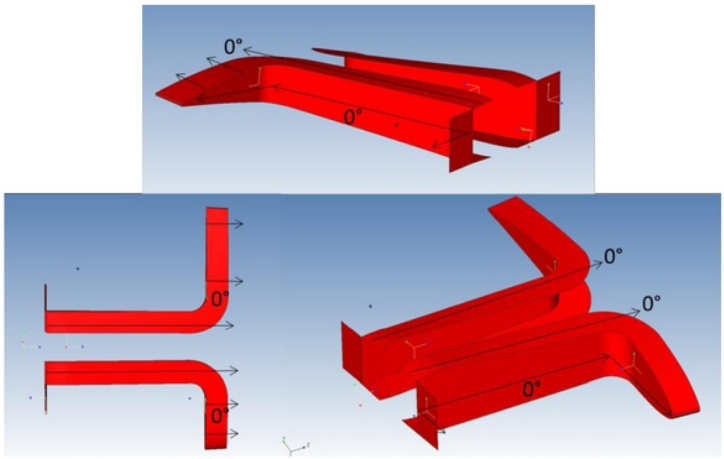


Figure 123 spar layup including woven ply locations and ply orientation

Figure 124 is the total ply thickness across the blade.

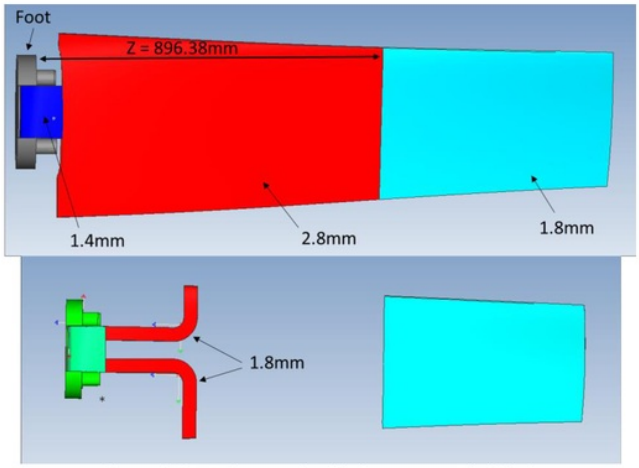


Figure 124 total composite thickness across the blade

11.2.1 Blade stiffness

Figure 125 is the magnitude displacement of the blade under max stiffness testing load. The testing found a max value of 40.542mm compared to the FEA of 39.4mm making a difference of 2.81%.

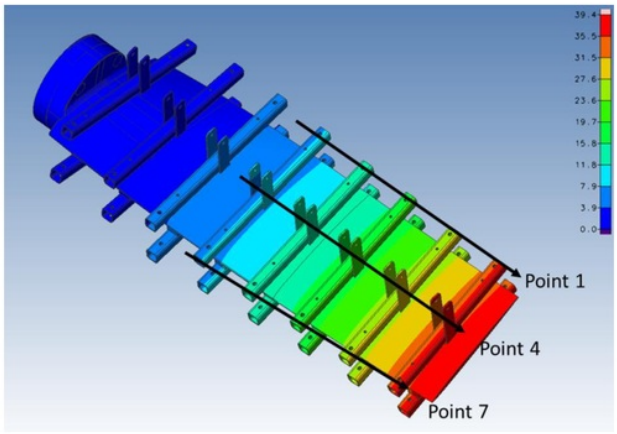
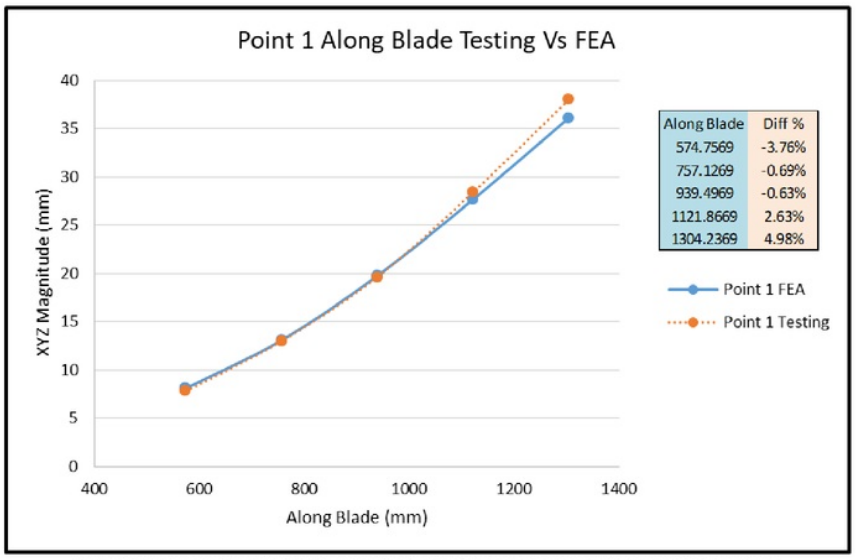
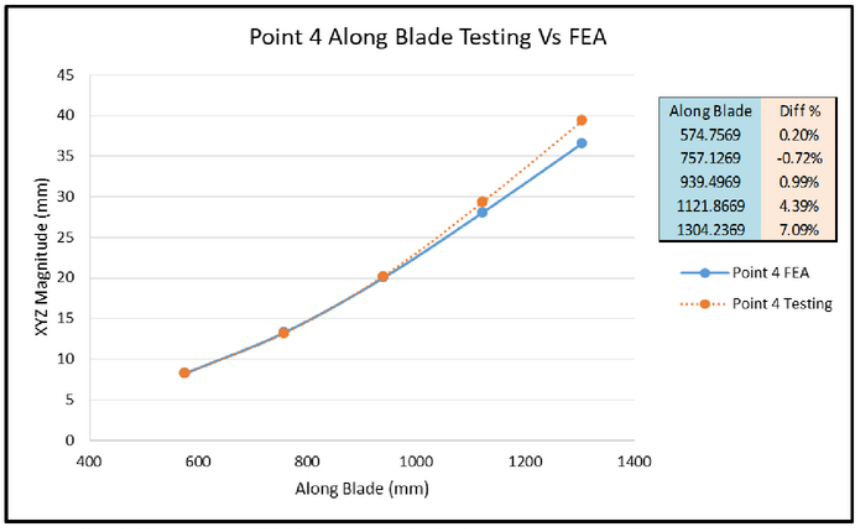


Figure 125 blade deflection under stiffness rig load

Points 1, 4 and 7 in Figure 125 are the constraint points of the optimisations. Graphs 17, 18 and 19 are comparing the FEA constraint point's displacement against the testing data.

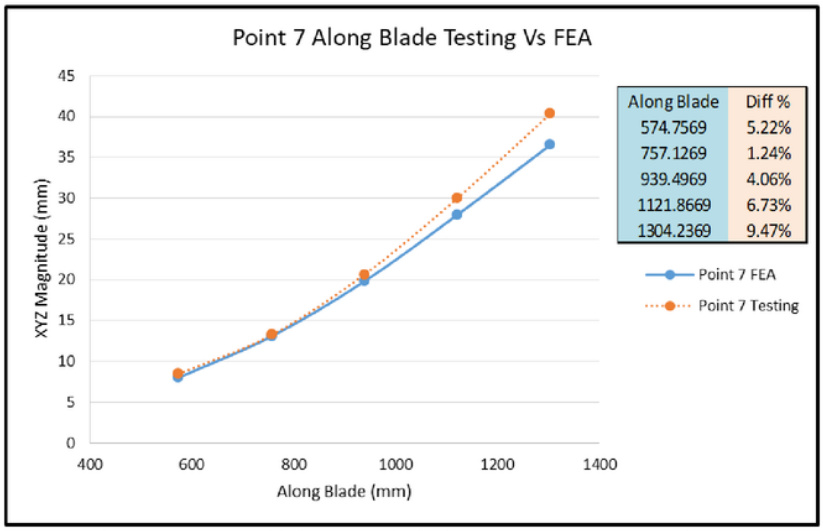


Graph 17 comparing FEA blade magnitude displacement against testing results point 1



Along Blade	Diff %
574.7569	0.20%
757.1269	-0.72%
939.4969	0.99%
1121.8669	4.39%
1304.2369	7.09%

Graph 18 comparing FEA blade magnitude displacement against testing results point 4



Along Blade	Diff %
574.7569	5.22%
757.1269	1.24%
939.4969	4.06%
1121.8669	6.73%
1304.2369	9.47%

Graph 19 comparing FEA blade magnitude displacement against testing results point 7

The new blade design does not exactly match the current blade stiffness, the difference being 9.47%. The results could not be greatly improved without using asymmetrical layup or by changing the ply sections. In theory, using a different UD material may improve the results with current design. However, this point of the project had reached the deadline for manufacturing *Mercedes* first blade prototype. The difference between the results was not thought to impact significantly on the performance as the blade design was over-stiff. Following a review meeting with *Lentus* discussing this result, the decision was made to proceed with the layup to meet deadlines. This meant a design review meeting would need to take place with *Mercedes* to discuss the difference between the new and old blade.

11.2.2 Composite stress

Figures 126 and 127 are showing the FEA results of highest stressed plies of each orientation for major and minor principle stress. When comparing the final results against the first blade design there was a similar trend of the stress concentration points remaining, with little improvement. This could imply the spars are not having the required effect, however, putting it into context, the first design was only tested up to 50Kg and this final design has over 500Kg of load with the overall stress relatively low.

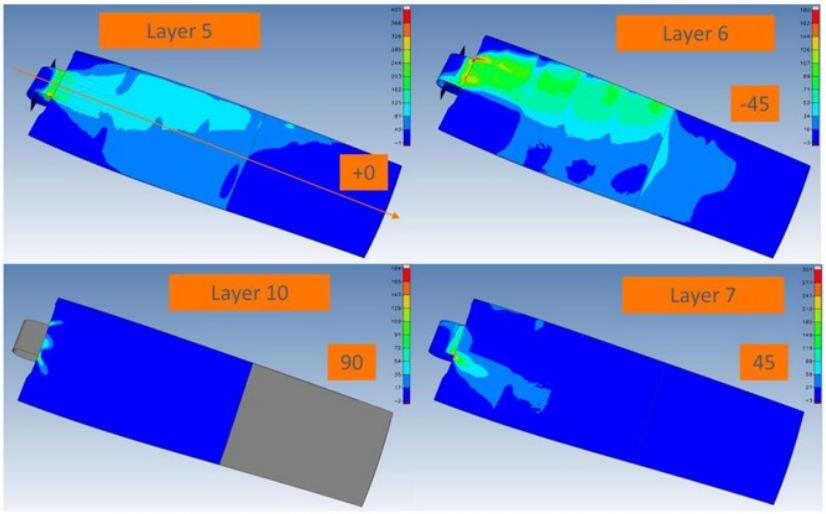


Figure 126 worst stressed plies under stiffness rig load major principle stress

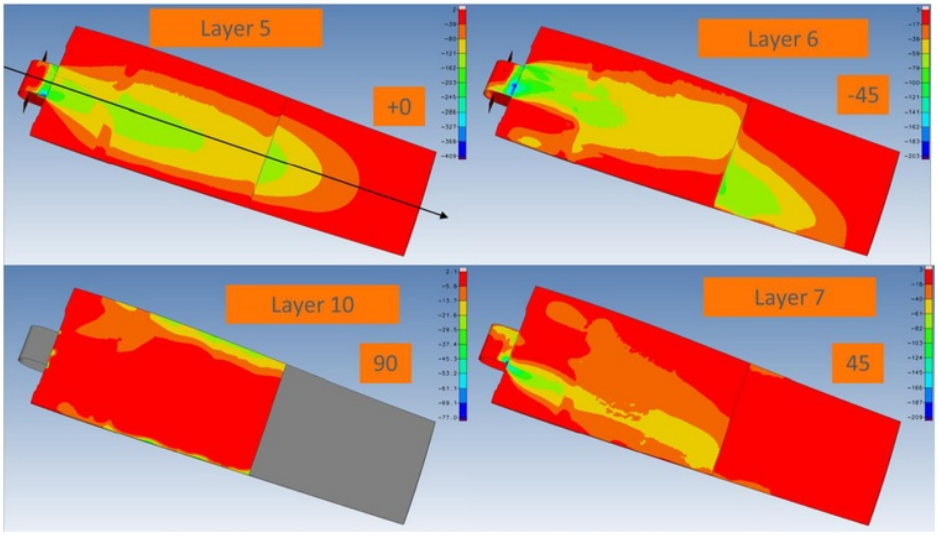


Figure 127 worst stressed plies under stiffness rig load minor principle stress

11.2.3 Composite failure index

The failure index is low with the worst point being 0.35. The index results show how there are now two stress concentration points (see Figure 128 red circles), one being from the

sudden change in composite geometry and the other from the sudden change in core stiffness (the composite going from the steel foot to the foam core).

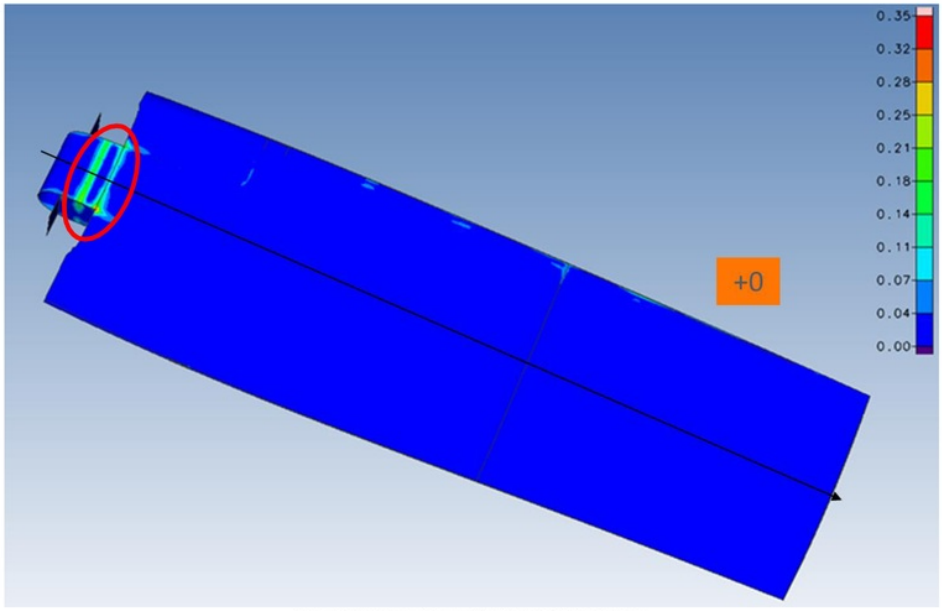


Figure 128 maximum Tsai-Wu failure index

11.2.4 Material parameter study

With the layup defined for blade stiffness, the next step was to check how changing the transverse direction and shear material properties would affect the results. Two different sets of material properties were tested; a low end set (unknown properties set 50% lower) and a high end set (unknown properties set 100% higher). Figure 129 shows those properties tested together with the normal properties.

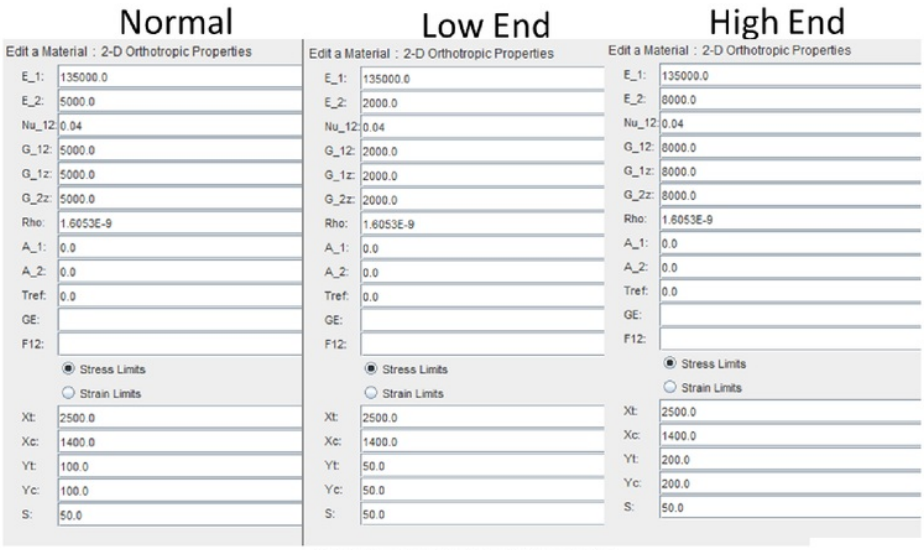


Figure 129 material properties tested

For the results for the blade displacement, there was only a change of 3% (see figure 130).

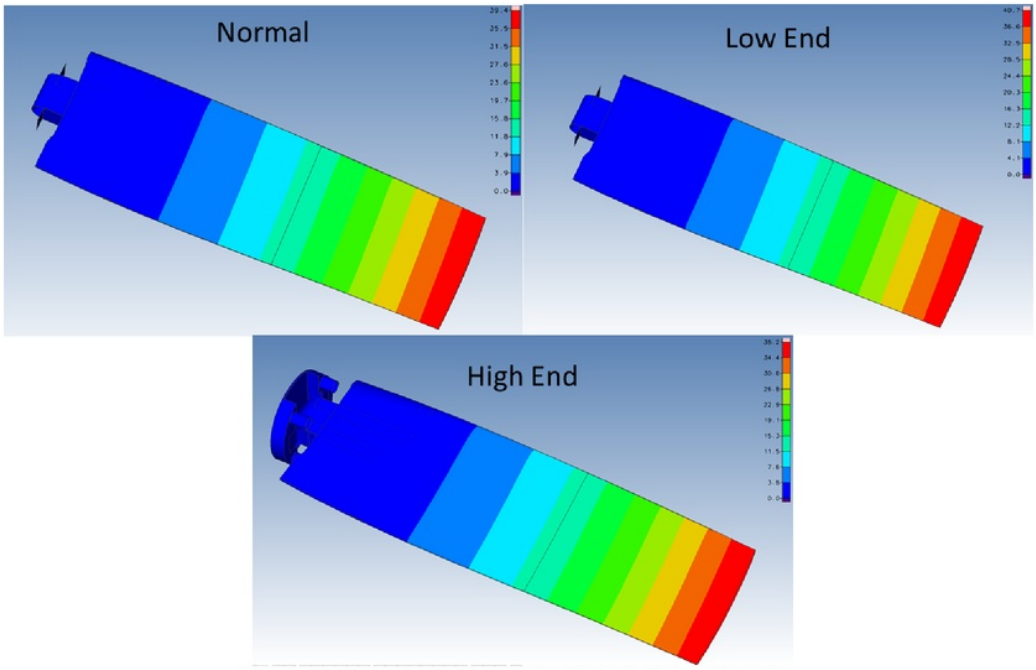


Figure 130 different material properties blade displacement results

The failure index results showed the same distribution across the blade (see figure 131), with the lower end properties only having a difference of 5%. However, the high end had a difference of 30%, and this was probably due to increasing transverse young's modulus which led to 90° and ±45° absorbing more of the load because of their higher stiffness.

Graeme Hyson concluded this was the likely reason for the index increase (Hyson, 2018). The material is very unlikely to have the high end properties as the normal properties used were stated by the manufacturer.

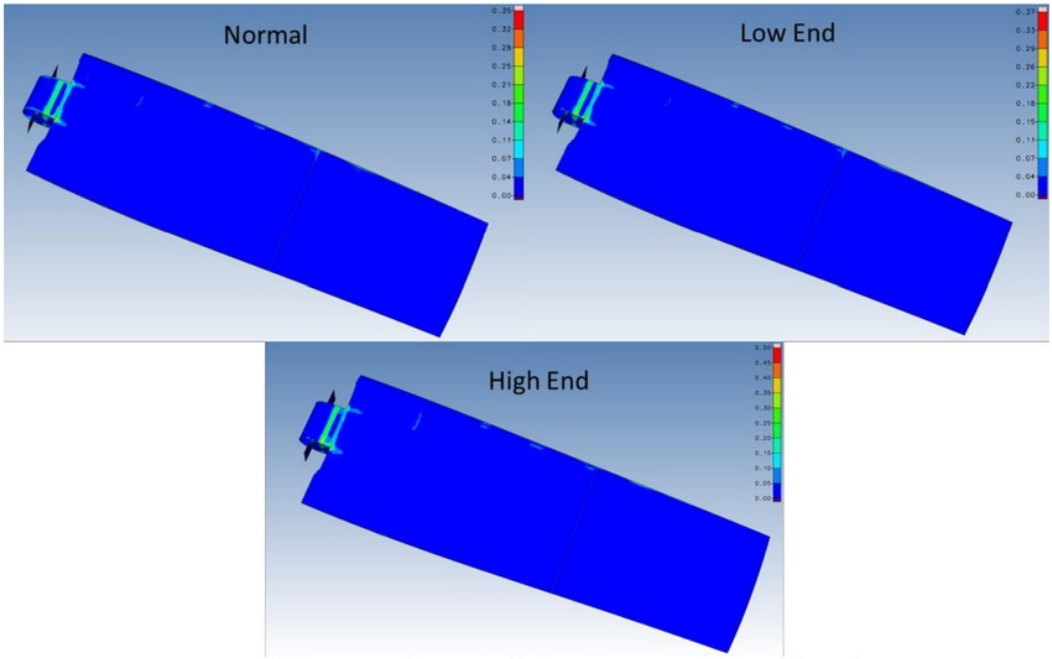


Figure 131 different material properties blade maximum Tsai-Wu failure index results

Overall the study showed even with extensive changes to the material properties, the composite layup is not sensitive to the changes.

11.3 FEA Stiffness & Centrifugal Load Results Of Final Design

With the defined laminate the centrifugal and stiffness loads were both applied to the model.

11.3.1 Composite stress

The highest stressed plies of each orientation resisting major and minor principle stress followed the same trend as with only having bending load applied. The blade had the same distribution of stress as previously, but to a greater extent (sees Figure 132 and 133).

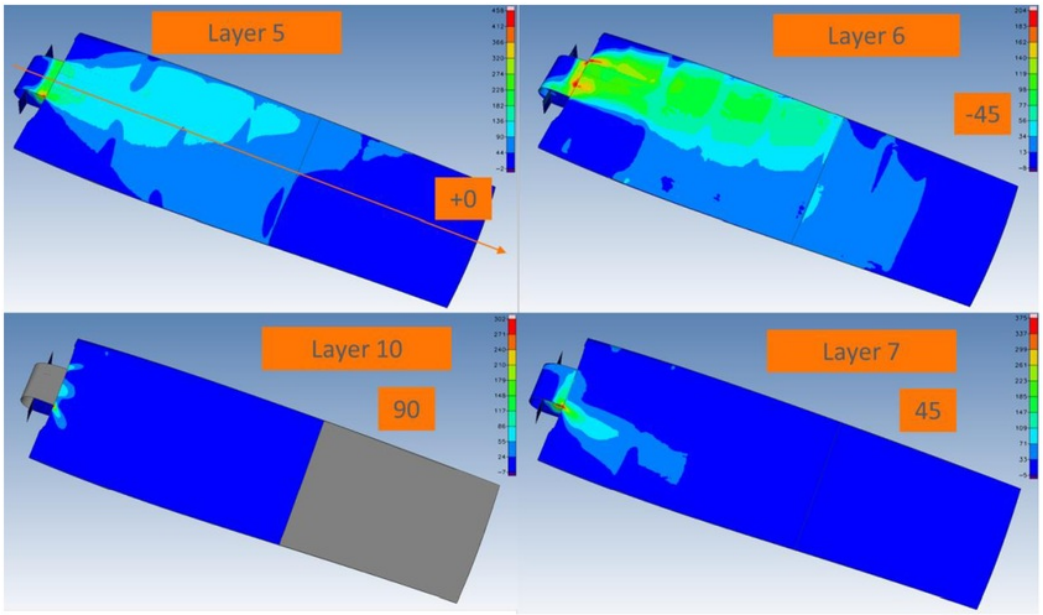


Figure 132 worst stressed plies under stiffness rig and centrifugal load major principle stress

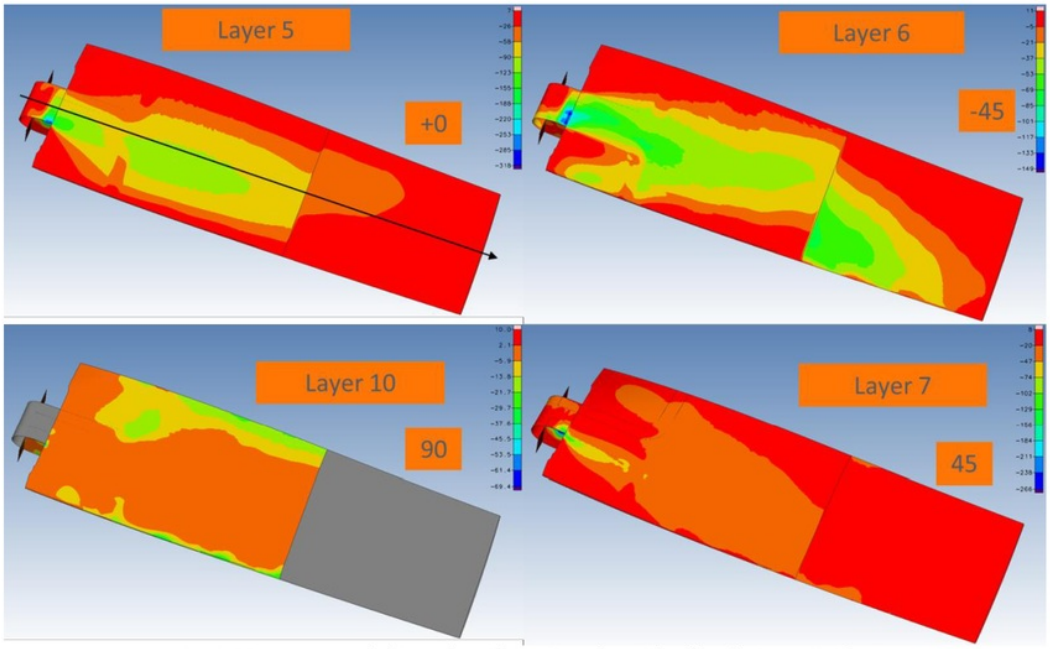


Figure 133 worst stressed plies under stiffness rig and centrifugal load minor principle stress

11.3.2 Composite failure index

The added load increased the failure index up to 0.57 but maintained the same distribution (see Figure 134).

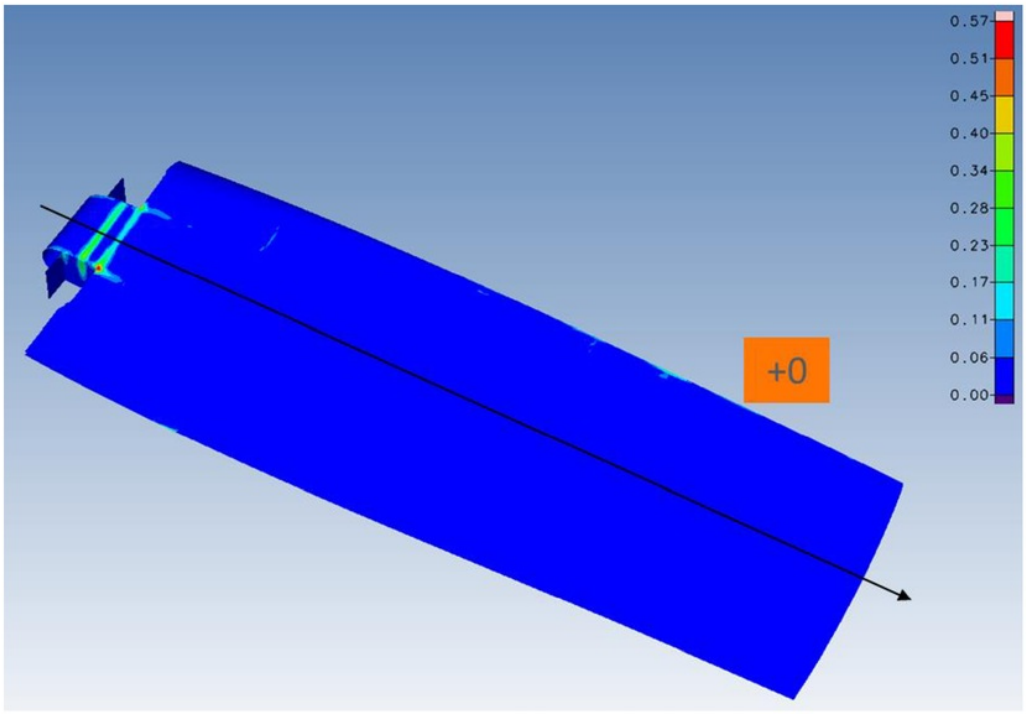


Figure 134 maximum Tsai-Wu failure index from both loads

11.3.3 Composite strain

The highest strain in the blade occurred in ply 1 at the stress concentration points (see Figure 135). The value of the maximum strain was 4700 microstrain which was in excess of the design target of 3000. However, this was only in one isolated spot. Reviewing the results with Nolan Richmond, he did not consider the value of 4700 being an issue as it was in one small area (Richmond, 2018). This aspect of the design was included for highlighting with the client *Mercedes*.

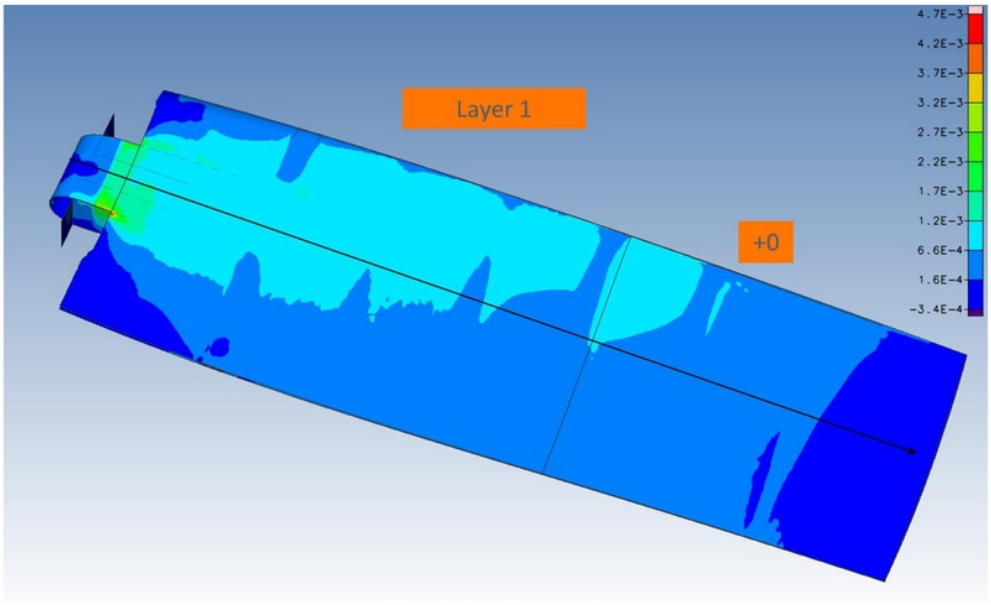


Figure 135 maximum strain

11.3.4 Other composite part results

The composite spars had a relatively low stress and failure index with the exception of high stress where the core changes from the steel to the foam core (see Figure 136).

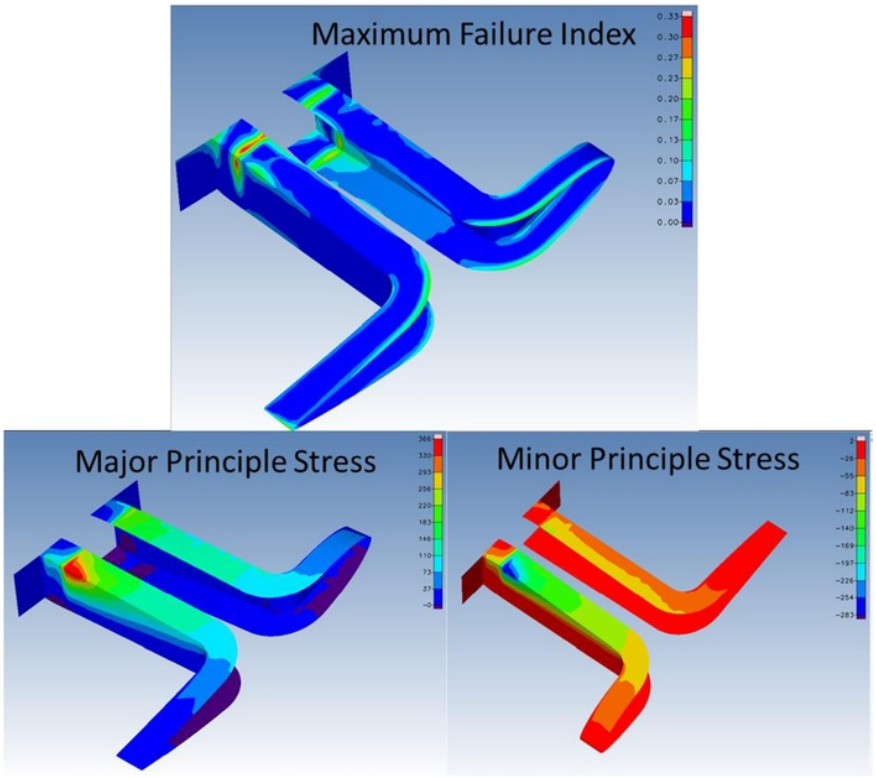


Figure 136 spar composite FEA results

The composite layup for the shroud area consisted of 4 plies. The FEA results showed extremely low stresses in that area which was expected in the design since the steel foot withstands the entire load. In Figure 137 the colour contours are patchy, indicating the glue contacts used to connect the mesh in that region are not quite in sync. However, with stress being so low it was not thought to have a significant enough influence on the results to induce the material to fail if amended.

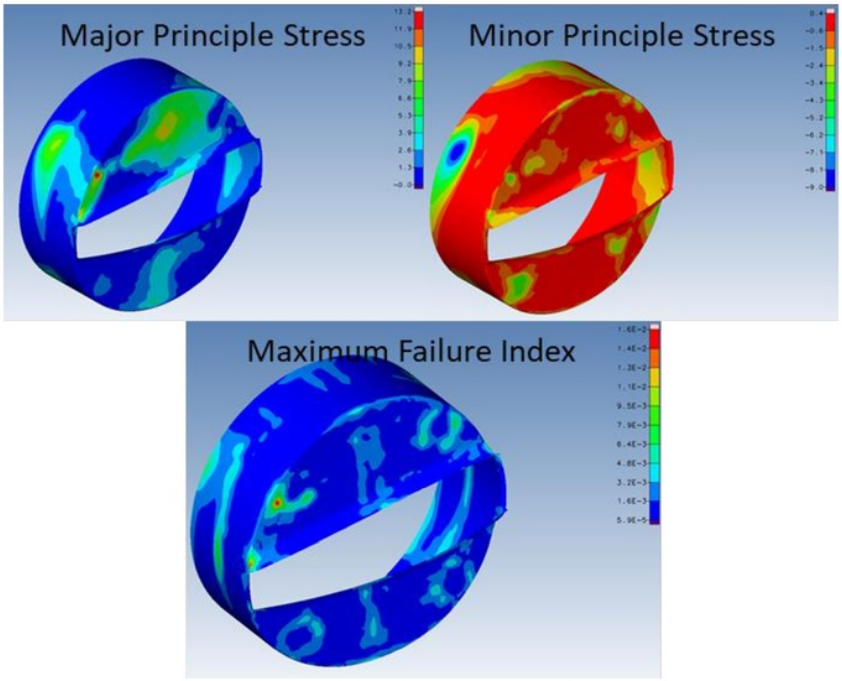


Figure 137 shroud composite FEA results

11.3.5 Foot stress

As previously explained the foot has the highest stresses in the gusset attachment (see Figure 138).

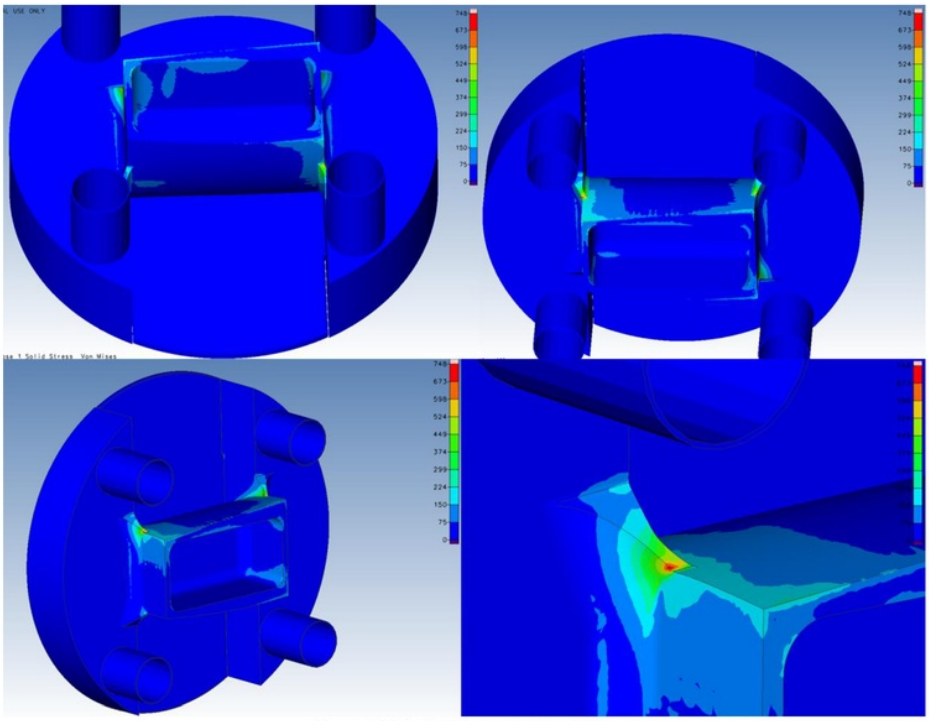


Figure 138 foot FEA results Von Mises

11.3.6 Core stress

The majority of the core is subject to low stress, as expected for the sandwich material (see Figure 139). However, some points on the leading and trailing core are exceeding the material strength of *Rohacell 71* (see red circles). To overcome this problem, the leading and trailing core use *Rohacell 101* as this has a higher strength than 71.

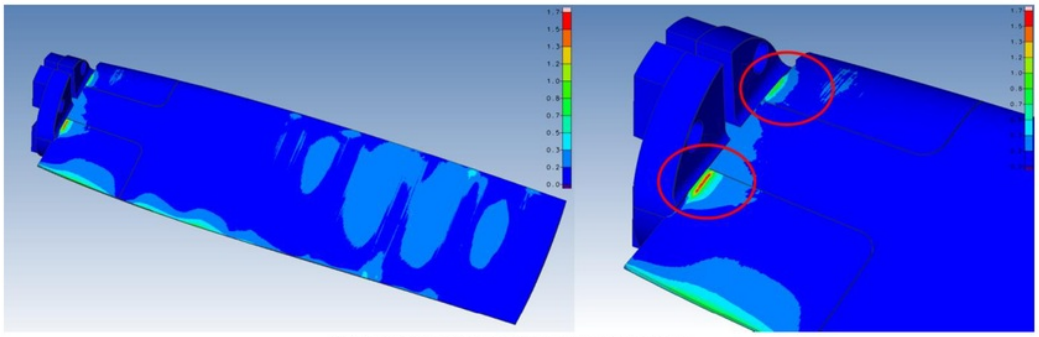


Figure 139 foam core FEA results Von Mises

11.3.7 Other solid parts stress

The silicone parts and the steel sleeves were both within their material properties (Figure 140 and 141).

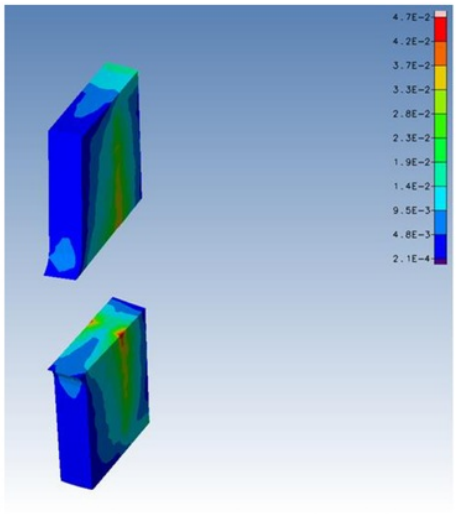


Figure 140 silicone parts FEA results Von Mises

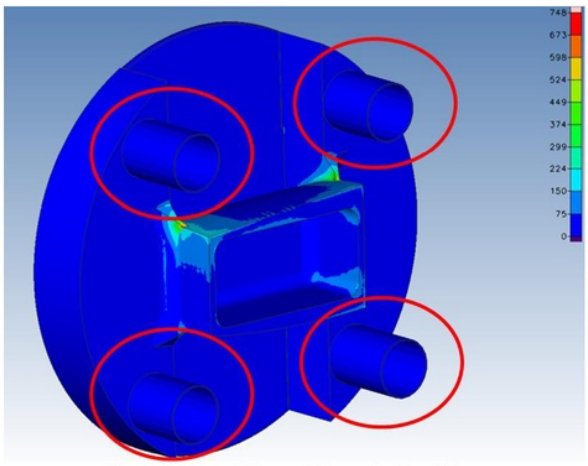


Figure 141 steel sleeves FEA results Von Mises

11.3.8 FEA natural frequency results

Carrying out the FEA study on the design frequencies found the first mode matched up perfectly with the LDV and F&S results of the current blade (see Figure 142). Mode shape was bending and had a frequency of 41.12Hz. The same for the second mode having a similar mode shape and frequency (see Figure 143).

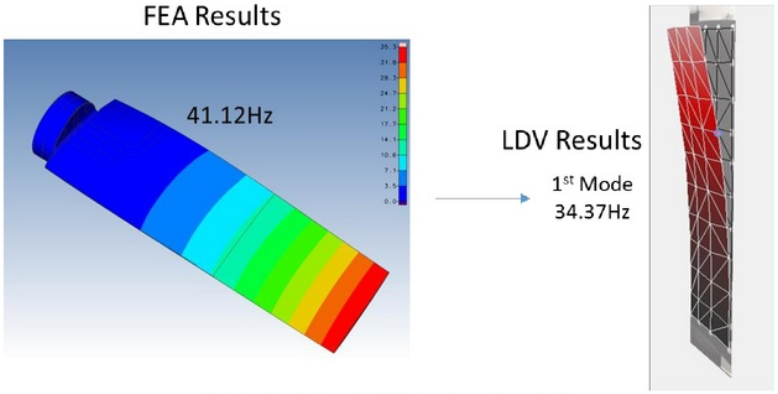


Figure 142 final design FEA results of 1st mode

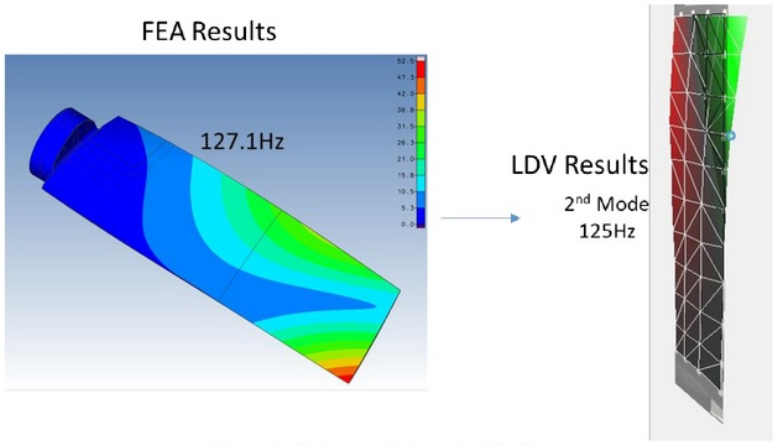


Figure 143 final design FEA results of 2nd mode

The 3rd and 4th modes were different from the current blade (see Figures 144 and 145).

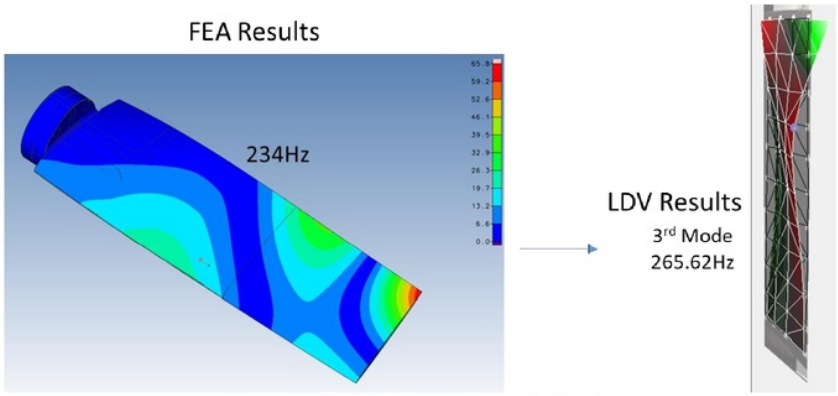


Figure 144 final design FEA results of 3rd mode

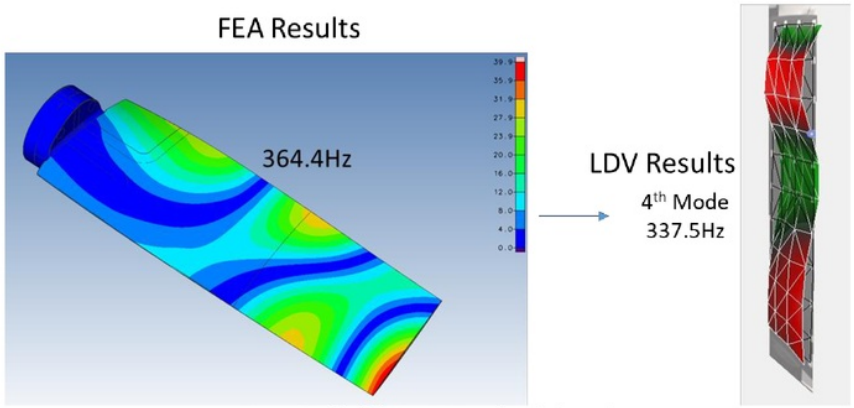


Figure 145 final design FEA results of 4th mode

The results indicate that the new blade is close to matching the stiffness of the original with the 1st and 2nd modes being close. However, the 3rd and 4th's difference in value could be due to:

- Different mass distribution between the blades
- Use of different materials

Even with the 3rd and 4th being different, the favourable results of the 1st and 2nd's natural frequency is a good indication that the new blade design is close to being the exact stiffness of the original. The design target was to replicate the 1st frequency and mode shape close to the original which has been achieved from the results.

11.3.9 Bond stress between laminate and core/foot

All the results of the final blade design up until this point have been positive. One of the last aspects to check was the bond stress (glue traction) between the laminate and the cores. Upon first inspection across the blade laminate and foam core, the glue traction was below 6MPa (see Figure 146). In the area of where the laminate attaches to the steel foot, the stress was around 40MPa, which at the time was thought to be acceptable as the E772 was rated to 67MPa (TenCate, 2018). However, after a penultimate design review meeting with *Lentus*, Nolan Richmond and Graeme Hyson identified from their experience that the 40MPa was too high and the laminate would de-bond from the foot. Graeme Hyson advised that some of the material classification properties tested and issued by material manufacturer are done in an artificial environment and not in realistic applications. They recommended the stress should be below 20MPa, which was only a problem for the steel foot connection (Lentus Composites, 2019) (Hyson, 2018) (Richmond, 2018).

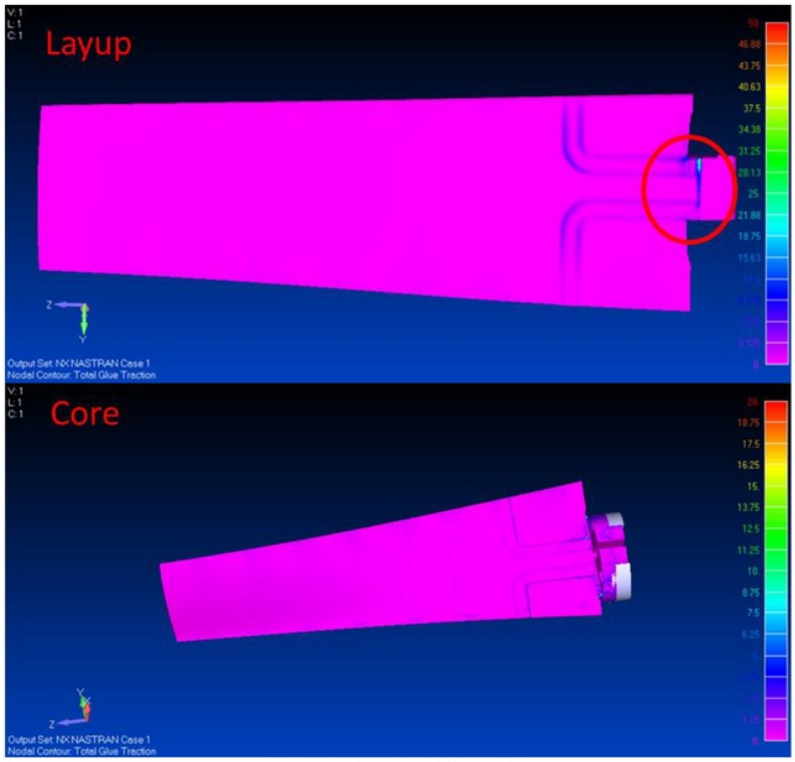


Figure 146 glue traction results

To check that the 40MPa was not an artificial stress caused by the FEA simulation, the glue contacts on blade was run again with spring elements connecting the composite mesh to the foot resulting in a similar result with the stress being at 42MPa (see figure 147).

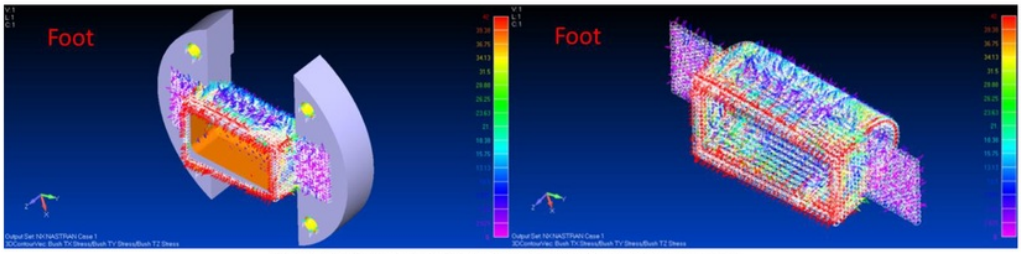


Figure 147 glue traction on the foot using spring elements

Carrying out further investigation into the contributing factors influencing the maximum failure index found that the majority of the maximum index values originate from the interlaminar stresses. In Figure 148 the red circles indicated the two spots where the index is high. Looking at the failure index of the compressive and tensile stress of ply 1 the two spots do not exist. The failure index of the interlaminar stresses' is identical to the maximum index meaning the high stress in the joint comes from the interlaminar stress. This in turn means the plies want to pull apart and de-bond from the foot.

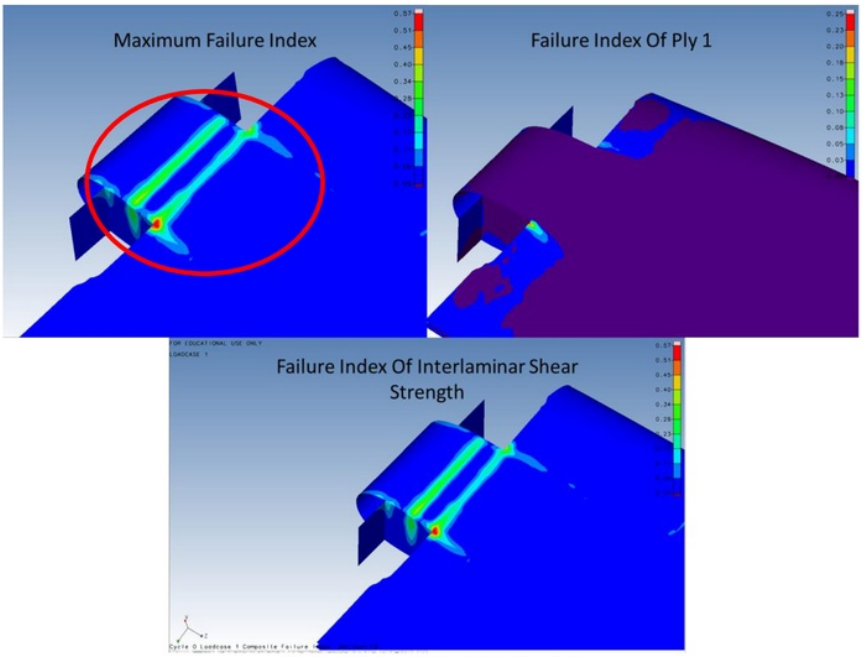


Figure 148 comparing failure index's

This can be said for the spar composite as well with the total index substantially coming from the interlaminar stress (see Figure 149) at the same point where the steel foot starts and ends.

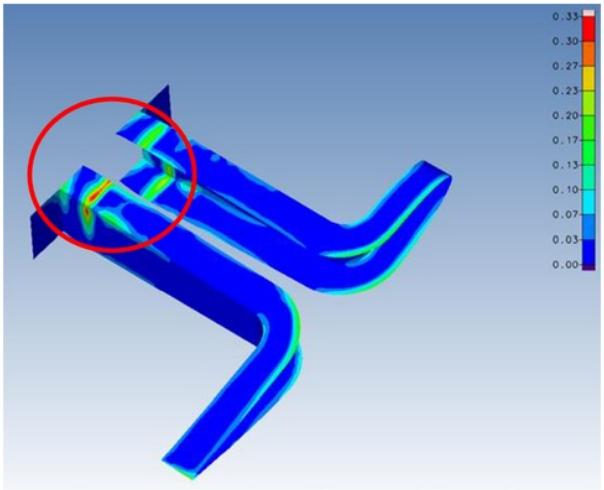


Figure 149 spar interlaminar shear strength failure index

The results show the composite tending to de-bond. This is typical of this type of joint. Graeme Hyson confers (Hyson, 2018).

11.3.10 Attempts to reduce the bond stress

Several improvements to the design were tried:

- **Adding in zed ply** – Transferring the peeling load onto fibres under tension through composite attached to the foot pocket and then to the surface of the main laminate (see Figure 150).

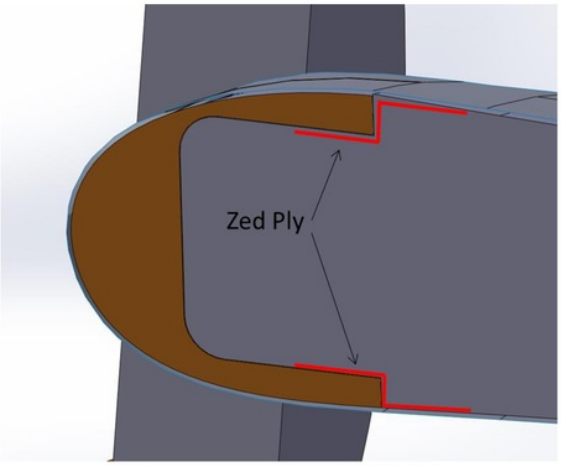


Figure 150 the zed ply on the steel foot

Mesh was modelled in-between the foot pocket and the main laminate to act as the zed plies. A layup of low and high stiffness was tried. However neither had a significant effect on the results. Figure 151 is the glue traction stress, which is still above 20MPa near the edges of the foot.

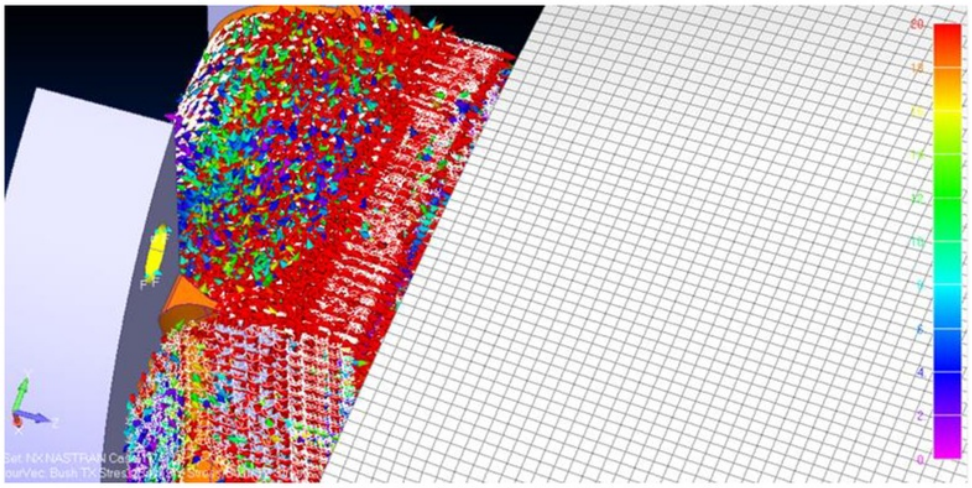


Figure 151 FEA results of adding in the zed plies glue traction

- **Wrapping 90° plies around foot** – The 90° plies are intended to warp around the joint of the steel foot in contact to the foam core. Figure 152 illustrates the function of the 90° plies which is intended to stop the main plies pulling away from the foot under bending load as the 90° fibres counteracts by going into tension.

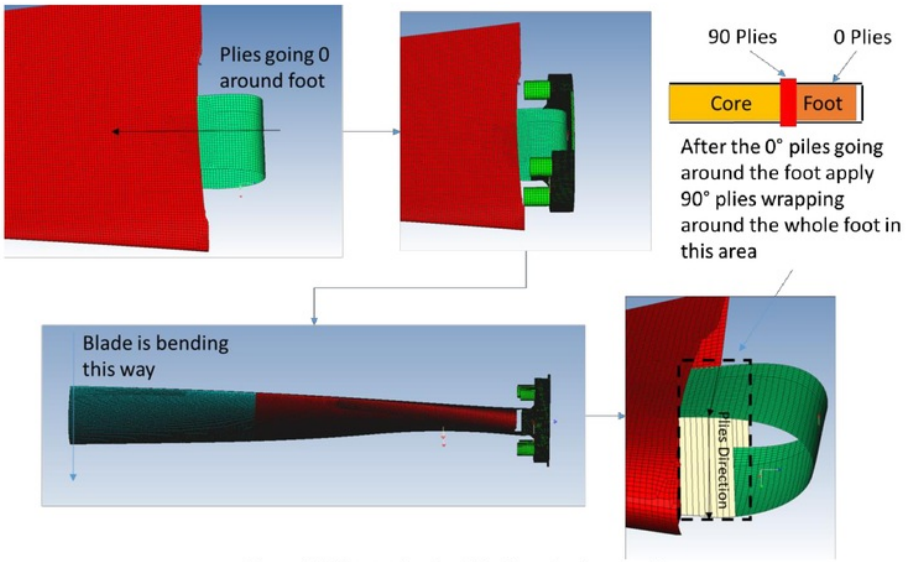


Figure 152 illustrating the 90° plies going into tension

However, this approach had no effect on the results even with increased composite material stiffness values for the 90° plies.

- **Tapering foot** – tapering the foot connection point with the foam core and change the stiffness gradually, rather than a sudden change. Figure 153 shows the results with and without taper. The taper did not have a beneficial effect, indicated by how the interlaminar shear strength failure index did not change significantly. Tapering the foot did cause the foot stress to increase from 748 to 962MPa.

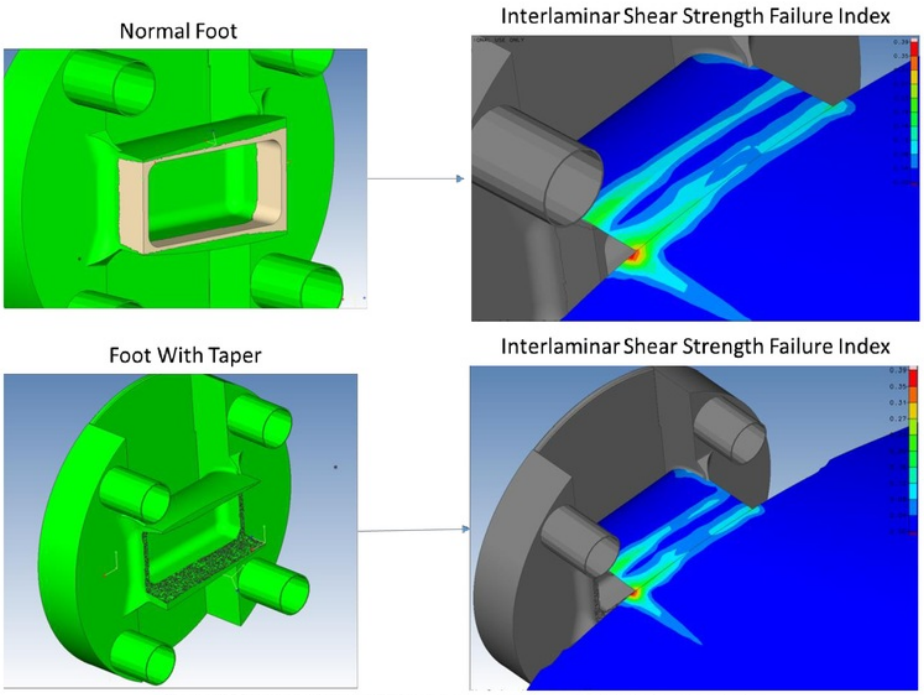


Figure 153 comparing the FEA results of the foot with and without a taper

- **Extending out the foot with taper** – Building on the tapering concept, extending the foot into the blade with an elongated taper (see Figure 154).

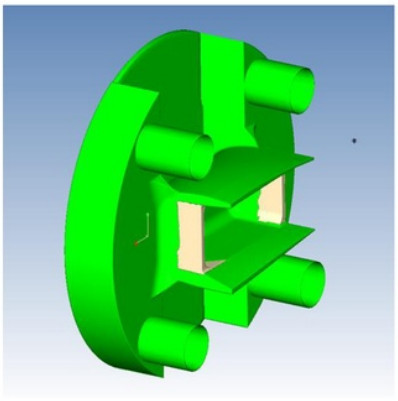


Figure 154 foot with extended foot taper

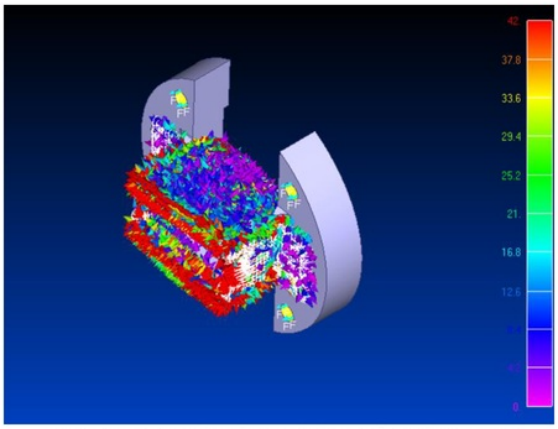


Figure 155 FEA results of extended taper foot glue traction

The extended foot did improve the results slightly, but still not below the acceptable level of 20MPa. Figure 155 shows the results. The high concentrated stress transfers to the edge of the foot.

Foot With Taper Normal Foot

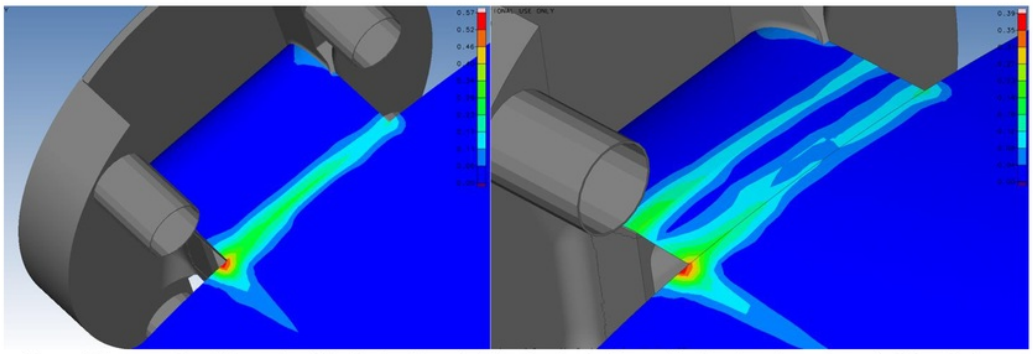


Figure 156 comparing FEA results of the foot with and without extended taper interlaminar shear strength failure index

The failure index of the extended taper has moved from one of the two previous spots where the index is high (see Figure 156), but still not assisting with stress reduction around the abrupt composite geometry change. The extended taper foot repeats the problem of increasing the foot stress (see Figure 157). In addition, extending the foot results in increasing the total blade mass which is undesirable.

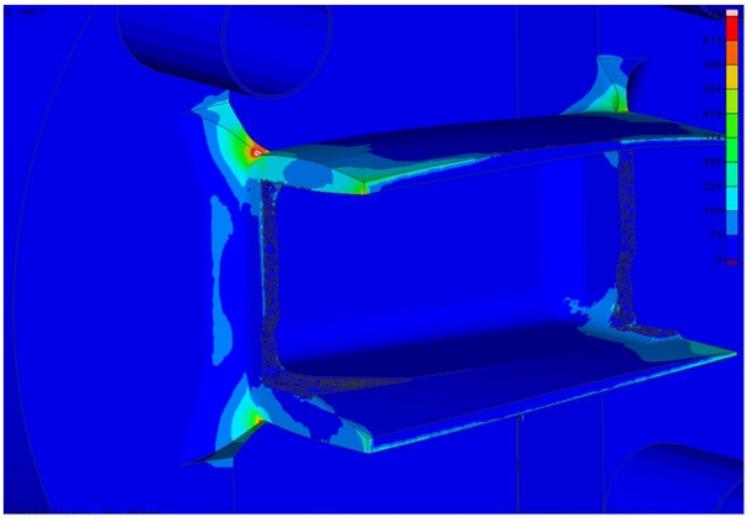


Figure 157 tapered foot Von Mises stress FEA results

- **Increasing composite stiffness at foot** – This approach was to divide up the composite sections near the foot and start with a similar stiffness as the foot itself. Then gradually reducing stiffness along the blade by dropping off the plies (see Figure 158). This again is attempting to smooth the sudden change in the stiffness over increased area.

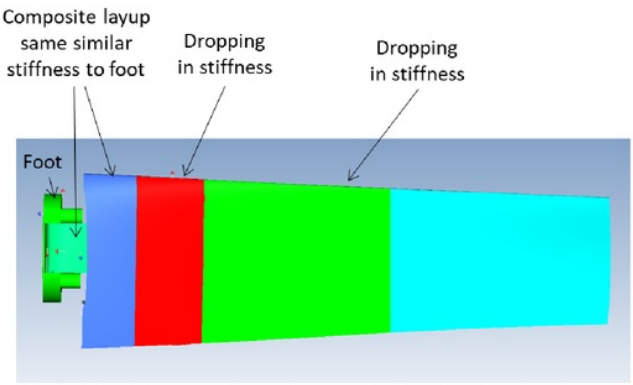


Figure 158 illustrating having stiffer composite section near the foot then dropping off along the blade span

The results are shown in Figure 159. Whilst this was not entirely successful, there was a slight improvement.

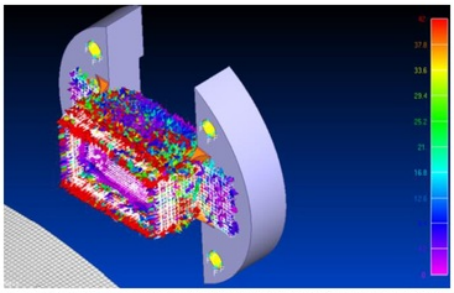


Figure 159 FEA results of extended taper foot glue traction

In summary, none of the methods of reconfiguring the joint design resulted in reducing the bonding stress to 20MPa. However, increasing the composite stiffness towards the foot, together with tapering, could result in the target improvement necessary if there was sufficient time remaining to develop the technique further. The adjustments to the design would have to be done with care so as not to inadvertently change the CoG Z beyond the design target and the total mass of the blade. Perhaps the composite spars could be re-looked at to help bring the bonding stress down.

Unfortunately, at this point of the project the deadline for finishing academic/investigative work was imminent, which meant further development on the new blade design would have to be curtailed. A review of the full design to date was conducted with *Lentus* and a plan formulated and agreed for adjusting the design to accommodate the bonding stresses, thereafter manufacturing the prototype. The author would focus on finishing academic elements to comply with University requirements whilst *Lentus* would adjust the design to resolve the last remaining issue.

11.4 Summary Of Finished Design

Table 11 below sets out the summary of the final design performance against the original design targets:

Table 11 final design performance against the design targets

No.	Target	Value	Pass ?	Acceptable ?	Why?/Notes
1	New Design To Match Current Blade Stiffness	Match the values from testing	No	Yes	The blade stiffness was only at worst 9% stiffer. The performance is to be discussed with *Mercedes* to reach an agreement.
2	The Design To Cope With Centrifugal Loading At 550RPM	Value to be calculated	Yes		Composite not failing under load, but safety factors to be discussed with *Mercedes*.
3	Total Blade Mass	20.1Kg	Yes		The total mass came out as 20.79Kg. Mass is over but can be controlled with back plate.
4	New Design To Match 1st Mode Frequency	Min 38Hz	Yes		
5	New Design To Match 1st Mode Shape	Bending Mode	Yes		
6	The CoG Z distance	*Z* To Be No More Than 359mm	Yes		The *Z* came out as 246mm. *Mercedes* are aware that because this value is not the exact same the blades will need to be changed in pairs.
7	Steel Foot Stress To Be Half Of Material Yield Point	Depending On Material	No	Yes	Not thought to have a major effect, but to be discussed with *Mercedes*.
8	Composite Strain	Be Below 3000 Microstrain	No	Yes	In one confined spot, to be discussed with *Mercedes*.

Table 11 does not include the unresolved issue of the bonding stress being too high against the target threshold. Apart from that, *Lentus* has confirmed the new blade design produced conforms to their satisfaction and confidence to deliver a prototype for testing to *Mercedes*, subject to their approval of errors highlighted in the body of this report.

11.4.1 Reserve factors

One set of criteria that has not yet been considered and quantified are the reserve factors (safety factors) of each part of the new blade design. Table 12 shows the reserve factors for major components in the design and Table 13 the reserve factors that have been used in terms of the loading used in the FEA analysis.

Table 12 blade parts safety factors

Blade Parts Reserve Factors						
Part	**Part Defining Value**	**Material**	**Material Limit**	**Highest Value on Part**	**Factor**	**Notes**
Main Composite	Tsai-Wu failure index	T700S E722	Value Of 1	0.57	1.75	
Composite Spars	Tsai-Wu failure index	T700S E722 & TR30S 3K 2X2 Twill E722	Value Of 1	0.33	3	
Shroud Composite	Tsai-Wu failure index	T700S E722 & TR30S 3K 2X2 Twill E722	Value Of 1	0.016	62.5	
Foot	Von Mises stress	15-5PH	1200MPa	748MPa	1.6	
Shroud Core	Von Mises stress	*Rohacell* IG-F 71	1.5MPa	0.2MPa	7.5	
Silicon Parts	Von Mises stress	*Alchemix* RTV240-C251	3.4MPa	0.047MPa	72.3	
Main Foam Core	Von Mises stress	*Rohacell* IG-F 71	1.5MPa	0.5MPa	3	
Leading and Trailing Foam Core	Von Mises stress	*Rohacell* IG-F 71	1.5MPa	1.7MPa	0.88	To be updated to IG-F101
Steel Sleeves	Von Mises stress	Stainless steel grade 304	205MPa	4.7MPa	43.6	
Back Plate	Von Mises stress	Stainless steel grade 304	205MPa	12.3MPa	16.6	

The factors in Table 13 are derived from the assumptions made during the design process. The following points are made about the factors:

- The blade was tested up to 5020N rather than the 4130N calculated. Also *Mercedes* restricted running the wind tunnel at 50m/s rather than the original operational target of 80m/s. If the facility exceeds 50m/s, this would mean as an estimate, the tunnel

runs at 343.75. Running 37.5% slower than maximum design means the factor has a further 37.5% (Miller, 2018).

- Again if it is assumed the tunnel only runs at 50m/s then the centrifugal load is lower.

Table 13 blade load reserve factors

Blade Loading Reserve Factors			
Load	**Running Load**	**Load Used**	**Factor**
Aerodynamic load	4130N	5020N	1.21
Assumed Aerodynamic Load At 50m/s wind speed	2581N	5020N	1.94
Centrifugal Load	50424N	129500N	2.56

As there is no information available on what are the right reserve factors for the new blade design, it is proposed to discuss the above factors with the client *Mercedes* and ascertain if they are acceptable.

12. CONCLUSIONS AND EVALUATION

This report has tracks the design process adopted to reverse engineer a composite wind tunnel fan blade for *Mercedes AMG Petronas' F1 Team* with *Lentus Composites*. Testing was carried out to find the current original blade performance which then formed the basis of design targets for the new replacement blade.

Aspects of what was important to the customer and to what *Lentus Composites* considered essential to incorporate into the design have been listed and adopted into the design process. In addition, tools for project planning, timescales, structure and aims have been utilised to run the project efficiently and track progress towards achieving the aims.

The results of blade testing correlated closely to information gathered from the research into the current blade composition. The data from testing was used in conjunction with design optimisation to accelerate the design process. However, the optimisation was limited with respect to manufacturing techniques available and consequently the design at that stage, was manually fine-tuned by the author.

The literature review identified there is a lack of existing reliable design criteria. Even with all the testing carried out on the current blade, there were still areas of unknowns; for example, centrifugal loading cannot be tested until the new blade is in operation within the wind tunnel. Further, the calculations for the aerodynamic loading have shown to be successful for testing the current blade, but nevertheless still had to make assumptions to arrive at those results. Whilst those gaps were infilled with the considerable experience of Lentus, there does ultimately need to be 100% confidence in the results of the FEA.

With there being a lack of information on the current blade (exact material used and layup) the success of the new blade finally rests on the prototype testing. If the prototype testing results correlate with the FEA then there is confidence the blade will perform as expected in the wind tunnel. If not, then there would need to be further development of the FEA model to correlate the results followed by a reassessment of the design and targets explored in conjunction with *Lentus* and *Mercedes*.

The input to reverse engineer and design of the replacement blade was underestimated at inception both with respect to resource time and the technical challenge of achieving all targets to manufacture a successful replacement before the deadline of submitting this thesis. The final design detailed in this report achieves at least 90% of the original targets with the final hurdle being the adequate measures to deal with the high bonding stress at the joint of the foot. The initial results of the manufacturing methods considered and tried as a means to resolve that issue indicate improvements can be made with additional

development time. The project is on-going to complete the final design threads at the time of writing.

Another outcome from the review meeting with *Lentus* was after the bonding stress issues have been resolved then to have a critical design meeting with *Mercedes* to get them to buy into the analysis that has been carried out and the errors in the design targets. As well for them to review the reserve factors of the new design. After that point the prototype can be manufactured and tested.

In light of the technical challenge and being a high stakes product this is an ongoing project to achieve complete satisfaction of the customer. In terms of the aims of this report, the majority have been achieved on the way to delivering a prototype blade to *Mercedes*.

13. FURTHER WORK

As previously mentioned, the most pressing matter, which is currently in hand is that related to resolve the bonding stress issue. Once resolved, CAD all the core parts with the offset of the final laminate thickness and run FEA to check this does not affect the blade performance. Up to now, the cores geometry has been the same as the blade final geometry as it would take too much time to keep modelling the offsets from the different laminates. It is expected that the results of the FEA with the offset would have very minimum change between the models without the offsets, as the composite plate meshes were set up to extend into the part.

Once the prototype blade FEA is completed, arrange the critical design meeting with *Mercedes* to inform and gain their approval of the finalized prototype design and results. Thereafter, proceed to manufacture the first prototype blade.

The prototype then needs to be stiffness tested and LDV tests to correlate the result with the FEA. If successful, review the results with *Mercedes* and if acceptable, proceed to series manufacture of the new blades.

Projected completed.

14. REFERENCES

Aerofoil Engineering. (2003). *Aerofoil Engineering*. Retrieved June 16, 2018, from Aerofoil Engineering: http://aerofoilengineering.com/index.php

Agilent Technologies. (2000). *The Fundamentals of Modal Testing.* USA: Agilent Technologies.

AK Steel. (n.d.). *15-5 PH Stainless Steel.* Retrieved November 3, 2018, from AK Steel: https://www.aksteel.com/sites/default/files/2018-01/155ph201706.pdf

Alchemie. (2019). *RTV240.* Retrieved January 12, 2019, from Alchemie: https://www.alchemie.com/rtv240.html

Amoo, L. M. (2012). *On The Design And Structural Analysis Of Jet Engines Fan Blade Structures.* USA: Progress in Aerospace Sciences.

AZO Materials. (2001, October 23). *Stainless Steel - Grade 304*. Retrieved November 4, 2018, from AZO materials: https://www.azom.com/article.aspx?ArticleID=965

Bheemreddy, V. (2014). *Composite Laminate Modeling.* Predictive Engineering.

Buck, J. (2014). *Best Practices and Usage Guidelines for NX Nastran Mesh Gluing.* Orlando: Siemens.

Cranfield University. (2008). Jet Engine Blade Design Calulations. *Cranfield University.* Milton Keynes: Cranfield University.

CreaForm. (2019, March 30). *HANDHELD OPTICAL CMM 3D SCANNER: METRASCAN 3D*. Retrieved from CREAFORM: https://www.creaform3d.com/en/metrology-solutions/optical-3d-scanner-metrascan

Evonik. (2019, March 1). *Rohacell IG-F.* Retrieved from Rohacell.com: https://www.rohacell.com/product/peek-industrial/downloads/rohacell%20ig-f%20product%20information.pdf

Fagerberg, L., & Stromberg, K.-O. (2007). *STRUCTURAL DESIGN, OPTIMISATION AND MANUFACTURING OF A COMPOSITE WIND TUNNEL AXIAL FAN BLADE .* Stockholm: KTH Royal Institute Of Technology.

Femap. (2017). *Femap 11.4.2 Help User Guide.* Siemens.

Hameed, S. (2015). *Finite Element Analysis of a Composite VAWT Blade.*

Heinemann, T. (2014). *Axial Fan Blade Vibration Assessment under Inlet Cross-Flow Conditions Using Laser Scanning Vibrometry.* Germany: University of Erlangen-Nuremberg.

Hyson, G. (2018, September 12). Fan Blade FEA Results. (G. Spring-Benyon, Interviewer)

Jun, M. (2011). *Numerical simulation of the pneumatic elasticity for the blade of a big axial-flow fan.* Beijing: Beijing University.

Katz. (1995). *Race Car Aerodynamics.* Cambridge: Bentley Publishers.

Kaw, A. K. (2006). *Mechanics Of Composite Materials.* USA: CRC Press.

Laird, D. (2010). *Modeling Composite with Femap.* Predictive Engineering.

Lee, K.-S. (2008). *Design optimization of low-speed axial flow fan blade with three-dimensional RANS analysis.* Mechanical Science and Technology.

Lentus Composites. (2019). *Fan Blade Tooling Scheme Report.* Oxford: Lentus Composites.

MacDonald, B. (2011). *Practical Stress Analysis with Finite Elements.* Dublin: Glasnevin Publishing.

Mattews, F. L., & Rawlings, R. D. (1994). *Composite Materials Engineering And Science.* North America: CRC Press LLC.

Mcbeath. (2006). *Competition Car Aerodynamices.* Somerset: Haynes Publishing.

Meng, M. (2014). *3D FEA modelling of laminated composites in bending and their failure mechanisms.* Plymouth: Plymouth University.

Mercedes AMG F1. (2018). *Wind Tunnel*. Retrieved November 07, 2018, from Mercedes AMG Petronas F1: http://careers.mercedesamgf1.com/facilities/wind-tunnel/

Meunier, D. (n.d.). *Design Tools for Fibre Reinforced Polymer Structures.* Delaware: National Composite Network.

Miller, G. (2018, May 26). Wind Tunnel Information. (G. Spring-Benyon, Interviewer)

Moham, R. S. (2014). *Vibration analysis of a steam turbine blade.* India: Indian Institute of Technology Madras, India.

NASA. (1998). *Design and Manufacture of Wood Blades for Windtunnel Fans.* Gloucester: NASA.

NASA. (2011). *Deformed Shape Calculation of a Full-Scale.* California: NASA.

Nicolas, M. J. (2016). *Large Scale Applications Using FBG Sensors: Determination of In-Flight Loads and Shape of a Composite Aircraft Wing.* Mississippi: Mississippi State University.

Paolozzi, A. (2006). *Dynamic Analysis with Fibre Optic Sensors for Structural Health Monitoring.* Rome: University of Rome.

Polytec. (2018). *Vibrometry*. Retrieved November 08, 2018, from Polytec: https://www.polytec.com/uk/vibrometry/areas-of-application/

Predictive Engineering. (2014). *Composite Laminate Modeling.* Predictive Engineering.

Predictive Engineerings. (2011). *Foundations of FEA Modeling with Femap and NX Nastran.* Predictive Engineering.

Richmond, N. (2018, June 16). Blade Loading. (G. Spring-Benyon, Interviewer)

Schwerdt, L. (2016). *Aerodynamical and structural analysis of operationally used turbine blades.* Germany.

Siemens. (2016). *FEMAP Commands.* Siemens.

Sinha, S. (2017). *Vibration analysis of composite airfoil blade using orthotropic thin shell bending theory.* USA: The Ohio State University.

Suzuki, T. (2015). *Fatigue Load and Life Estimation of Composite Turbine Blades under Random Ocean Current.* Yokohama: IHI Corporation.

TenCate. (2018). *E722.* Retrieved November 26, 2018, from TenCate Advanced Composites: https://www.tencatecomposites.com/product-explorer/products/fSmt/E722

Torayca. (2018). *T700S Data Sheet*. Retrieved Novenber 15, 2018, from Torayca: https://www.toraycma.com/page.php?id=661

Vanderplaats, G. N. (2007). *Multidiscipline Design optimixation.* California: VR And D.

Wollmann. (2016). *Design and testing of composite compressor blades with focus on the vibration behaviour.* Germany.

Yang, L. (2007). *EXPERIMENTAL RESEARCH ON AERODYNAMIC PERFORMANCE AND EXIT FLOW FIELD OF LOW PRESSURE AXIAL FLOW FAN WITH CIRCUMFERENTIAL SKEWED BLADES.* Shanghai: School of Mechanical Engineering, Shanghai Jiaotong University, Shanghai .

Appendix A – FEA & Composite Material Principles

FEA uses the method of analysing displacement. FE requires the solution of the matrix equation $Ku = P$. K is the sum of element stiffness matrices K_i and NE the number of finite elements in a structure (Vanderplaats, 2007).

$$K = \sum_{i=1}^{NE} K_i$$

Equation 11 FEA solution matrix

P column is the matrix which contains the load vectors for each loading conditions and U columns are the corresponding nodal displacements. Stiffness matrix is the function of the design variables defining the structure. The load vectors P may also be a function of the other design variables. One assuming a proposed design has been specified, the stiffness matrix K and load vectors can be created (Vanderplaats, 2007). Therefore the displacements U must be solved:

$$u = K^{-1}P$$

Equation 12 displacement from stiffness matrix

The stiffness element k_i is formed from stiffness matrix k_i^0 using the local co-ordinate system of the elements and geometric transformation matrix T:

$$k_i = T^T k_i^0 T$$

Equation 13 element stiffness matrix

u displacements joint is already calculated it is possible to calculate the forces on each element using the displacement and element stiffness matrix which are with the associated element. It is transformed to the coordinate system locally by:

$$u^0 = Tu$$

Equation 14 transformation matrix

Where u and u^0 are only the displacements contained with the associated nodes of the element. The element forces now are:

$$f = k_i^0 u^0$$

Equation 15 element force

It is now possible from all of the forces to calculate the corresponding constraints and stresses (Vanderplaats, 2007).

The FEA package used in this project was *GENESIS Design Studio*. Design Studio is capable of running linear structure analysis, nonlinear, frequency mode analysis, and part optimisation.

Composite FEA process

The following steps outline the process used to run a single analysis on a composite structure:

1. First is to input the orthotropic properties of the materials into the software. Material which is considered to be orthotropic is defined by having the classification of properties performing differently depending on the loading direction. For example a unidirectional laminar might have very high tensile loading capabilities in the longitudinal direction to the fibre, but have significantly lower values in the transverse direction. The performance of an orthotropic material can be classed by acting in three different planes of symmetry. Each plane gives a unique Young's modulus value for the longitudinal direction 1 ($E11$), transverse direction 2 ($E22$), and in plain direction 3 ($E33$). As well as Young's modulus this applies to the shear stress within the material ($G12$ and $G13$) (Kaw, 2006). The finite element software would evaluate stiffness terms as shown below:

$$\begin{Bmatrix} \sigma_1 \\ \sigma_2 \\ \sigma_3 \\ \tau_{23} \\ \tau_{13} \\ \tau_{12} \end{Bmatrix} = \begin{bmatrix} C_{11} & C_{12} & C_{13} & 0 & 0 & 0 \\ C_{12} & C_{22} & C_{23} & 0 & 0 & 0 \\ C_{13} & C_{23} & C_{33} & 0 & 0 & 0 \\ 0 & 0 & 0 & C_{44} & 0 & 0 \\ 0 & 0 & 0 & 0 & C_{55} & 0 \\ 0 & 0 & 0 & 0 & 0 & C_{66} \end{bmatrix} \begin{Bmatrix} \varepsilon_1 \\ \varepsilon_2 \\ \varepsilon_3 \\ \gamma_{23} \\ \gamma_{13} \\ \gamma_{12} \end{Bmatrix}$$

Equation 16 orthotropic stiffness terms

Composites are usually made up of laminates, and a laminate is made up of single plies which are known as a laminar material. A laminar ply is constructed by combining a resin matrix impregnated with a reinforcement material (fibre). A typical laminar ply would be a unidirectional fibre impregnated with an epoxy resin (Kaw, 2006). A three plane properties can be calculated by taking a percentage volume fraction of the resin matrix and reinforcement. FEA can find the final terms by using the rule of mixtures technique:

$$\begin{aligned} E_L &= E_f V_f + E_m V_m \\ \frac{1}{E_T} &= \frac{V_f}{E_f} + \frac{V_m}{E_m} \\ \frac{1}{G_{LT}} &= \frac{V_f}{G_f} + \frac{V_m}{G_m} \\ \nu_{LT} &= \nu_f V_f + \nu_m V_m \end{aligned}$$

Equation 17 Composite rule of mixtures equation (Bheemreddy, 2014)

2. Once the materials are defined, the part geometry (CAD) can be imported into the software and mesh the structure with element nodes. The type of meshes can vary from volume 4 node tetrahedron, to plane 4 nodes plates. Plate elements are the most common way of modelling composite structures. They use the classical lamination theory (CLT) to calculate the behaviour of a composite lay-up. CLT is similar to classical plate theory (CPT) but CLT takes into account the material having different properties in different directions. CLT only works for thin laminates with in-plane direction. There are 4 parts to CLT (Bheemreddy, 2014) (Femap, 2017).

Part 1 Kinematic Equations - *u0, v0*, and *w0* are the displacements of the middle plane in the *x, y,* and *z* directions. Again, *εx0, εy0*, and *γxy0* are the mid-plane strains, and *κx, κy*, and *κxy* are the curvatures.

$$\begin{Bmatrix} \varepsilon_x \\ \varepsilon_y \\ \gamma_{xy} \end{Bmatrix} = \begin{Bmatrix} \varepsilon_x^0 \\ \varepsilon_y^0 \\ \gamma_{xy}^0 \end{Bmatrix} + z \begin{Bmatrix} \kappa_x \\ \kappa_y \\ 2\kappa_{xy} \end{Bmatrix} = \begin{Bmatrix} \frac{\partial u_0}{\partial x} \\ \frac{\partial v_0}{\partial y} \\ \frac{\partial u_0}{\partial y} + \frac{\partial v_0}{\partial x} \end{Bmatrix} - z \begin{Bmatrix} \frac{\partial^2 w_0}{\partial x^2} \\ \frac{\partial^2 w_0}{\partial y^2} \\ 2\frac{\partial^2 w_0}{\partial x \partial y} \end{Bmatrix}$$

Equation 18 Kinematic Equations (Bheemreddy, 2014)

Part 2 Constitutive Equations - K indicates the Kth layer counting from the top of the laminate.

$$\begin{Bmatrix} \varepsilon_x \\ \varepsilon_y \\ \gamma_{xy} \end{Bmatrix}_k = [T]_k^T [S]_k [T]_k = \begin{bmatrix} \bar{S}_{11} & \bar{S}_{12} & \bar{S}_{16} \\ & \bar{S}_{22} & \bar{S}_{26} \\ sym. & & \bar{S}_{66} \end{bmatrix}_k \begin{Bmatrix} \sigma_x \\ \sigma_y \\ \sigma_{xy} \end{Bmatrix}_k$$

Equation 19 Constitutive Equations (Bheemreddy, 2014)

Part 3 Resultants – All the terms on the left side are the force and moment resultants.

$$\begin{Bmatrix} N_x \\ N_y \\ N_{xy} \end{Bmatrix} = \int_{-t/2}^{t/2} \begin{Bmatrix} \sigma_x \\ \sigma_y \\ \tau_{xy} \end{Bmatrix} dz = \sum_{k=1}^{N} \int_{z_{k-1}}^{z_k} \begin{Bmatrix} \sigma_x \\ \sigma_y \\ \tau_{xy} \end{Bmatrix}_k dz$$

$$\begin{Bmatrix} M_x \\ M_y \\ M_{xy} \end{Bmatrix} = \int_{-t/2}^{t/2} z \begin{Bmatrix} \sigma_x \\ \sigma_y \\ \sigma_{xy} \end{Bmatrix} dz = \sum_{k=1}^{N} \int_{z_{k-1}}^{z_k} \begin{Bmatrix} \sigma_x \\ \sigma_y \\ \sigma_{xy} \end{Bmatrix}_k z dz$$

Equation 20 Resultants (Bheemreddy, 2014)

Part 4 Equilibrium Equations –

$$\frac{\partial N_x}{\partial x}+\frac{\partial N_{yx}}{\partial y}=-p_x$$
$$\frac{\partial N_{xy}}{\partial x}+\frac{\partial N_y}{\partial y}=-p_y$$
$$\frac{\partial^2 M_x}{\partial x^2}+2\frac{\partial^2 M_{xy}}{\partial x \partial y}+\frac{\partial^2 M_y}{\partial y^2}=-p_z$$

Equation 21 Equilibrium Equations (Bheemreddy, 2014)

The 4 parts are then brought together to give the stiffness matrices A, B and D. There is a relationship between the resultants (forces and moments) and strains of the composite laminates. If the stresses in the resultants are replaced with constitutive equations the following is given:

$$\begin{Bmatrix} N_x \\ N_y \\ N_{xy} \end{Bmatrix} = \sum_{k=1}^{N} \begin{bmatrix} \bar{C}_{11} & \bar{C}_{12} & \bar{C}_{16} \\ & \bar{C}_{22} & \bar{C}_{26} \\ sym. & & \bar{C}_{66} \end{bmatrix}_k \left(\int_{z_{k-1}}^{z_k} dz \begin{Bmatrix} \epsilon_x^0 \\ \epsilon_y^0 \\ \gamma_{xy}^0 \end{Bmatrix} + \int_{z_{k-1}}^{z_k} z dz \begin{Bmatrix} \kappa_x \\ \kappa_y \\ 2\kappa_{xy} \end{Bmatrix} \right)$$
$$\begin{Bmatrix} M_x \\ M_y \\ M_{xy} \end{Bmatrix} = \sum_{k=1}^{N} \begin{bmatrix} \bar{C}_{11} & \bar{C}_{12} & \bar{C}_{16} \\ & \bar{C}_{22} & \bar{C}_{26} \\ sym. & & \bar{C}_{66} \end{bmatrix}_k \left(\int_{z_{k-1}}^{z_k} z dz \begin{Bmatrix} \epsilon_x^0 \\ \epsilon_y^0 \\ \gamma_{xy}^0 \end{Bmatrix} + \int_{z_{k-1}}^{z_k} z^2 dz \begin{Bmatrix} \kappa_x \\ \kappa_y \\ 2\kappa_{xy} \end{Bmatrix} \right)$$

Equation 22 CLT replaced equation (Bheemreddy, 2014)

Then CLT applies the summation and integration operations to their respective components, the force and moment resultants can be expressed as:

$$\begin{Bmatrix} N_x \\ N_y \\ N_{xy} \end{Bmatrix} = \begin{bmatrix} A_{11} & A_{12} & A_{16} \\ & A_{22} & A_{26} \\ sym. & & A_{66} \end{bmatrix} \begin{Bmatrix} \epsilon_x^0 \\ \epsilon_y^0 \\ \gamma_{xy}^0 \end{Bmatrix} + \begin{bmatrix} B_{11} & B_{12} & B_{16} \\ & B_{22} & B_{26} \\ sym. & & B_{66} \end{bmatrix} \begin{Bmatrix} \kappa_x \\ \kappa_y \\ 2\kappa_{xy} \end{Bmatrix}$$
$$\begin{Bmatrix} M_x \\ M_y \\ M_{xy} \end{Bmatrix} = \begin{bmatrix} B_{11} & B_{12} & B_{16} \\ & B_{22} & B_{26} \\ sym. & & B_{66} \end{bmatrix} \begin{Bmatrix} \epsilon_x^0 \\ \epsilon_y^0 \\ \gamma_{xy}^0 \end{Bmatrix} + \begin{bmatrix} D_{11} & D_{12} & D_{16} \\ & D_{22} & D_{26} \\ sym. & & D_{66} \end{bmatrix} \begin{Bmatrix} \kappa_x \\ \kappa_y \\ 2\kappa_{xy} \end{Bmatrix}$$

Equation 23 Integrated CLT (Bheemreddy, 2014)

The integrated equation can be given as follows:

$$\begin{Bmatrix} \mathbf{N} \\ \mathbf{M} \end{Bmatrix} = \begin{bmatrix} \mathbf{A} & \mathbf{B} \\ \mathbf{B} & \mathbf{D} \end{bmatrix} \begin{Bmatrix} \boldsymbol{\epsilon}^0 \\ \boldsymbol{\kappa} \end{Bmatrix}$$

Equation 24 ABD stiffness equation (Bheemreddy, 2014)

A is the extensional stiffness, B is coupling stiffness, and D the bending stiffness of the laminate. The stiffness matrices are given as follows:

$$A_{ij} = \sum_{k=1}^{N} \left(\bar{C}_{ij}\right)_k (z_k - z_{k-1}) = \sum_{k=1}^{N} \left(\bar{C}_{ij}\right)_k t_k$$
$$B_{ij} = \frac{1}{2}\sum_{k=1}^{N} \left(\bar{C}_{ij}\right)_k \left(z_k^2 - z_{k-1}^2\right) = \sum_{k=1}^{N} \left(\bar{C}_{ij}\right)_k t_k \bar{z}_k$$
$$D_{ij} = \frac{1}{3}\sum_{k=1}^{N} \left(\bar{C}_{ij}\right)_k \left(z_k^3 - z_{k-1}^3\right) = \sum_{k=1}^{N} \left(\bar{C}_{ij}\right)_k \left(t_k \bar{z}_k^2 + \frac{t_k^3}{12}\right)$$

Equation 25

Finally this then is used as the displacement method in FEA to solve (Bheemreddy, 2014).

An extra composite characteristic which is used in FEA is the laminate failure theory. As the behaviour of composites is very complex, failure theories are a great tool in post processing results to understand how individual plies (lamina) are stressed within a laminate from the total load being applied to the part. They can identify if a single ply is failing within a laminate lay-up. There are many theories in how it calculates its failure index, but some are more accurate than others when compared to experimental data. Bheemreddy, Matthews & Rawlings, and Kaw's composite books found one of the best, when compared to data, is Tsai-Wu's theory. In addition, a paper by Meng looking into different theories being used in FEA found Tsai-Wu to be the best as well (Meng, 2014).

Tsai-Wu is based on the total strain energy theory of Beltrami but applies it to the general lamina state of plane stress with unequal tensile and compressive strengths (Kaw, 2006).

$$F_1\sigma_1 + F_2\sigma_2 + F_{11}\sigma_1^2 + F_{22}\sigma_2^2 + 2F_{12}\sigma_1\sigma_2 + F_{66}\sigma_{12}^2 = 1$$

$$F_1 = \frac{1}{X_t} - \frac{1}{X_c}$$
$$F_2 = \frac{1}{Y_t} - \frac{1}{Y_c}$$
$$F_{11} = +\frac{1}{X_t X_c}$$
$$F_{22} = +\frac{1}{Y_t Y_c}$$
$$F_{66} = +\frac{1}{S^2}$$

Equation 26 Tsai-Wu failure theory (Kaw, 2006)

Appendix B – Testing Methodology

Stiffness Test

Testing outcomes

The following were the aims of the stiffness testing:

1. Load the blade in increments to ascertain if the deflection is linear, thus the stiffness would be linear.
2. Test the blade up to 421Kg and find the corresponding deflection along the blade.
3. Test to 500Kg to establish a safety margin over the anticipated operating load for developing the new design.

Procedure of testing

The following is a step by step procedure of testing the blade on the stiffness rig:

1. Attach blade to testing rig and set out tracking dots for GOM system. At the same time using data from the blade testing CAD model, mark out the positions for the profile clamps.

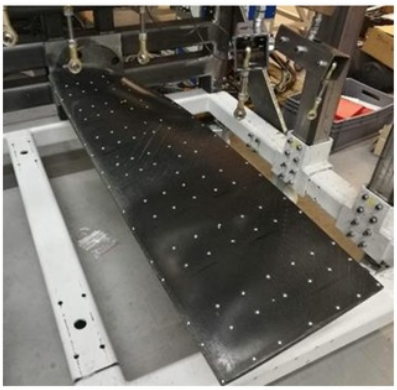


Figure 160 blade being attached to testing rig

2. Record weights of all whiffletree and profile clamps.
3. Calibrate GOM system.



Figure 161 calibrating GOM system

4. Track the blade droop arising from the load applied by the weight of the profile clamps.

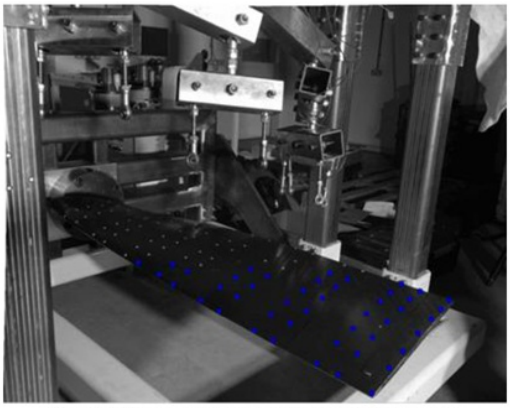


Figure 162 tracking blade before attaching clamps

5. Attach profile clamps and record droop. Set out GOM tracking dots on profile clamps.

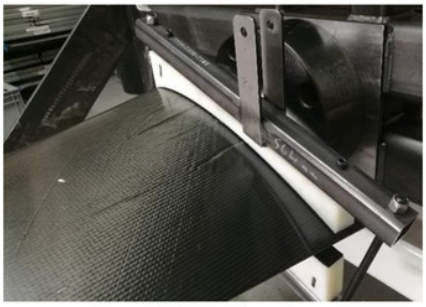


Figure 163 attaching clamps

6. Attach whiffletree to load cell and calibrate load cell against total weight of components.



Figure 164 calibrating load cell

7. Attach whiffletree to profile clamps and zero load cell.



Figure 165 blade fully set up for testing

8. Begin testing and increase the load by 250N increments. At each increment, record blade displacement through GOM system. Repeat until excess 5000N is achieved.



Figure 166 testing blade

9. Repeat test to ensure consistent results are recorded.

Natural Modal Test

As discussed in Section 2.2.4, establishing the vibration response of the blade is another important aspect of the blade design. Two methods of finding the current blade response could be carried out with the available equipment; tap testing and LDV testing. These were both carried out to be able to correlate the results between two sets of data.

Testing outcomes

The following were the aims of the tap testing:

1. Find the average first natural frequency of the blade; the testing equipment used was only adequate enough to find the first frequency. This meant the tap testing results would be used to validate the results of the LDV.

LDV testing aims were:

1. Find a first natural frequency that correlates with the tap testing results.
2. Find the first 4 natural frequencies of the blade and the mode shapes. The mode shapes can be correlated against F&S's findings from their report.

Procedure of tap testing

Due to the complexity of the blade shape, a single accelerometer was not adequate enough to give consistent results. To overcome this, a mesh style rig was constructed which consisted of 44 sensors evenly placed over the blade (see Figure 167).



Figure 167 mesh of 44 accelerometers

Only 8 sensors could be read at any one time due to the available equipment which meant the test would have to be carried out multiple times. This led to ensuring the force input to the blade was consistent between tests. To achieve this, the amplifier on the LDV rig was used to apply a force to the blade (see Figure 168), which meant the force could be controlled and consistent throughout the tests.



Figure 168 LDV amplifier on tap testing rig

The procedure of the test is as follows:

1. Attached sensors to blade
2. Set up 2x PicoScope and connect to 8 sensors
3. Triger amplifier and record results
4. Repeat test until all 44 sensors have been recorded

Procedure of LDV testing

The LDV was set up to measure the same points on the blade as for the tap testing and used the amplifier to ensure the same force input (see Figure 169).

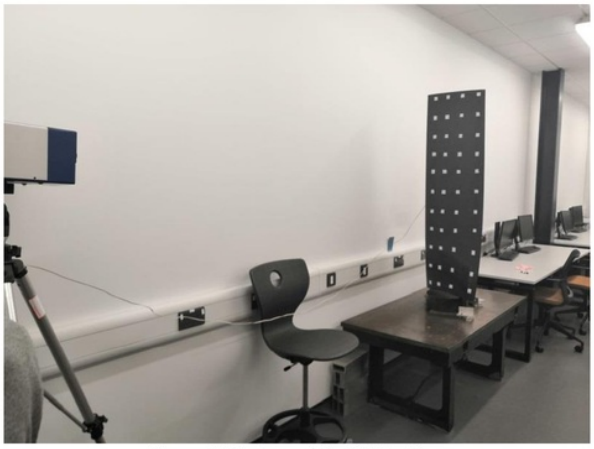


Figure 169 set up of the LDV testing

The procedure of testing is as follows:

1. Calibrate camera distance from blade and lighting
2. Set the LDV to capture points on blade. The points to be taken are to be the same as for tap testing
3. Run LDV test
4. Repeat to correlate consistent results

Appendix C – Blade Assembly Meshing Categories

F&S used a mesh combination of quadrilateral (quads) shell elements for the composite parts and solid brick elements for their steel foot design. Their reasoning for this combination was that modelling composites with shell quads gave the best results when correlating FEA models, and with respect to the blade foot, bricks are considered to give more accurate stress results compared to tetrahedral (tets) or wedge elements (Fagerberg & Stromberg, 2007). F&S did not state how the sandwich parts were meshed, nor if they were even included in the FEA model. Saqib Hameed meshed the turbine blade in a similar format to F&S but there were no sandwich parts in their design (Hameed, 2015).

Predictive Engineering's book on composite laminate modelling recommends for meshing composite parts to use 2D elements over 3D as it gives more freedom when applying CLT. Also, quads over tets from past experience appear to capture the stress concentration areas better (Predictive Engineering, 2014). A book by Bryan J MacDonald also recommends using quads for 2D elements as they gave more accurate results (MacDonald, 2011).

Predictive Engineering also publish a book on Foundations of FEA Modelling which states when possible, the use of brick elements for solid meshing as this gives better results with solving stress in the components. Other benefits are that it usually takes less time to solve (being less nodes) plus works better with orthotropic materials. However, with complex geometry, it can be difficult to generate a mesh and is time consuming (Predictive Engineerings, 2011). MacDonald's book states tets produce acceptable displacement results but generally do not give accurate results for stress, which is mainly due to the element shapes being stiff in comparison to bricks. However, in more recent years there has been great improvement with tets elements being closer to bricks (MacDonald, 2011). *Predictive Engineering* also confirms tets elements have improved to match the performance of bricks when using second order elements. Tetrahedral first order elements are close behind the performance of second. The down side of using second order is that it requires more time to resolve. However, weighing up the time needed to generate the brick mesh if the geometry is complex and the level of accuracy needed from the model, the difference in time overall is small (Predictive Engineerings, 2011).

Attempting to mesh the geometry of the blade using 3D bricks is difficult due to its complexity (see Figure 170). Consequently, using tets for the sandwich and steel parts on balance is considered the optimal approach.

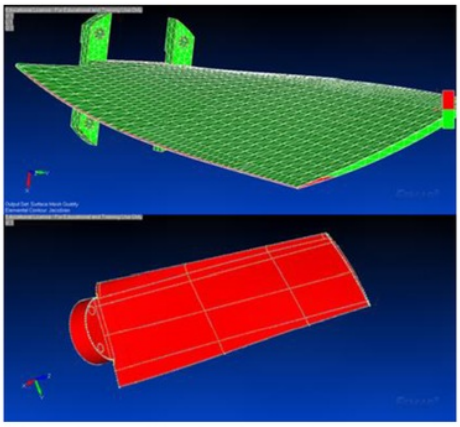


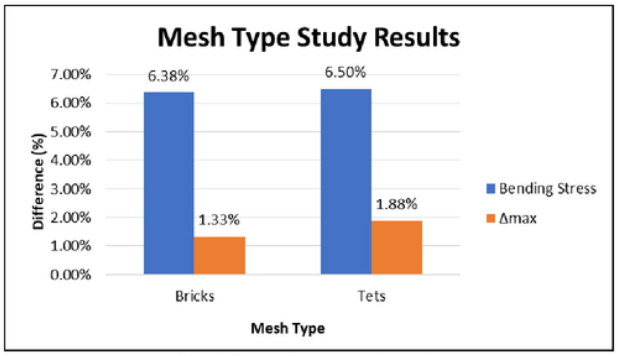
Figure 170 showing the difficulties with meshing the complex geometry

To establish how much of a difference in results there is between bricks and tets, a parameter study was undertaken on a simple cantilever bar with a point load at the free end and fixed at the other (see Figure 171). This enables correlation of the FEA results through simple hand calculations for deflation and the average bending stress at the fixed end.



Figure 171 bar model for correlation study

Using the same mesh size for each meshing type, the quads elements give slightly more accurate results against the predicted hand calculations (Graph 20). The study results are not representative of the blade, but do give an indication that the FEA results between the two mesh types have converged in recent years.



Graph 20 mesh type study results

Predictive Engineering's book on composite laminate modelling recommends that if the component is treated as a sandwich composite (which the blade could be viewed as with it essentially being composite on the outside encasing and an inner core/steel), then the part could be meshed in all shell elements. This could be achieved by positioning the core/steel material in the middle of the composite layup information for CLT. However, due to the complex geometry, the plate elements would not align at the middle because of the twist in the blade and variation in the thickness along the length of the geometry (see Figure 172 for illustration).

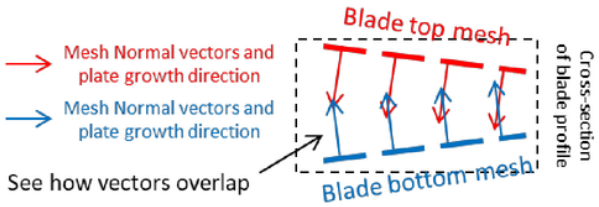


Figure 172 showing how the plate mesh would overlap with the complex geometry

Appendix D – Mesh Connection Methods

To find the best method to use, a parameter study was carried out on a coupon cantilever beam which represented the blade model by having a steel base tet solid mesh (foot of the blade), *Rohacell* core solid mesh (blade sandwich parts) and E722 T700S composite 2D quad mesh (see Figure 173).

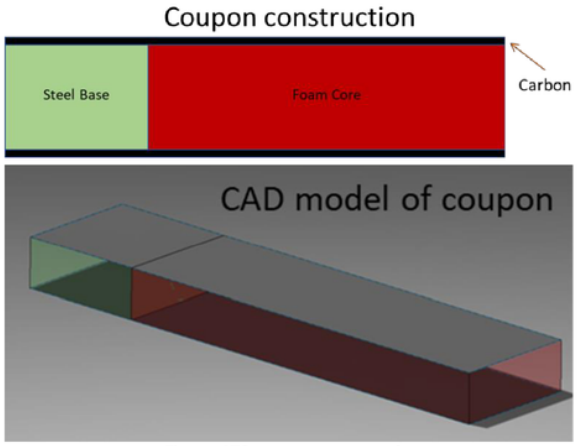


Figure 173 coupon construction

The idea of coupon was to represent the main parts of the blade design in plain geometry to enable simple hand calculations. The plate mesh model as discussed in **Appendix C** could easily be manufactured for testing, providing three methods of validating and correlating the FEA results and finding the best connection method.

The coupon had three different loads applied to it for the study:

Table 14 loads used for the coupon study

Load Type	Load
Cantilever beam with a point load at the free end	49.05N (5Kg)
Cantilever beam with a point load at the free end	98.1N (10Kg)
Cantilever beam loaded in tension	1000N

The hand calculations compared the max deflation results for all 3 loads, while the plate mesh model can potentially compare both the max deflation and stress distribution. However, due to limited equipment available for the testing, the results could only be compared to the max deflation under a 49.05N load.

The hand calculations used to calculate the max deflections follows:

- **Max bending deflection**

$$\delta max = \int_0^L \frac{Mmm}{EI} dx$$

Equation 27 max bending deflection

To calculate the max deflection, the cantilever beam is considered non uniform with a point load at the free end using a duplex equation (23). The beam was sectioned A,B,C with two sets of EI values as illustrated in Figure 174 together with dimensions used in calculations.

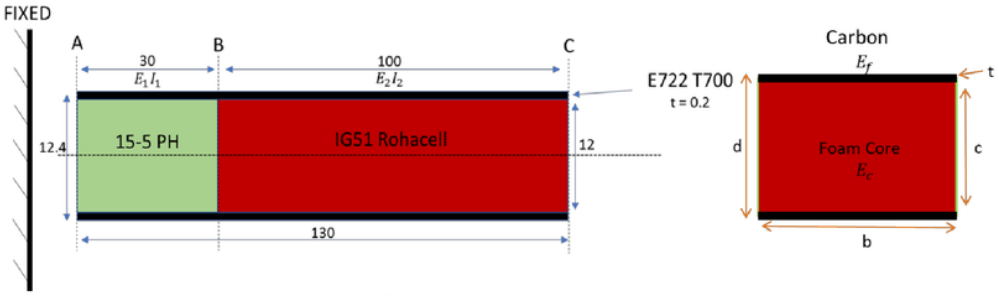


Figure 174 coupon sections and measurements

Initially, work out overall E and I values for both E_1I_1 and E_2I_2 as the part is a sandwich composite. This can be done using parallel axis theorem and CLT.

$$I_1 = I + Ad^2$$

Equation 28 parallel axis theorem

The EI values must = the same for the equation to work. As E_1I_1 has a much higher number because it has the steel base in the sandwich, it can be treated as a fraction.

$$\delta max = \int_C^B \frac{Mmm}{E_2I_2} dx + \int_B^A \frac{Mmm}{0.02E_1I_1} dx$$

Equation 29 max bending deflection formula for the coupon

Equation 25 then gives the max deflection for the coupon under bending load.

- **Tension deflection**

$$\Delta L = \frac{FL}{EA}$$

Equation 30 max deflection under tension load

To work out the total deflection under tension, the ΔL values are worked out for *B-C* and *A-B* then added together to give total ΔL (see Equation 31). The E values are the same as for δmax.

$$\frac{FL_{B-C}}{E_2A} + \frac{FL_{A-B}}{E_1A} = Total\ \Delta L$$

Equation 31 max deflection under tension load formula for the coupon

The hand calculations were validated by comparing with FEA results from using a plate mesh model of the coupon. Table 15 are the results between the two sets of deflection data which compare closely and thus the hand calculations were considered viable for this study.

Table 15 validating the hand calculation results

	Hand Calc (mm)	FEA (mm)	Difference (%)
49.05N (5Kg)	0.796	0.778	2.31%
98.1N (10Kg)	1.59	1.556	2.19%
1000N	16.23	15.86	2.33%

Using a combination of brick, tets and quad elements in the blade model, it is extremely difficult to line the nodes up between the meshes. To do so was not considered practical. Also the RB3 method to integrate connections was discarded due to difficulty in modelling and reliability of results. Three methods remained to be tested for adoption:

- Glue contact regions
- Spring elements
- RB2

Glue contact regions – glue contacts connects the meshes together by simulating infinitely strong glue that never delaminates between the two mesh surfaces. Figure 175 is the coupon model set with the regions that are to have glue bonding together.

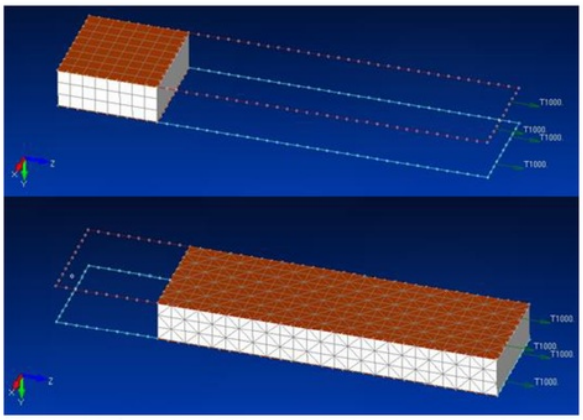
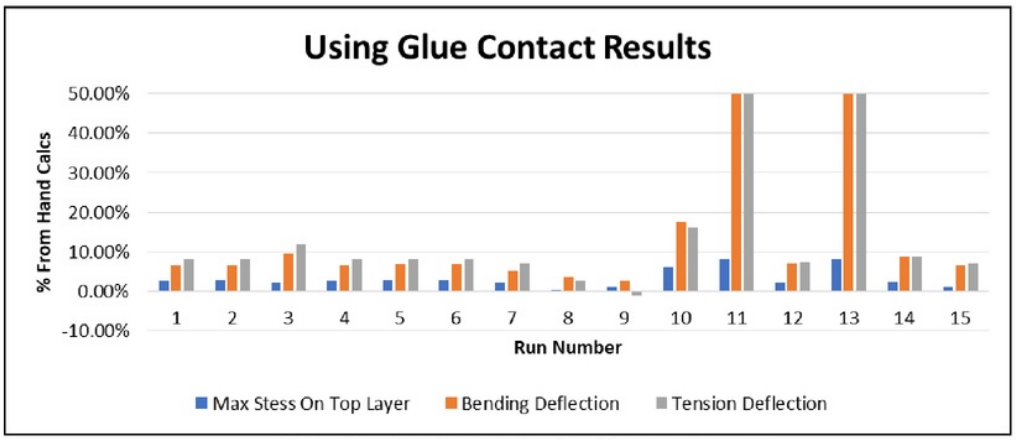


Figure 175 FEA model of coupon with glue contact regions connecting the meshes together

Within the FEA software there are multiple settings to define how the glue contacts behave in the model. Graph 21 is the FEA results of using the different combination of settings to define the glue contacts against the hand calculation results. Testing found that run 8 had the best overall correlation between the different loading types on the coupon. Run 8 sets the glue as a deformable weld between the two mesh surfaces.



Graph 21 testing glue contact regions FEA correlation results

Spring elements – spring elements connect the meshes together by simulating small springs in between the two sets of nodes on the mesh surfaces (see Figure 176). The springs can be set to a calculated stiffness value for the resin matrix of the composite that connects the parts together.

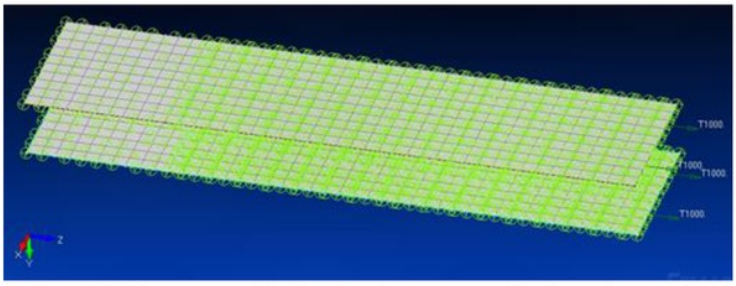


Figure 176 FEA coupon model with spring elements connecting the meshes together

The spring stiffness value for this test has been calculated using the following equation:

$$Bond\ K = \frac{Bulk\ E \times Bond\ A}{Bond\ Gap}$$

Equation 32 working out the spring element stiffness

$Bond\ A$ is the area of the element size, bond gap is assumed to be 0.1mm and the $Bulk\ E$ is the bulk modulus of epoxy resin which is assumed to be 3500MPa, this gives a stiffness value of 315000N/mm.

RB2 – RB2 connect the meshes together by connecting the nodes on the mesh surfaces by creating rigid body elements (see Figure 177).

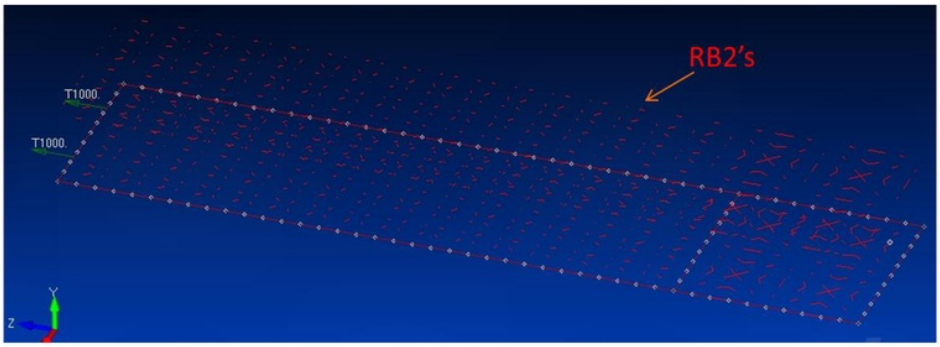
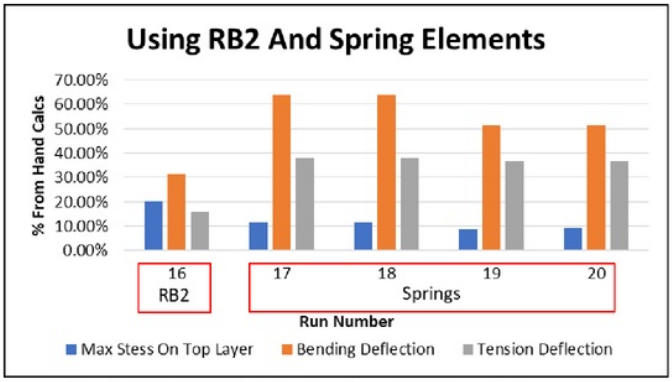


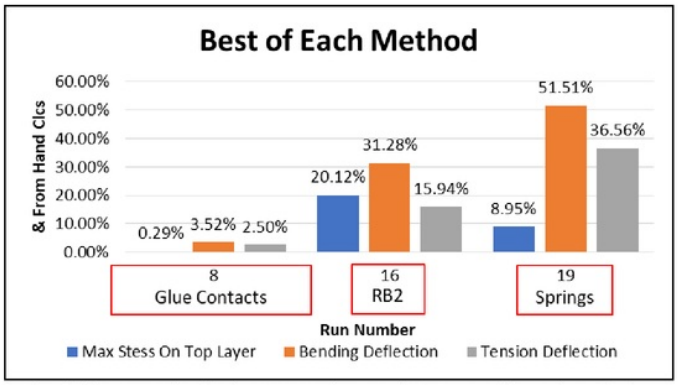
Figure 177 FEA coupon model with RB2s connecting the meshes together

Graph 22 is the results of testing the RB2 and spring elements methods on the coupon model against the hand calculation results. Run 17 used the stiffness value of the calculation, however with the bond gap and the epoxy resin modulus being assumed, 3 extra runs where carried out to see how sensitive the stiffness value was to the results. Making the stiffness value very high or low did not affect the results by much, meaning the stiffness value is not very sensitive to the end results.



Graph 22 testing RB2 and spring elements FEA correlation results

Graph 23 is comparing the best results from the three methods. Using the settings from run 8 seems to be the best way of modelling the connection between the meshes.



Graph 23 comparing the best connection results between the each method

Figure 178 is the FEA coupon model colour contour results of the best methods. Looking at the colour contours of the stress and deflection, the glue contacts gives an even distribution across all three load types. In comparison, the RB2 and spring elements give a disjointed distribution of stress. Conferring the results with Graeme Hyson (stress engineer at *Lentus*), he agreed the FEA colour contour results should have an even distribution and not to be patchy to represent realistic defamation and stress in a part (Hyson, 2018).

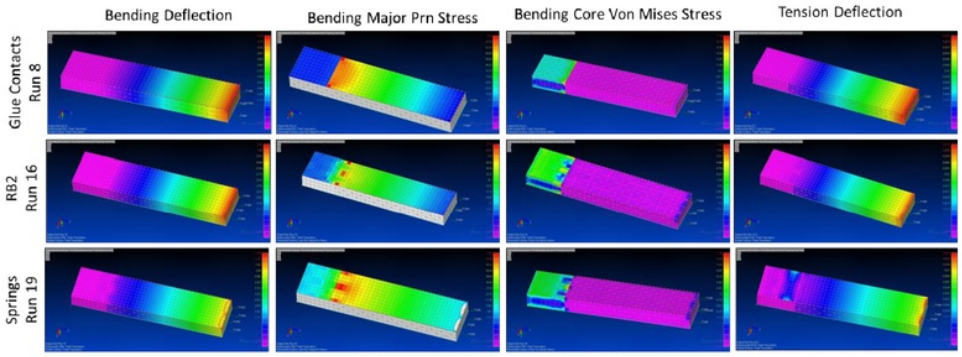


Figure 178 FEA coupon model colour contour results

Figure 179 is comparing the glue contact results against the plate model results. The results between the two are very similar which leads to the conclusion that the glue contacts are the best method integrating the multiple meshes for the blade.

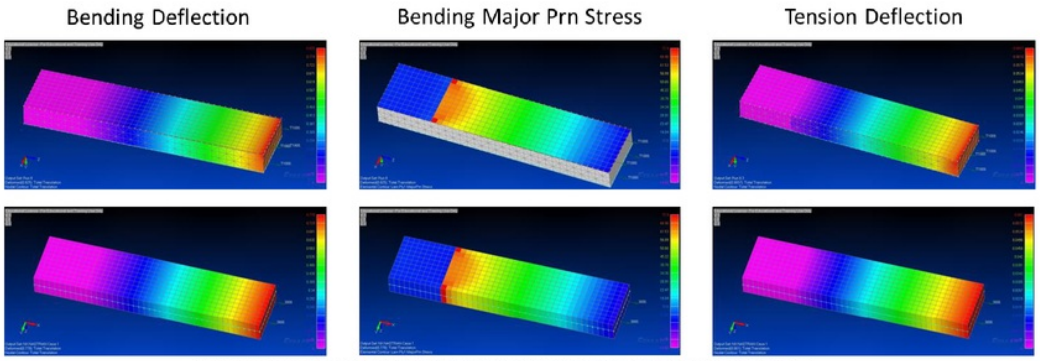


Figure 179 comparing the results of the glue contacts and plate mesh model

To reinforce the decision to adopt the glue contacts as the best method, the coupon was manufactured with the same materials for actual testing as the coupon used in FEA model with the same composite layup (see Figure 180).



Coupon Layup:
OP10 – E722 150g UD @ 0˚
OP20 – Core
OP30 - E722 150g UD @ 0˚

Figure 180 coupon constructions

The coupon was tested fixed to an aluminium rig and loaded with 49.05N (5Kg weight) at the free end (see Figure 181) where a DTi was positioned to take measurements. The test was repeated to gain an average result.

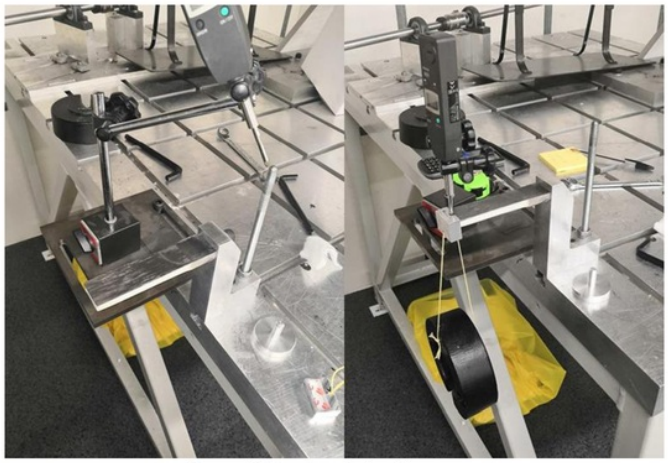


Figure 181 testing rig for the coupon

The initial test results did not correlate with the FEA and hand calculation results (see Table 16).

Table 16 results of testing the coupon

	Test 1		
	Results	Coupon Results	Diff (%)
Hand	0.796	1.51	89.70%
FEA Plate	0.778	1.51	94.09%
FEA	0.825	1.51	83.03%

With there being such a difference between the results, it was unlikely the first test was correct. Further inspection of the manufactured coupon found that during the curing process, the *Rohacell* core had been crushed, which meant the cross-section area of the part had become smaller resulting in a smaller second moment of area than originally allowed for (see Figure 182). The revised value (x) was 9.62mm.

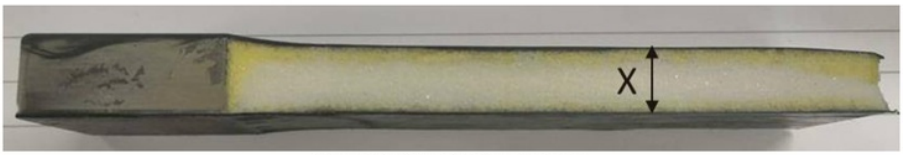


Figure 182 manufactured coupon

Inputting the revised value into the calculations, the FEA model outputted results a lot closer (see Table 17) but not enough for validation.

Table 17 results of testing coupon with new I value

	Test 2		
	Results	Coupon Results	Diff (%)
Hand	1.013	1.51	49.06%
FEA Plate	1.059	1.51	42.59%
FEA	1.0778	1.51	40.10%

When considering this further, it was believed that there was a movement in the aluminium holding rig during testing. Consequently, the rig was incorporated into the FEA model to see if it influenced the results.

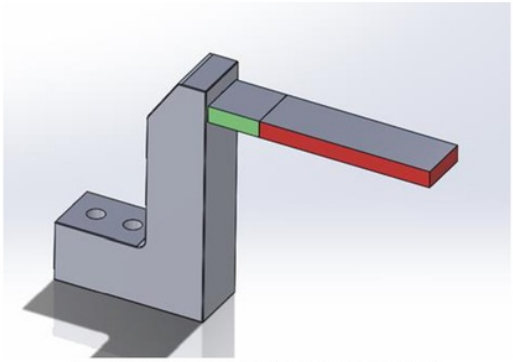


Figure 183 aluminium holding rig with coupon

Running the FEA model again with the rig included found the results to correlate within 6% (see Table 18).

Table 18 results of FEA model with rig compared to testing

	Test 3		
	Results	Coupon Results	Diff (%)
FEA	1.434	1.51	5.30%

In conclusion, the overall best method for connecting the meshes together within the blade model is using glue contacts with the settings used in run 8 as it has acceptable correlation between all fronts.

Appendix E – Mesh Density

Mesh density is an impotent aspect of modelling in FEA (MacDonald, 2011). Unfortunately there is no straightforward answer to what is the right mesh size or density, but there are methods to help find the right mesh approach:

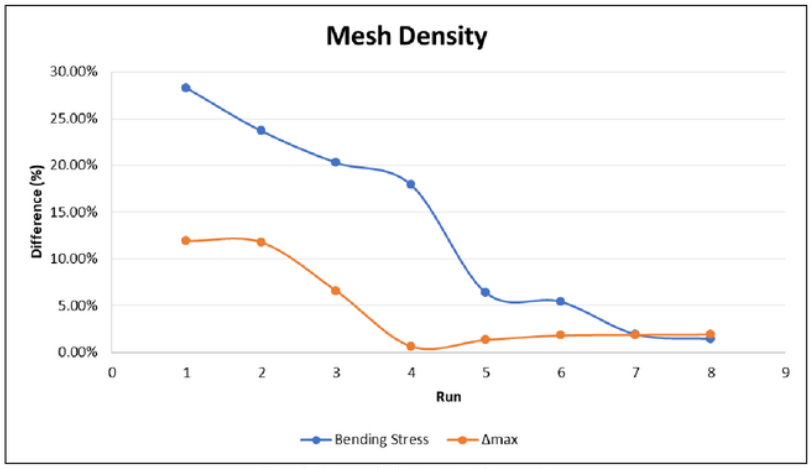
1. Compare FEA results to experimental testing data
2. Run an initial analysis with a medium mesh density followed by a further run with a fine mesh and ascertain if there are big differences in the results
3. Run with overly fine mesh throughout the model

The first method is finding the mesh convergence point when the results correlate with the testing data (MacDonald, 2011). To see how mesh density affects the results, a parameter study was conducted on the same cantilever bar model in appendix C. Table 19 lists out how the nodes and elements were increased over 8 runs.

Table 19 nodes and elements numbers over 8 runs

Run	Number of Elements	Number of Nodes
1	72	80
2	120	128
3	300	310
4	1080	1098
5	4560	4598
6	28200	28294
7	112800	112988
8	2826000	2826942

Graph 24 is the results of the study. As expected the accuracy of the results increases as the mesh becomes finer, but past run 7 does not have a sufficient improvement. This means run 7 is the optimum convergence point.



Graph 24 mesh density study results

This approach however was not feasible as the composite layup of the current blade is unknown, thus there are no comparable results. Also, the mesh may converge at different mesh sizes; for example, displacement in general converges faster than stress results (MacDonald, 2011). For the blade interested in both output of results.

The second method is best suited to assist in refining the blade mesh. However, it would need to be applied every time the FEA model changed following a design update.

With respect to the third option; due to the size of the blade, choosing a very fine mesh throughout the model would increase the solving time to an unacceptable level rendering it an impractical approach.

Other considerations in MacDonald's book regarding mesh density are as follows:

- In general, employ a finer mesh in areas where high stress is expected (MacDonald, 2011)
- Use a fine mesh around holes (MacDonald, 2011)
- When there is an adverse colour contour transition between elements, increase the mesh size for better resolution (MacDonald, 2011)
- Areas where there is low stress, the mesh density can be low in comparison to rest of the model (MacDonald, 2011)

Appendix F – Model Quality Checks

Element Quality

The quality of the 2D and 3D meshes were checked before running the model. For all the mesh types used, the Jacobian needed to be below 0.6 as this is recommended by *Siemens FEMAP* guide lines to be an acceptable mesh quality for results accuracy (Siemens, 2016). In addition, the regions where it was expected to have high levels of stress in the foot, the quality was greater (0.2 Jacobian) to ensure a better resolution of the results (Predictive Engineerings, 2011).

Jacobian compares the shape of an element to an "ideally shaped" element of the same topology. It takes into consideration all the different aspects of defining a good element. However, this can sometimes mislead an element to be of good quality when actually it is fine in most aspects but poor in others, so should be used with caution (Siemens, 2016).

If a region of the model mesh is poor but is not considered critical or having a big influence on the end result then it could be acceptable.

Testing if the model is over-constrained

To check the model is not over constrained, a simple test was carried out by applying a 1G force to the assembly to ascertain if the reaction forces at the constraints add up to the total mass of the model. If forces do not add up correctly equal to the total mass, then the model is over constrained.

The test included the profile clamps for the stiffness testing. The total mass of the parts comes to 43.74Kg.

The reaction force was 429.113N in total from the 4 bolt holes of the steel foot (see Figure 184). Dividing the 429.113N with 1G gives the mass of the assembly to be 43.74Kg, thus demonstrating the model is not over constrained.

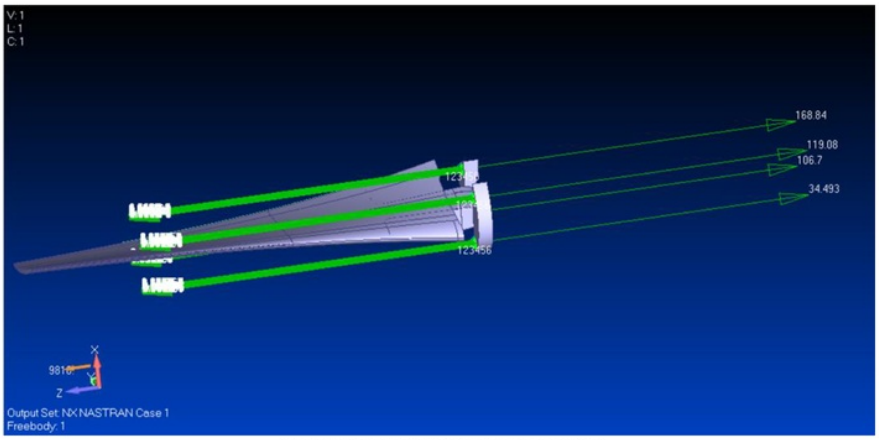


Figure 184 results of the constraint test

Appendix G – Blade Bill Of Materials

This section lists out the bill of materials used in the final design of the blade.

Core Materials

F&S used a PVC foam as core material in the current blade (Fagerberg & Stromberg, 2007). The new blade design will be manufactured with prepregnanted composite materials in view of *Lentus's* extensive experience. The logical material to use was *Rohacell*. *Lentus* have incorporated *Rohacell* in a vast range of products gaining considerable experience. Benefits include:

- Easy to machine
- *Lentus* have a range of suppliers for manufacturing the parts
- Similar mechanical properties to PVC foam

The grade of *Rohacell* used is IG-F 71 and the properties are in detailed in Table 20.

Table 20 Rohacell IG-F 71 properties data (Evonik, 2019)

Property	IG-F 71
Tensile Modulus	92MPa
Density	75Kg/m³
Compressive Strength	1.5MPa
Tensile Strength	2.8MPa
Shear Strength	1.3MPa

Composite Materials

F&S used UD fibre in the current blade as the main structural plies (Fagerberg & Stromberg, 2007). The new blade will follow a similar approach by using *Torayca* T700S UD with *TenCate* E722 resin system. *Lentus* have previously used this product in a range of structural applications accumulating experience working with the material.

In some areas of the blade parts, the geometry renders it difficult to laminate using UD material. Instead, the use of *Grafil* TR30S 3K 2X2 Twill woven with the *TenCate* E722 was more appropriate. *Lentus* have used this previously in conjunction T700S UD. The 2X2 Twill fibre woven format is easier to laminate as the fibres are intertwined and do not splay apart.

Table 21 detail the properties of both composite materials used in the blade:

Table 21 composite material properties **(Torayca, 2018)** *(TenCate, 2018)*

Property	Torayca T700S UD 200gsm 33% Resin Weight	Grafil TR30S 3K 2X2 Twill Woven 50% Resin Weight
Matrix	TenCate E722	
Density	1605.3Kg/m³	1605.3Kg/m³
Tensile elastic modulus fibre direction	135GPa	56GPa
Tensile elastic modulus transverse	5GPa	56GPa
Shear modulus in-plane	5GPa	5GPa
Tensile strength fibre direction	2500MPa	590MPa
Compressive strength fibre direction	1450MPa	565MPa
Tensile strength transverse	100MPa	580MPa
Compressive strength transverse	100MPa	560MPa
Shear strength in-plane	50MPa	50MPa
Shear strength interlaminar	50MPa	50MPa

To assist the composite bond between the *Rohacell* and steel foot, *TenCate* EF72 glue film is used.

Silicone Material

To aid ply consolidation in the blade shroud area, silicone parts were included in the design since they expand during the manufacturing process from the curing heat. The silicone used was a composite application grade *Alchemix* RTV240-C251 detailed in Table 22:

Table 22 silicone propteries (Alchemie, 2019)

Property	Alchemix RTV240-C251
Density	1250Kg/m³
Young's modulus	1.67MPa
Tensile strength	3.4MPa

Structural Steel

F&S used a high yield strength stainless steel for the foot to be able to withstand the high stresses arising in the blade at the point of fixity and avoid the need for a creep analysis within the foot design, as well the corrosion resistant properties (Fagerberg & Stromberg, 2007).

For the replica design, grade 15-5PH steel was chosen as this material fulfilled all the requirements outlined in previous paragraph. After initial FEA runs of the blade design, it was decided with *Lentus* that grade 15-5PH-3 would be acceptable to withstand the stresses from the FEA results. Table 23 provide the properties:

Table 23 15-5P properties (AK Steel)

Property	Stainless Steel 15-5PH-3
Density	7870Kg/m³
Young's modulus	200GPa
Shear modulus	76GPa
Yield strength	1200MPa
UTS	1366MPa

Cosmetic Steel

For all steel parts within the foot that were considered not to be structural or not subject to high stress values, the cheaper stainless steel grade 304 was used as it was more cost effective for the project (see Table 24):

Table 24 304 properties (AZO Materials, 2001)

Property	Stainless Steel 304
Density	7900Kg/m³
Young's modulus	200GPa
Yield strength	205MPa
UTS	515MPa

Appendix H – Blade Design 2

The second blade design took on board the outputs from the first blade design. One of the main points was to reduce the high stress near the base. Earlier in this report it was explained that the best way of doing this was through a composite spar (see Figure 185).

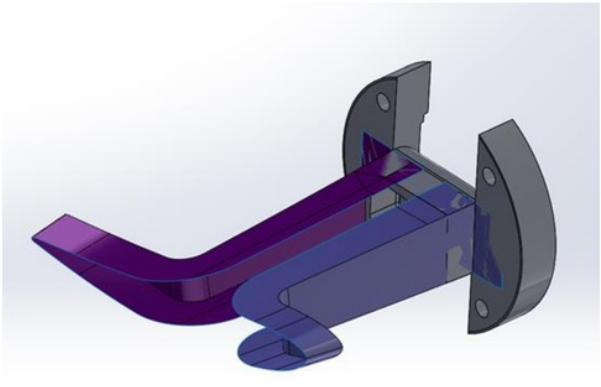


Figure 185 composite spar attached to the foot

To decide how big the spars should be a study was carried out looking at changing the length and overhang (see Figure 186). The study used a previously optimised layup and changed the two spar variables to find an optimum which reduced the stress without changing the stiffness too much from the previous results without the spars.

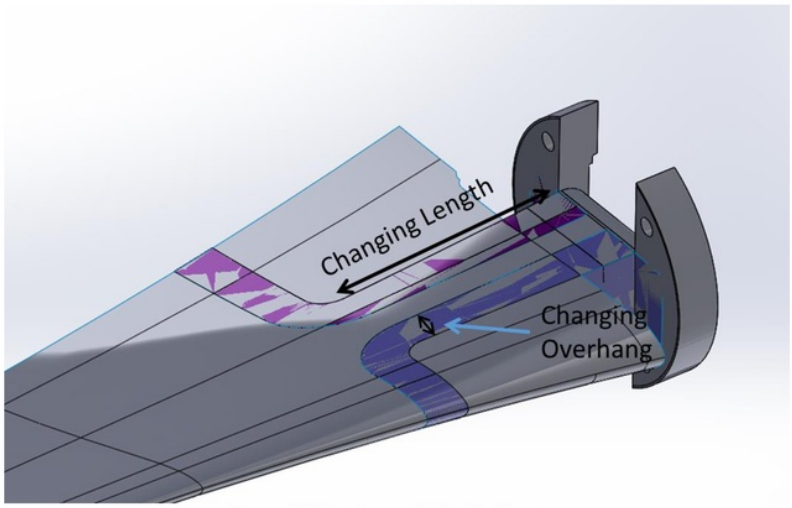
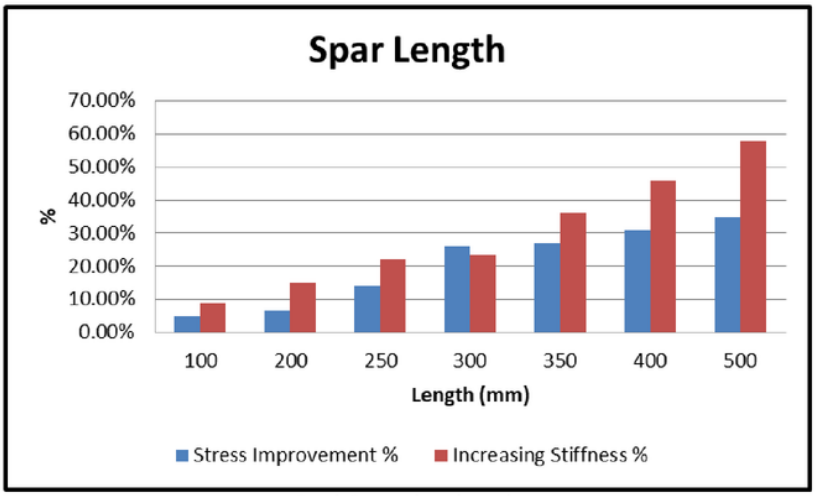


Figure 186 the two variables for the spar

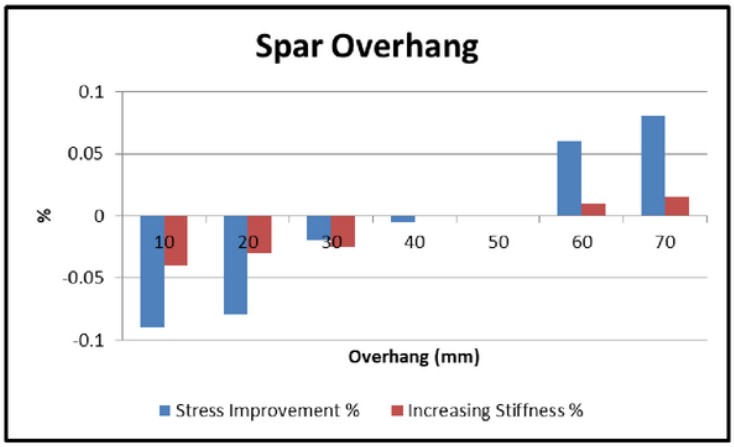
Graph 25 shows the results from changing the spar length. As expected as the length increases the stress decreases in the composite around the foot, but the blade stiffness starts to increases too much. 300mm was taken as the optimum overall and it is not the

highest at removing the stress, but increasing the stiffness too much will not allow for leeway for optimising the main laminate to match the stiffness of the current blade.



Graph 25 spar length results

Taking the 300mm length forward the overhang was tested next. The spar length was found using a set overhang of 50mm, and at 50mm shows 0% change. The results show the overhang change is not very sensitive to affecting the results.



Graph 26 spar overhang results

Overall the 300mm and 50mm overhang was the best and taken forward to be used in the blade.

The foot design was also updated to include the following:

- The foot shape was extended up to the shroud diameter to add mass to the design. This also had the added benefit of expanding into the mould to consolidate shroud plies.
- Extruding part for spars and adding mass. The extruding part also has a pocket for the main core to sit into, which when assembling the blade acts as a location pin.
- Pocket on the back of the foot for the back plate.

Figure 187 shows the updated foot changes.

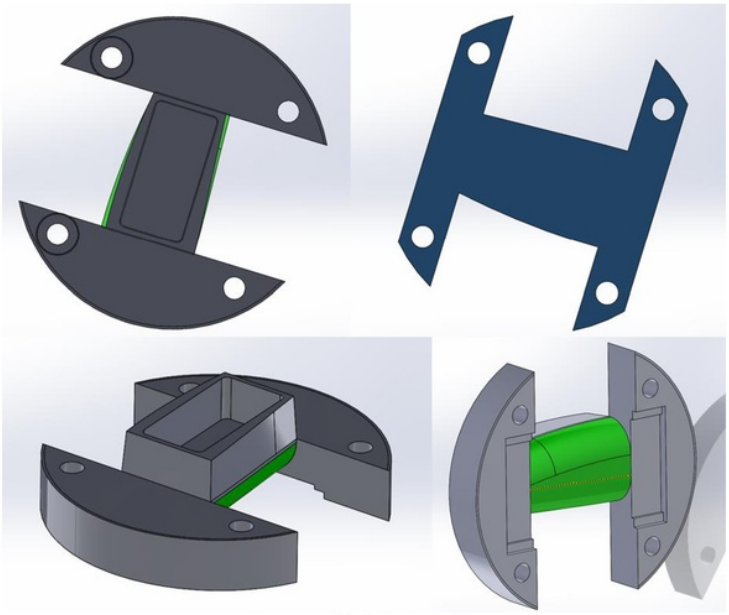


Figure 187 blade design 2 foot

The foot had the extruding part added in to give a bonding surface for the spars to wrap around. It was extruded 20mm before going into the main profile of the blade to give as much bonding surface as possible and was not extruded past as the geometry would start to get too complicated for machining.

To protect the internal materials and close the new blade up, a stainless steel back plate was designed. After curing the blade, the back plate can be bonded into place (see Figure 188). Stainless steel was selected over a composite plate for minimising weight contribution to the total blade mass. The back plate provides the added benefit of being non-structural which means it can act as a way of controlling the total blade weight after curing. The back plate gives 2.3Kg of margin for adjustment of total blade weight.

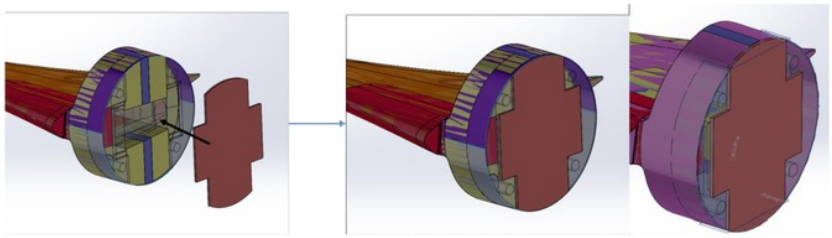


Figure 188 foot back plate

The shroud area parts have been added into the FEA to improve results. To help with consolidating plies in the shroud area, a silicone wedge is added into the blade shroud design (see Figure 189) which expands from the heat generated from the curing process and rams core parts into the shroud plies. This idea pushed the shroud core parts into the mould walls. As well the core parts were split up to be easy to assemble when manufacturing the blade.

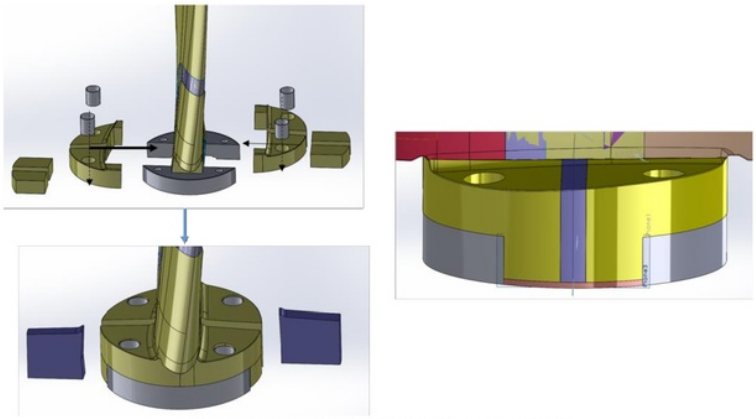


Figure 189 silicone parts and shroud core parts

Figure 190 is the FEA results of the composite stress with the updated blade parts. The similar trends remain from the first blade design, but comparing the same laminate with and without the spar shows how the spars are reducing the stress (see Figure 190).

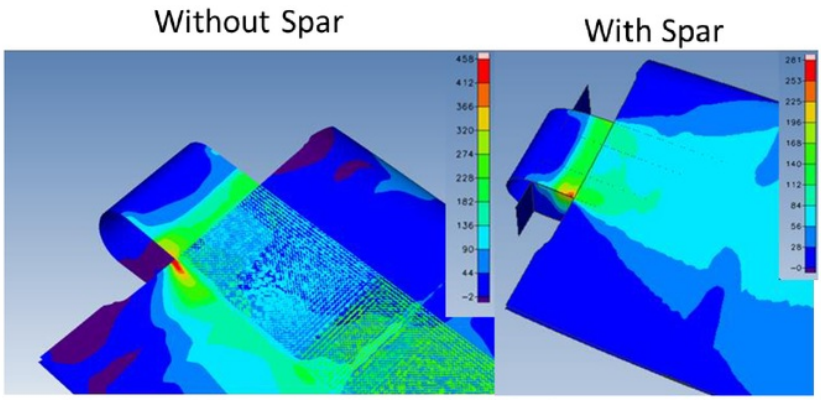


Figure 190 FEA stress results of design 2 composite with updated parts

However, at this point it was noticed that the failure index results were not making sense (see Figure 191).

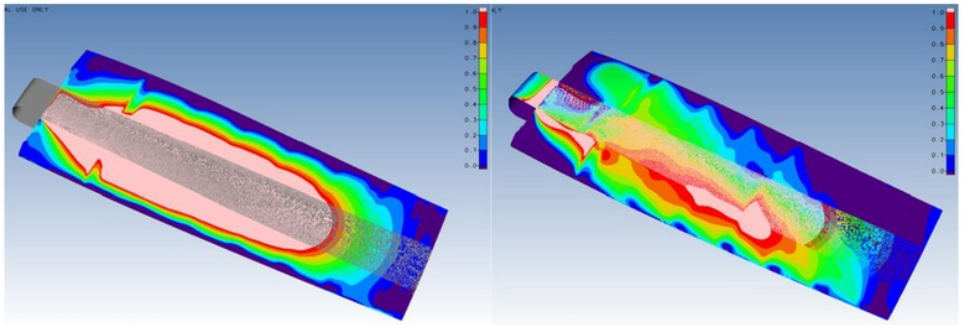


Figure 191 blade design 2 composite failure index results

The steel foot and main foam core are showing points where there are stress consternation areas (see red circles in Figure 192).

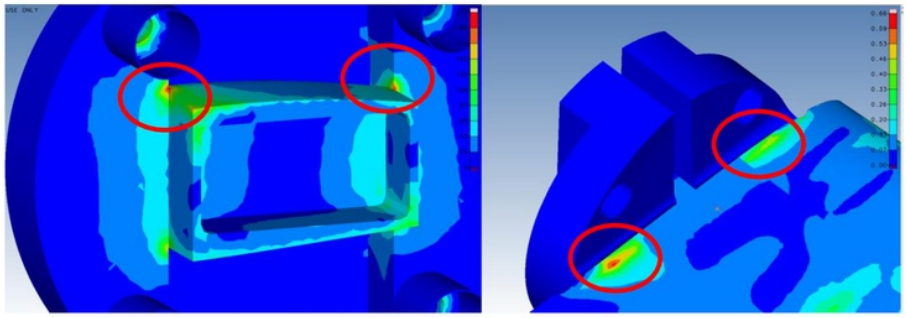


Figure 192 FEA stress results of foot and main foam core

The out comes from design 2 were as follows:

- The composite spars results show improvements on the stress within the composite.
- The failure index seems far too high, further investigation is needed.

- In the next designs the foot and main core stress concentration areas need to be improved.

Appendix I – Blade Design 5

Design 5 took the same principles forward from design 2. Design 5 developed the laminate to match the stiffness results of the current blade.

Figure 193 and Graphs 27, 28 and 29 (which are 3 sets of data from the FEA against the testing data) show the results of the stiffness of the blade matching the exact data from testing. However, the laminate designs outputted by the software were either not symmetrical or in small patches (see Figure 194). The former was mainly down to the software attempting to make the layup as light as possible. This was not a problem in terms of manufacturing this type of layup, but when only applying the bending load in one direction, there was no guarantee that if the blade was loaded in the opposite direction, it would achieve the same stiffness performance, nor cope with stresses. Similarly, this can also be said for having a symmetrical laminate due to profile shape, but the risk is minimal in comparison to the non-symmetrical laminate.

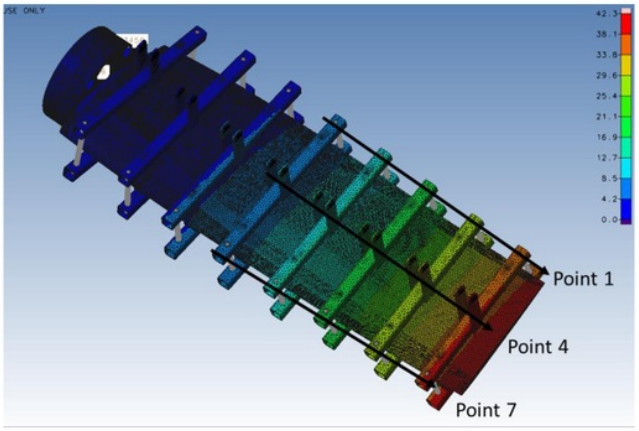
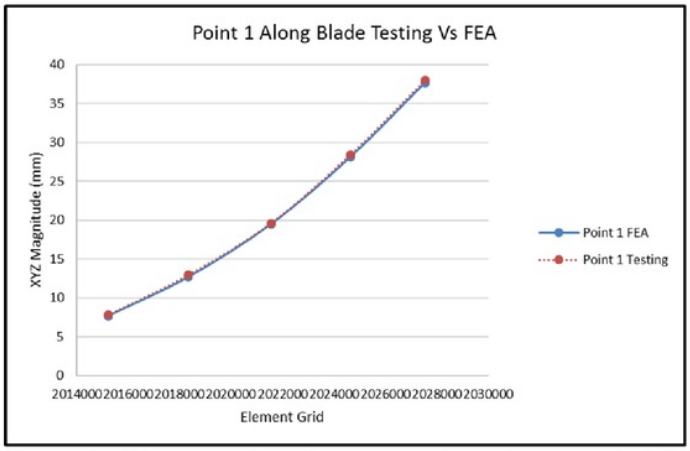
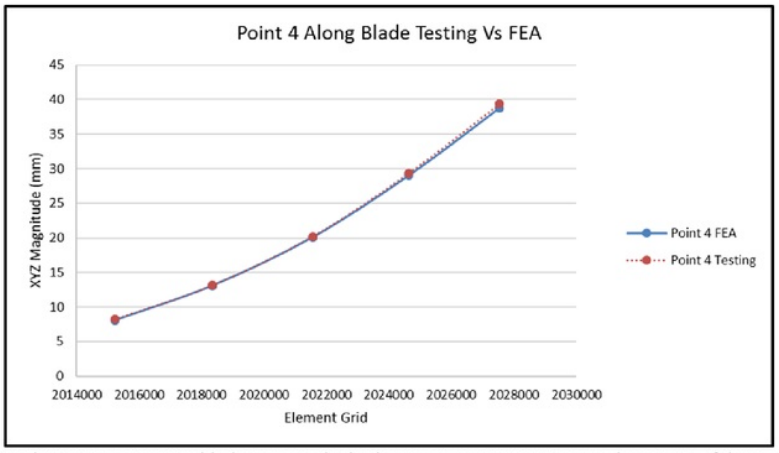


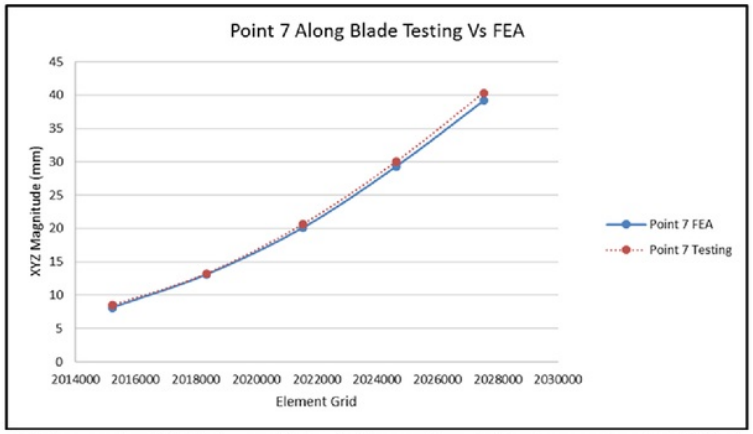
Figure 193 displacement FEA results of blade design 5



Graph 27 comparing FEA blade magnitude displacement against testing results point 1 of design 5



Graph 28 comparing FEA blade magnitude displacement against testing results point 4 of design 5



Graph 29 comparing FEA blade magnitude displacement against testing results point 7 of design 5

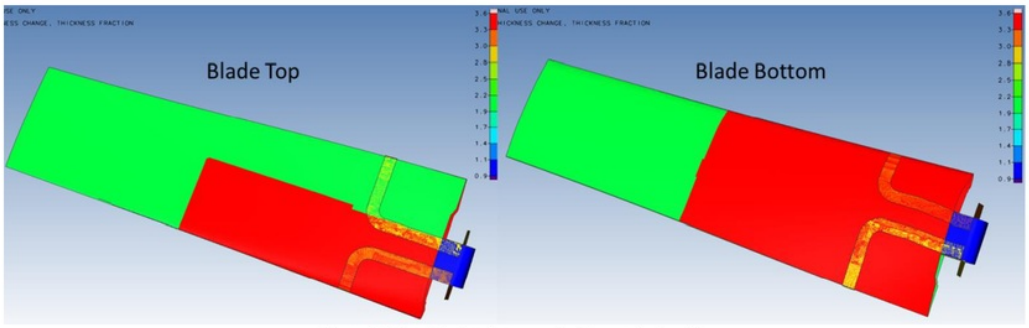


Figure 194 optimised composite layup design 5

Not outputting a symmetrical laminate was the limit of the software capability on this project. To progress the project forward, the best ply shape design was taken and specified to be symmetrical, Figure 195 was the optimum shape.

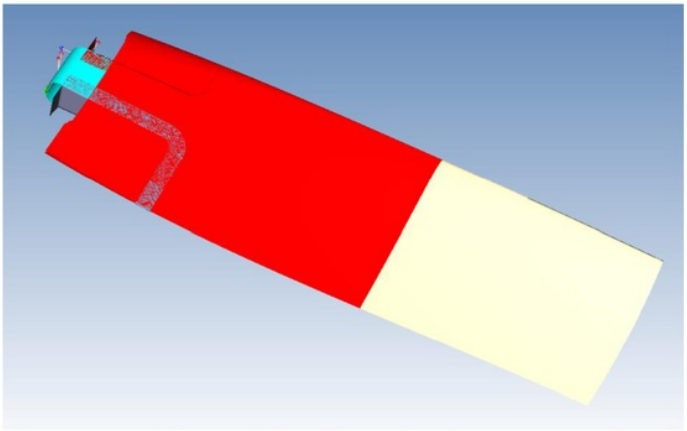
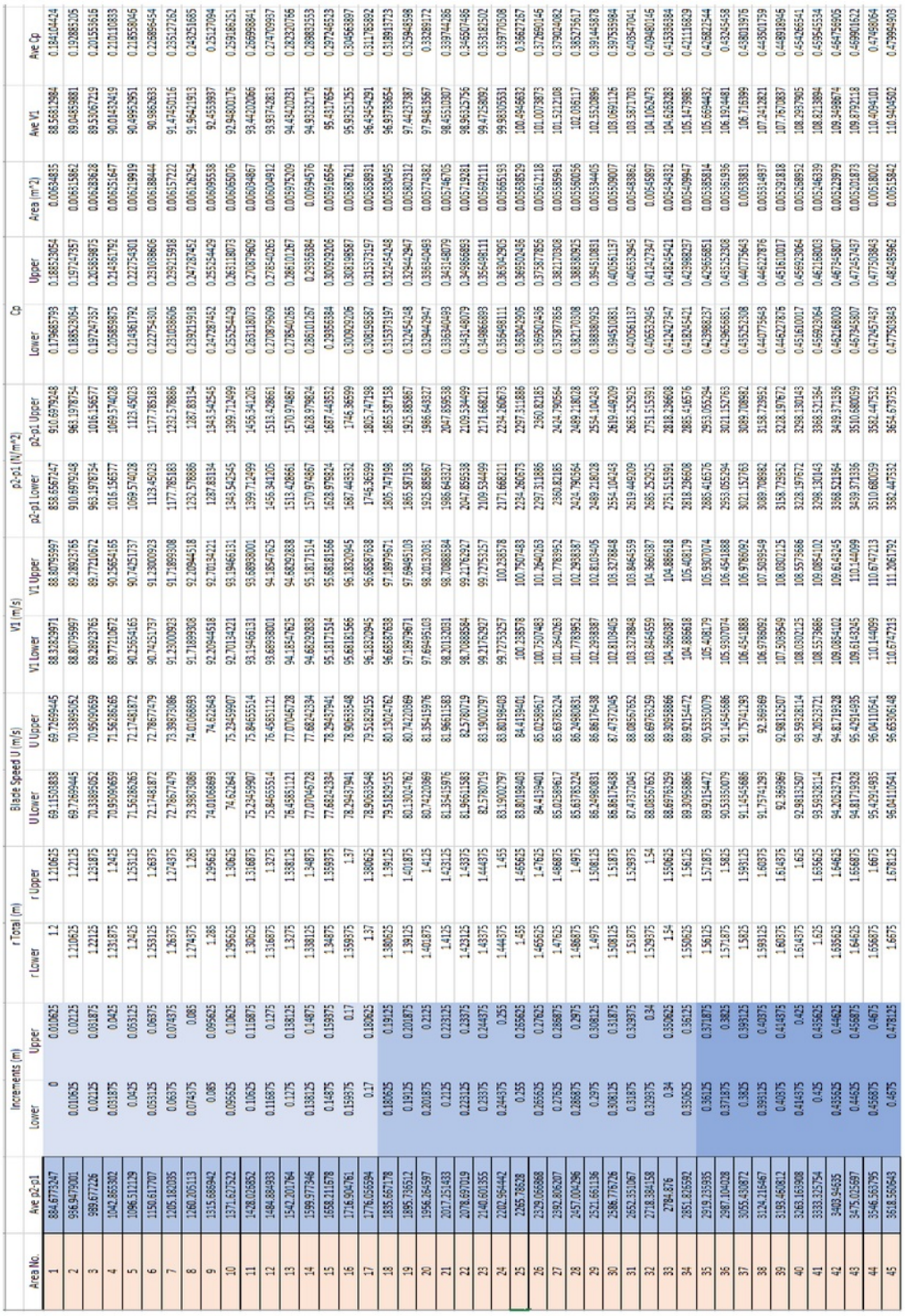


Figure 195 optimised composite layup for manufacturing to move project forward

Appendix J – Extra Information



Area No.	Ave p2-p1	Increments (m)		r Total (m)		Blade Speed U (m/s)		V1 (m/s)		p2-p1 (N/m^2)		Cp		Area (m^2)	Ave V1	Ave Cp
		Lower	Upper	r Lower	r Upper	U Lower	U Upper	V1 Lower	V1 Upper	p2-p1 Lower	p2-p1 Upper	Lower	Upper			
1	884.6773247	0	0.010625	1.2	1.210625	69.11503838	69.72698445	88.33829971	88.80795997	858.6567247	910.6979248	0.179685793	0.188523054	0.00634835	88.56812984	0.184104424
2	936.9473001	0.010625	0.02125	1.210625	1.22125	69.72698445	70.33895052	88.80795997	89.28925765	910.6979248	961.1978754	0.188523054	0.197247357	0.006319862	89.04859881	0.192085105
3	989.6772226	0.02125	0.031875	1.22125	1.231875	70.33895052	70.95093659	89.28925765	89.77210672	961.1978754	1016.156577	0.197247357	0.205893875	0.006283628	89.53367219	0.200563616
4	1042.865302	0.031875	0.0425	1.231875	1.2425	70.95093659	71.56286265	89.77210672	90.25654165	1016.156577	1069.574028	0.205893875	0.214361792	0.006251647	90.01432419	0.210110833
5	1096.531219	0.0425	0.053125	1.2425	1.253125	71.56286265	72.17481872	90.25654165	90.74251737	1069.574028	1123.45023	0.214361792	0.222754301	0.006219919	90.49953951	0.218558045
6	1150.617707	0.053125	0.06375	1.253125	1.26375	72.17481872	72.78677479	90.74251737	91.23000923	1123.45023	1177.785183	0.222754301	0.231038605	0.006188444	90.98626633	0.226896454
7	1205.182035	0.06375	0.074375	1.26375	1.274375	72.78677479	73.39873086	91.23000923	91.71899308	1177.785183	1232.578886	0.231038605	0.239215918	0.006157222	91.47450116	0.235127262
8	1260.205113	0.074375	0.085	1.274375	1.285	73.39873086	74.01068693	91.71899308	92.20944518	1232.578886	1287.83134	0.239215918	0.247267452	0.006126254	91.96421913	0.243251665
9	1315.686942	0.085	0.095625	1.285	1.295625	74.01068693	74.622643	92.20944518	92.70119221	1287.83134	1343.542545	0.247267452	0.255254429	0.006095538	92.4553997	0.25127094
10	1371.627522	0.095625	0.10625	1.295625	1.30625	74.622643	75.23459907	92.70119221	93.19466131	1343.542545	1399.712499	0.255254429	0.263118073	0.006065076	92.94001176	0.259186251
11	1428.026652	0.10625	0.116875	1.30625	1.316875	75.23459907	75.84655514	93.19466131	93.68938001	1399.712499	1456.341205	0.263118073	0.271079609	0.006034867	93.44202066	0.266998841
12	1484.884933	0.116875	0.1275	1.316875	1.3275	75.84655514	76.45851121	93.68938001	94.18547635	1456.341205	1513.426661	0.271079609	0.278540265	0.006004912	93.93743813	0.274709937
13	1542.201764	0.1275	0.138125	1.3275	1.338125	76.45851121	77.07046728	94.18547635	94.68202838	1513.426661	1570.974867	0.278540265	0.286101267	0.005975209	94.43420231	0.282320766
14	1599.977346	0.138125	0.14875	1.338125	1.34875	77.07046728	77.68242394	94.68202838	95.18171514	1570.974867	1628.979824	0.286101267	0.29356884	0.005945676	94.93232176	0.289883533
15	1658.211678	0.14875	0.159375	1.34875	1.359375	77.68242394	78.29437941	95.18171514	95.68181566	1628.979824	1687.440332	0.29356884	0.300929206	0.005916564	95.4317654	0.297446523
16	1716.904761	0.159375	0.17	1.359375	1.37	78.29437941	78.90633548	95.68181566	96.18320945	1687.440332	1746.96599	0.300929206	0.308198587	0.005887611	95.93251255	0.304563897
17	1776.056594	0.17	0.180625	1.37	1.380625	78.90633548	79.51829155	96.18320945	96.68587638	1746.96599	1805.747198	0.308198587	0.315373197	0.005858831	96.43454291	0.311785892
18	1835.669178	0.180625	0.19125	1.380625	1.39125	79.51829155	80.13024762	96.68587638	97.18979671	1805.747198	1865.587158	0.315373197	0.322454248	0.005830455	96.93783654	0.318913723
19	1895.736512	0.19125	0.201875	1.39125	1.401875	80.13024762	80.74220069	97.18979671	97.69485103	1865.587158	1925.885867	0.322454248	0.329442947	0.005802312	97.44237387	0.325948598
20	1956.264597	0.201875	0.2125	1.401875	1.4125	80.74220069	81.35415976	97.69485103	98.20132031	1925.885867	1986.643227	0.329442947	0.336540493	0.005774382	97.94813567	0.33289172
21	2017.251493	0.2125	0.223125	1.4125	1.423125	81.35415976	81.96611583	98.20132031	98.70888584	1986.643227	2047.895538	0.336540493	0.343148079	0.005746705	98.45510307	0.339744285
22	2078.697019	0.223125	0.23375	1.423125	1.43375	81.96611583	82.57807719	98.70888584	99.21762927	2047.895538	2109.534499	0.343148079	0.349866893	0.005719281	98.96325756	0.345607486
23	2140.601855	0.23375	0.244375	1.43375	1.444375	82.57807719	83.19002797	99.21762927	99.72753257	2109.534499	2171.668211	0.349866893	0.356498111	0.005692111	99.47258092	0.353182502
24	2202.964442	0.244375	0.255	1.444375	1.455	83.19002797	83.80198403	99.72753257	100.2387578	2171.668211	2234.260673	0.356498111	0.363942965	0.005665193	99.98305331	0.359770508
25	2265.78628	0.255	0.265625	1.455	1.465625	83.80198403	84.4139401	100.2387578	100.7507483	2234.260673	2297.311886	0.363942965	0.371877855	0.005638539	100.4945832	0.36627267
26	2329.055868	0.265625	0.27625	1.465625	1.47625	84.4139401	85.02589617	100.7507483	101.2640263	2297.311886	2360.82185	0.371877855	0.379877006	0.005612118	101.0073873	0.373690146
27	2393.806207	0.27625	0.286875	1.47625	1.486875	85.02589617	85.63785224	101.2640263	101.7783952	2360.82185	2424.790564	0.379877006	0.382170308	0.005585961	101.5212108	0.379024082
28	2457.004296	0.286875	0.2975	1.486875	1.4975	85.63785224	86.24980831	101.7783952	102.2938387	2424.790564	2489.218028	0.382170308	0.388380925	0.005560056	102.036117	0.385273617
29	2521.661136	0.2975	0.308125	1.4975	1.508125	86.24980831	86.86176438	102.2938387	102.8103405	2489.218028	2554.104243	0.388380925	0.394510831	0.005534405	102.5520896	0.391445878
30	2586.776726	0.308125	0.31875	1.508125	1.51875	86.86176438	87.47372045	102.8103405	103.3278848	2554.104243	2619.449209	0.394510831	0.400561157	0.005509007	103.0691126	0.397535984
31	2652.351067	0.31875	0.328375	1.51875	1.528375	87.47372045	88.08567652	103.3278848	103.8454559	2619.449209	2685.252915	0.400561137	0.406553945	0.005483862	103.5871703	0.403547041
32	2718.384158	0.328375	0.34	1.528375	1.54	88.08567652	88.69763259	103.8454559	104.3660387	2685.252915	2751.515391	0.406553945	0.412472347	0.005458897	104.1062473	0.409480146
33	2784.826	0.34	0.350625	1.54	1.550625	88.69763259	89.30958866	104.3660387	104.886618	2751.515391	2818.296608	0.412472347	0.418245421	0.005434332	104.6263283	0.415383584
34	2851.825592	0.350625	0.36125	1.550625	1.56125	89.30958866	89.92154472	104.886618	105.408179	2818.296608	2885.416576	0.418245421	0.423988237	0.005409947	105.1479885	0.421116629
35	2919.235935	0.36125	0.371875	1.56125	1.571875	89.92154472	90.53350079	105.408179	105.9307074	2885.416576	2953.055294	0.423988237	0.429656851	0.005385814	105.6694432	0.426821544
36	2987.104028	0.371875	0.3825	1.571875	1.5825	90.53350079	91.14545686	105.9307074	106.4541888	2953.055294	3021.152763	0.429656851	0.435252308	0.005361936	106.1924481	0.43245458
37	3055.430872	0.3825	0.393125	1.5825	1.593125	91.14545686	91.75741293	106.4541888	106.9786092	3021.152763	3089.708982	0.435252308	0.440775643	0.005338831	106.715399	0.438013976
38	3124.215467	0.393125	0.40375	1.593125	1.60375	91.75741293	92.3689869	106.9786092	107.5039549	3089.708982	3158.723952	0.440775643	0.446227876	0.005314937	107.2412821	0.443501759
39	3193.465812	0.40375	0.414375	1.60375	1.614375	92.3689869	92.98132507	107.5039549	108.0302125	3158.723952	3228.197672	0.446227876	0.451610017	0.005291818	107.7670837	0.448918945
40	3263.163908	0.414375	0.425	1.614375	1.625	92.98132507	93.59328114	108.0302125	108.5573686	3228.197672	3298.130143	0.451610017	0.456923064	0.005268852	108.2957965	0.454265541
41	3333.315754	0.425	0.435625	1.625	1.635625	93.59328114	94.20523721	108.5573686	109.0854102	3298.130143	3368.521364	0.456923064	0.462188003	0.005246339	108.8213894	0.459545534
42	3403.94455	0.435625	0.446625	1.635625	1.646625	94.20523721	94.81719328	109.0854102	109.6145245	3368.521364	3439.371336	0.462188003	0.467545807	0.005224979	109.3498674	0.464756905
43	3475.025697	0.446625	0.458875	1.646625	1.658875	94.81719328	95.42914935	109.6145245	110.144099	3439.371336	3510.880059	0.467545807	0.472457437	0.005201873	109.879218	0.469901622
44	3546.563795	0.458875	0.4675	1.658875	1.6675	95.42914935	96.04110541	110.144099	110.6747213	3510.880059	3582.447332	0.472457437	0.477503843	0.005180002	110.4094101	0.47498064
45	3618.580643	0.4675	0.478125	1.6675	1.678125	96.04110541	96.65306148	110.6747213	111.2061792	3582.447332	3654.573755	0.477503843	0.482485962	0.005158422	110.9404502	0.479994903

Figure 196 excel load distribution calculations

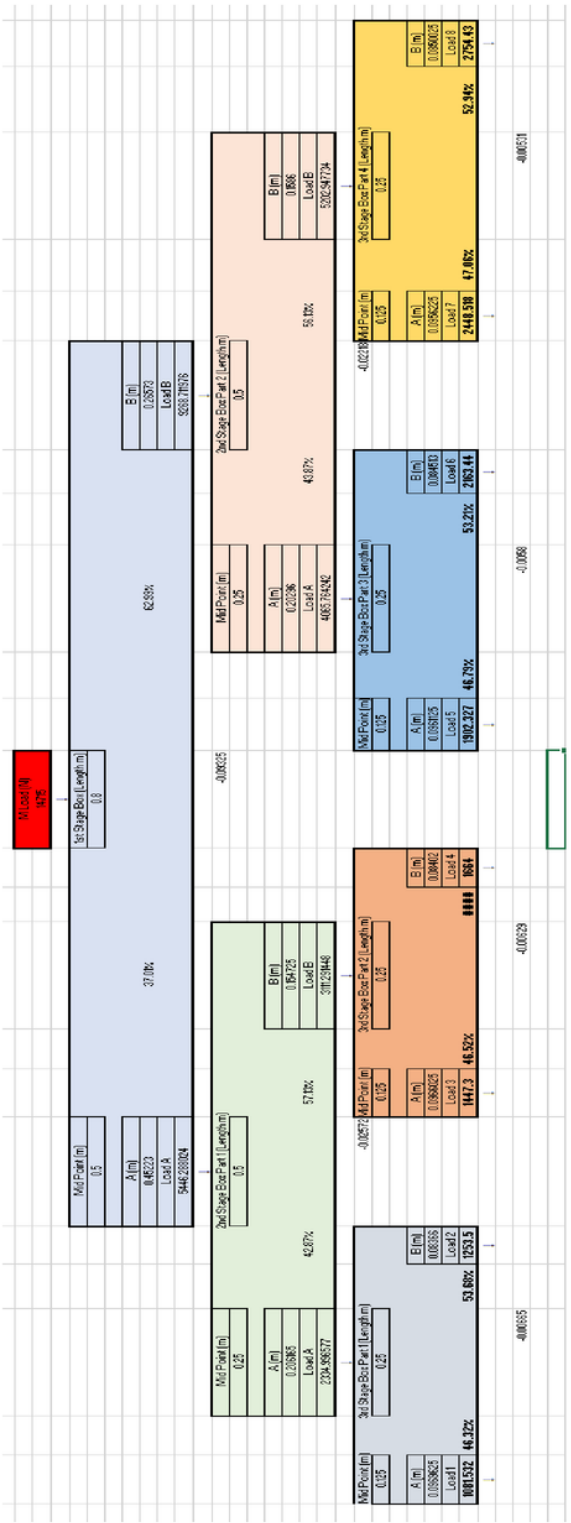


Figure 197 excel spreadsheet construction to calculate the distance between pin joints for the right load distribution

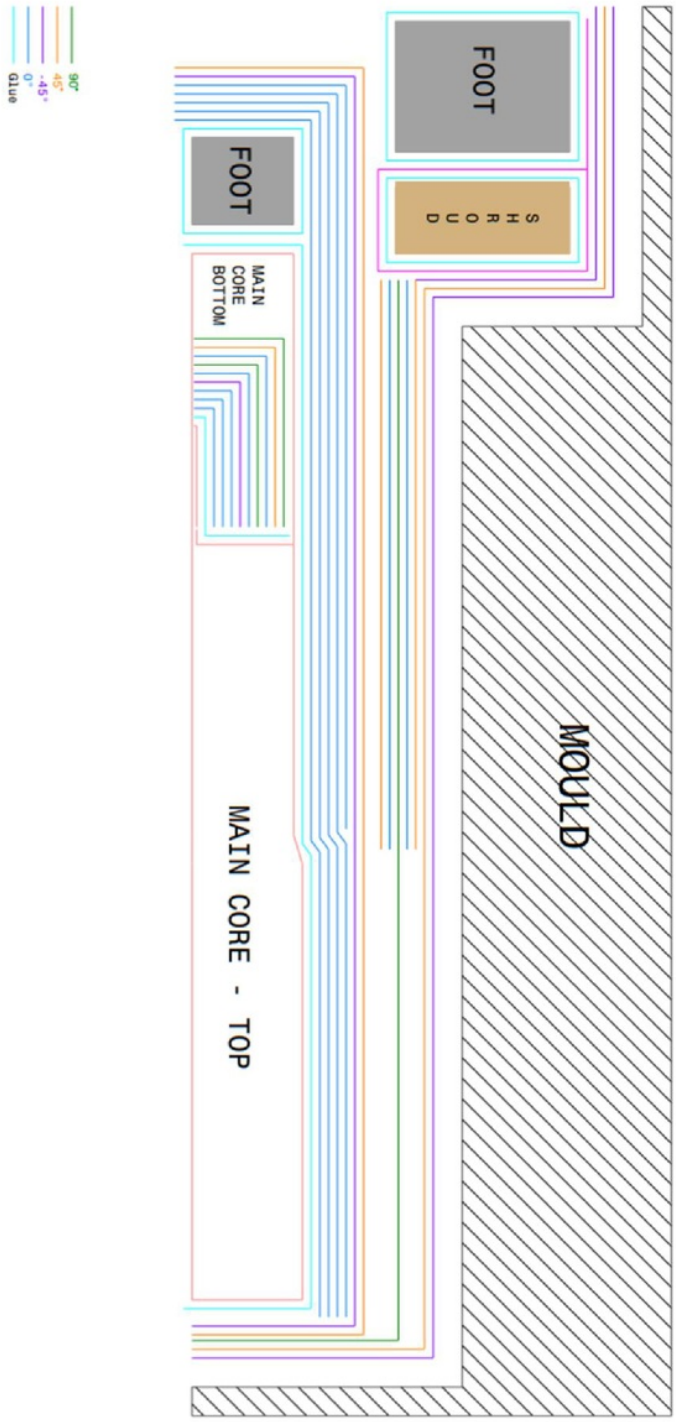


Figure 198 final blade layup (Lentus Composites, 2019)